University of Massachusetts Amherst
ScholarWorks@UMass Amherst

Masters Theses | Dissertations and Theses

August 2014

Performance of Circular Reinforced Concrete Bridge Piers Subjected to Vehicular Collisions

Nevin L. Gomez
University of Massachusetts Amherst

Follow this and additional works at: https://scholarworks.umass.edu/masters_theses_2

 Part of the Structural Engineering Commons

Recommended Citation

Gomez, Nevin L., "Performance of Circular Reinforced Concrete Bridge Piers Subjected to Vehicular Collisions" (2014). *Masters Theses*. 20.
https://scholarworks.umass.edu/masters_theses_2/20

This Open Access Thesis is brought to you for free and open access by the Dissertations and Theses at ScholarWorks@UMass Amherst. It has been accepted for inclusion in Masters Theses by an authorized administrator of ScholarWorks@UMass Amherst. For more information, please contact scholarworks@library.umass.edu.

PERFORMANCE OF CIRCULAR REINFORCED CONCRETE BRIDGE PIERS SUBJECTED TO VEHICULAR COLLISIONS

A Thesis Presented

by

NEVIN L. GÓMEZ

Submitted to the Graduate School of the
University of Massachusetts Amherst in partial fulfillment
of the requirements for the degree of

MASTER OF SCIENCE IN CIVIL ENGINEERING

MAY 2014

Civil and Environmental Engineering
Structural Engineering and Mechanics

PERFORMANCE OF CIRCULAR REINFORCED CONCRETE BRIDGE PIERS SUBJECTED TO VEHICULAR COLLISIONS

A Thesis Presented

by

NEVIN L. GÓMEZ

Approved as to style and content by:

_____
Azadeh Alipour, Chairperson

_____
Behrouz Shafei, Member

_____
Paul Fisette, Member

_____
Richard N. Palmer, Department Head
Civil and Environmental Engineering Department

ABSTRACT

PERFORMANCE OF CIRCULAR REINFORCED CONCRETE BRIDGE PIERS SUBJECTED TO VEHICULAR COLLISIONS

MAY 2014

NEVIN L. GÓMEZ, B.S.C.E, UNIVERSITY OF MASSACHUSETTS, AMHERST

M.S.C.E., UNIVERSITY OF MASSACHUSETTS, AMHERST

Directed by: Professor Azadeh Alipour

Vehicle collisions with bridge piers can result in significant damage to the support pier and potentially lead to catastrophic failure of the whole structure. The Nation's aging infrastructure suggests that many structures no longer meet current design standards, placing many bridge susceptible to failure if subjected to an extreme loading event. This research aims to study the structural response of reinforced concrete bridge piers subjected to vehicle collisions. A sensitivity analysis is conducted to observe the causes of shear and bending failures of bridge piers subjected to vehicle collision. Parameters, such as pier diameter, transverse reinforcement spacing, vehicle impact velocity, pile cap height, and multi-pier configuration, are investigated in this study.

The finite element code LS-DYNA is utilized to simulate and analyze the vehicle collisions to obtain accurate and detailed results. The vehicle models offered by the National Crash Analysis Center and the National Transportation Research Center, Inc. are used to conduct this research. The finite element modeling controls and material properties are validated by conducting an impact drop hammer experiment. The bridge pier collision models are validated by comparing vehicle damage and impact forces with

published research results. Conservation of energy is also checked to assure stability within the impact simulation.

A sensitivity analysis suggests that different pier parameters have a profound effect on failure modes and distribution of impact forces. Piers with large stiffness result in high impact forces, low lateral displacements, and high resistance to shear forces and bending moments. A performance-based analysis shows that bridge piers can be designed using damage ratios associated with particular damage states.

TABLE OF CONTENTS

Page

LIST OF TABLES

Page

LIST OF FIGURES

Page

LIST OF EQUATIONS

Page

CHAPTER 1.

INTRODUCTION

1.1. Introduction

A vehicle collision with a bridge pier is an extreme loading event that may occur very rarely in the lifespan of a bridge, but can result in significant structural damage to the support piers, bent cap, foundation, and superstructure, with the possibility of leading to full structural failure or collapse. A study conducted by Harik et al. (1990) investigated the cause of 79 bridge failures in the United States between the years 1951 to 1988. The study showed that the leading causes of bridge failures were due to collisions involving ships, trucks, and trains. The study also showed that the 36 collision accidents leading to complete and partial bridge failure outnumbered the 29 failures caused by natural phenomenon including flood, scour, wind, earthquake, etc. A similar study conducted by Wardhana and Hadipriono (2003) analyzed the cause of bridge failures in the United States between the years 1989 to 2000. This study showed that hydraulic sources, such as flood and scour, were the leading cause of bridge failures. The second leading cause of bridge failures was due to accidental collisions; accounting for 11.73% of the 503 bridge failures that occurred. These studies indicate that the biggest causes of bridge failures are hydraulic damage, vehicle collision, material deterioration, and overloading of the structure.

The following recent vehicle collisions with bridge piers have not resulted in structural collapse of the bridges, but they have caused significant damage to the bridge components and led to traffic disruptions in major metropolitan areas.

On 15 August 2007 at around 3:00 a.m., a tractor-trailer carrying 55-gallon drums of sodium hypochlorite was traveling westbound on I-70 in Grand Junction, CO, when it lost control and crashed into the north support pier of the Road 26.5 overpass (Gallegos and McPhee 2007). Two fatalities were reported after the wreck. The chemicals being carried did not pose any risk to the public but did require environmental cleanup. The truck took out 75 ft of guardrail before striking the bridge pier. The force of the impact sheared the column at the bent cap connection, as shown in Figure 1.1. The bridge was reopened the next day after a temporary support was constructed. The repairs to the bridge support cost around $286,000 and took about four months to complete (Colorado DOT 2007).

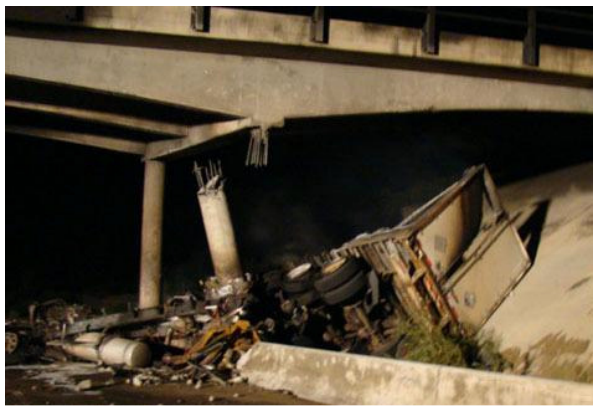

Figure 1.1. Road 26.5 pier support failure caused by tractor-trailer impact in Grand Junction, CO (Gallegos and McPhee 2007)

On 22 May 2011 at around 3:00 a.m., a tractor-trailer carrying newspapers and magazines was traveling northbound on I-85 near Gaffney, SC, when it struck the pier of the SC Highway 150 overpass (Kudelka 2011). The force of the collision destroyed the impacted column and half of the bent cap while also damaging the other two columns and resulting in the sagging of the superstructure spans. The destruction caused by the collision is shown in Figure 1.2. I-85 northbound traffic resumed 52 hours following the accident, after the damaged section of the overpass was demolished. The whole overpass

was later replaced with an entirely new bridge that took four months to construct. The roadway was reopened on SC Highway 150 on 21 October 2011.

Figure 1.2. Damage caused by the tractor-trailer collision with the SC Highway 150 bridge over I-85 (Smoke 2012)

On 11 June 2012 at around 4:00 p.m., a tractor-trailer carrying various electronics was traveling westbound on I-30 in Dallas, TX, when the driver supposedly fell asleep at the wheel and crashed into the bridge support columns of the Dolphin Road overpass (Vega 2012). The force of the impact was so great that the cab of the tractor and a portion of the trailer were split in half. The impact, shown in Figure 1.3, resulted in a shear failure to the easternmost pier, requiring emergency repairs to be conducted to stabilize the overpass. The highway was shut down for over 15 hours and the repairs to the bridge took about a week.

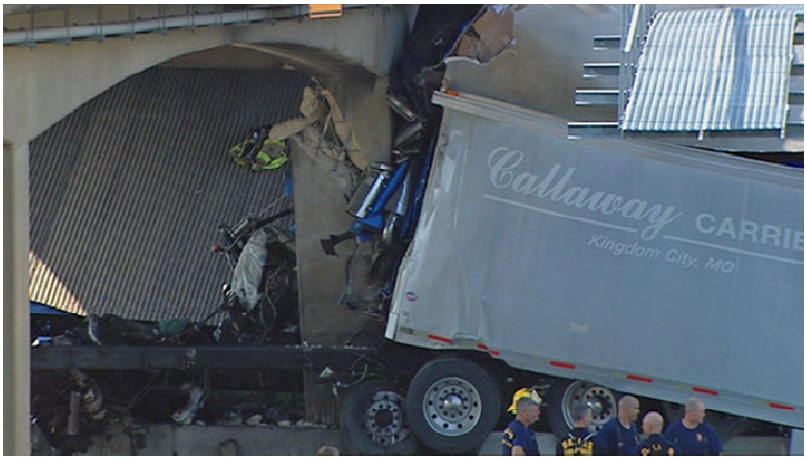

Figure 1.3. Tractor-trailer collision with the I-30 bridge over Dolphin Road (Vega 2012)

Bridge failures due to vehicle collisions have huge economic impacts and can result in the loss of human life. The economic impacts include the cost required to repair or replace the damage to the bridge, vehicles involved, and goods lost. Additional costs are associated with redirecting traffic during the repair work, lost commerce to local businesses due to the disrupted traffic circulation, and remediation due to any environmental damage caused from the accident (Kamaitis 1997). When a bridge is damaged and requires immediate repair, an emergency contract needs to be written up and bids put out with haste to reduce the impact on disrupted traffic. The states departments of transportation finance these projects with states funds that could otherwise be used to improve other government facilities or programs.

1.2. Objectives/Scope of Research

The objectives of this research consist of the follows: (1) conduct a thorough literature review to understand the interactions and processes associated with vehicle collisions with bridge piers and how to investigate such events using finite element modeling; (2) model an impact event to assure material models and finite element process are working correctly; (3) model a single-column bridge pier and validate the accuracy of

the vehicle models by comparing analytical results with published results; (4) conduct a sensitivity analysis to observe the effects of pier diameter, hoop spacing, vehicle impact velocity, pile cap height, and multi-pier bents on the structural resistance and response of bridge piers.

Chapter 2 aims to establish a comprehensive literature review on the topic of vehicle collisions with bridge piers, as well as how to model such events using the finite element code LS-DYNA. The literature review revealed that, although not the leading cause of bridge failures, vehicle collisions pose a serious threat to bridges and can cause extensive damage to the structure. The equivalent static force design load recommended by AASHTO greatly underestimates the dynamic impact force generated during a collision event (El-Tawil 2004). Researchers look to developing finite element model to simulate vehicle collision events to gain a better understanding of the design forces that are resisted by impacted bridge piers.

Chapter 3 aims to analytically quantify the vehicle impact forces generated during collision events. Conservation of energy is used to define a vehicle impact force based on the vehicle mass, impact velocity, and the amount of displacement caused by crushing of the vehicle. This method of determining impact force can be used to establish an equivalent static force for design purposes in piers under elastic deformations.

Chapter 4 aims to validate finite element materials and controls that can be used to conduct vehicle impact simulations. Due to a lack experimental data involving vehicle collisions with bridge piers, a similar impact phenomenon was modeled using a drop hammer experiment. Rectangular reinforced concrete beams with varying longitudinal reinforcement ratios were subjected to impact loads. The analytical results for mid-span

displacement and impact forces were compared with reported experimental data. The finite element controls and material models were validated for use with impact load simulations.

Chapter 5 aims to validate the finite element procedures and controls for modeling vehicle collisions with bridge piers. Three vehicle models were investigated: a Chevrolet C2500 pickup truck, a Ford F800 single unit truck, and a tractor-trailer truck. The vehicle models were simulated at 55, 90, 110, and 135 km/h. The vehicle models were validated by comparing vehicle damage and peak impact forces resulting from similar published simulations. The impact simulations correlated well with the published results and were used with confidence to conduct further research.

Chapter 6 aims to identify how different parameters affect the failure of bridge piers subjected to vehicle collisions. A sensitivity analysis is conducted to evaluate the impact of different parameters, such as pier diameter, hoop spacing, vehicle impact velocity, pile cap height, and multi-pier bent configuration. A performance-based analysis is conducted to identify different damage states resulting from various damage ratios. The damage ratios are based on the peak dynamic impact force resulting from the simulation, as well as the shear capacity of the pier. A performance-based analysis could be used to replace the equivalent static force recommended by AASHTO for vehicle impact loads on bridge piers.

CHAPTER 2.

LITERATURE REVIEW

The American Society of Civil Engineers (ASCE) published a report that depicts the condition and performance of the Nation's civil infrastructure. The report presents the rating similar to those used in a school report card, where an A is exceptional condition and F is failing. The condition of the Nation's bridges received a grade of C+, which corresponds to a mediocre rating. As of 2013, there were 607,380 bridges in the United States; of which 66,749 were found to be structurally deficient and 84,748 functionally obsolete (ASCE 2013). Structurally deficient bridges require significant maintenance, rehabilitation or complete replacement. Functionally obsolete bridges are outdated and do not meet the design standards in use today. This suggests that nearly 25% of the Nation's bridges do not meet design standards and are susceptible to failure if subjected to an extreme loading event. The average age of all the bridges in the United States is 42 years. Nearly $12.8 billion is spent annually on improving the Nation's bridges, but it is estimated that another $8 billion is required to reduce the backlog of work necessary to bring all the bridges up to a suitable level.

Harik et al. (1990) reported the causes of bridge failures in the United States from 1951 to 1988. The 114 failure cases were classified into two categories: complete and partial collapse. Complete collapse consisted of bridges that were no longer able to support their design loads due to loss of a pier, a span, or a major portion of their sub- or superstructure. Partial collapse consisted of bridges that required only partial closure of the bridge. The observed causes of bridge failures were due to vehicle accidents, nature,

age of structure, and overweight loading. The majority of the observed vehicle collision failures were due to trucks, ships, and trains.

Wardhana and Hadipriono (2003) repeated the same study as Harik et al. (1990) for the years between 1989 and 2000. Causes of bridge failures during this period included, but were not limited to, hydraulic, collision, overload, deterioration, fire, and earthquake. Of the total 503 bridge failures analyzed during this time period, 59 failures were a result of vehicular collisions; 14 from automobiles and trucks, 10 from barges, ships and tankers, 3 from trains, and 32 from other collision related causes. Vehicular collisions were the third most frequent cause of bridge failure, accounting for nearly 12% of all bridge failures after flood and scour.

Agrawal and Chen (2008) analyzed the causes of over-height vehicle impact events with bridge components for the state of New York from 1998 to 2008. A thorough literature review on the subject was conducted by the authors in order to better understand the key factors that may be implemented to mitigate over-height vehicle collisions with bridge components. It was observed that bridge frames and girders were the most commonly struck element of a structure. Bridge piers accounted for 10% of the 146 observed objects that were struck by vehicles in this study. It was also observed that tractor-trailers and trucks account for 95% of all vehicle impacts with bridges. Construction equipment has the highest frequency of hitting bridge components. The New York State Department of Transportation assesses the vulnerability of the state's bridges for possible failure modes due to collision through their Bridge Safety Assurance (BSA) program (NYSDOT 1995). According to this program, bridges are classified as having low, medium, or high vulnerability to failure based on the structure having

adequate collision protection systems It was observed that bridges with low vulnerability rating accounted for 46% of bridge hit cases. This suggests that even bridges thought to be well protected from vehicle collisions still have a probability of being struck.

Kamaitis (1997) discusses the effects that vehicle collisions with bridges have on society. A major end result of a vehicle-bridge collision is the economic impact that a damaged bridge has on the general public. It is suggested that the main consequences of vehicle bridge collisions are the cost of repairing or replacing the damaged bridge, cost of the damage to the colliding vehicle and any goods that were being carried, cost of injuries or fatalities, cost involved with reorganizing and detouring the traffic during the repair or reconstruction period, local business and social losses due to disruption of the detoured traffic, and the cost of the damage to the surrounding environment. The authors observed that many of the bridges constructed in the 1970's and 1980's no longer met the vertical clearance required by more recent design specifications in 1997; resulting in an increase of over-height vehicle impacts with bridges. It was also suggested that the impacting force caused by the vehicle could be interpreted as a dynamic force as a function of the vehicle mass and speed before and after impact.

Sharma et al. (2012) studied the response of reinforced concrete columns subjected to vehicle collisions and evaluated the amount of damage in them based on the performance of the column after the impact. The behavior of the impacted columns was divided into four damage categories and three performance levels. The damage levels ranged from insignificant damage to total collapse. The performance levels were defined as fully operational with no damage, operational with damage, and collapse prevention. The impact scenarios were ranked as low, moderate, and severe depending on the mass

and velocity of the impacting vehicle. The performance-based design aims to improve the behavior of the column to ensure that performance levels are met at varying levels of damage. The finite element code LS-DYNA was used to simulate four different vehicle types impacting a circular reinforced concrete pier. The dynamic shear force demand on the reinforced concrete column was analyzed, and it was concluded that the dynamic shear force demand increased with vehicle mass and impact velocity. The authors suggest that a hinge is formed at the location of impact when the dynamic shear force velocity exceeds the design shear force capacity, and that the safety of an existing bridge can be evaluated by comparing the design shear force capacity to the calculated dynamic shear force demand that results from an impact.

2.1. Finite Element Modeling of Vehicle Collisions

Murray (2007) developed a concrete material model that could be used during high speed, short duration impact events. The model was a continuous surface cap, elasto-plastic damage material model, with strain rate effects, for concrete that is used with the finite element code LS-DYNA. The material model was developed to represent the concrete in bridge rails and portable barriers subjected to vehicle collisions. The concrete model is capable of modeling strain rate effects, ductile and brittle damage, and stiffness and strength recovery.

Murray et al. (2007) evaluated the elasto-plastic damage material model developed for the finite element code LS-DYNA. The material model was validated by correlating the analysis results with experimental test data. The validation models consisted of drop tower impact of one-third-scale beams, bogie vehicle impact of full-scale reinforced concrete beams, pendulum impact of bridge rails, and quasi-static

loading of a safety-shaped barrier. The results of the numerical models accurately matched the results of the experimental tests for most cases and required the adjustment of some of the material parameters in others. The most critical material properties were found to be the facture energies, rate effect on fracture energy, and the maximum principal strain at which erosion occurs. A simplified version of the material model is available that uses default values determined by the mass density, unconfined compressive strength, and maximum aggregate size of the concrete mix. The accuracy of this concrete model was validated by the authors and will be used for conducting research.

Malvar and Crawford (1998) investigated the effect of high strain rates on the yield stress of steel reinforcing bars. It was observed that as the strain rate increases the yield stress of the reinforcing bar increases log-linearly. They proposed a formulation that could be used to determine the dynamic increase factor (DIF), the ratio of dynamic to static yield stress values, for steel reinforcement. The formulation is only valid for bars with yield stress between 290 and 710 MPa and for the range of strain rates between 10^{-4} and 225 s^{-1}. These formulas will be used to model the increase of strength for steel reinforcement bars under dynamic loading.

El-Tawil et al. (2004) investigated the accuracy of using the finite element code LS-DYNA to study vehicle collisions with bridge piers. Two vehicle models were used in this study; the Chevy C-2500 pickup truck and the Ford F800 single-unit truck. These vehicles have been validated for the use of crash analysis simulations and are available through the National Crash Analysis Center (NCAC). The dynamic force time-histories were recorded during the impact simulations with the trucks traveling at impact speeds

ranging from 55 to 135 km/h. The results of the impact simulations showed that the computed equivalent static forces generated from the collisions of both vehicles could be greater than the design collision force specified by design standards. This suggests that the design vehicle collision force could have been underestimated substantially by the design specifications.

Tsang and Lam (2008) studied the effects of vehicle impacts with structural reinforced concrete columns and investigated the velocity required for a vehicle of a known mass and type to cause a particular amount of damage in a column. Instead of the traditional strength and strain-based failure criteria, the authors suggest using displacement-based criteria that can be used to estimate the velocity required for a vehicle to cause damage. According to this study, the vehicle acts as a spring by absorbing and defusing the impact energy through crushing and undergoing inelastic deformations. If the vehicle were to act more rigidly, the column would be subject to shear failure characteristics. But since the vehicle is not rigid, the column is susceptible to bending deformations and flexural failure. The study utilizes the law of conservation of energy where the kinetic energy of the moving vehicle is absorbed and dissipated partly through the parts of the vehicle that undergo damage and partly through the flexural bending and formation of a plastic hinge in the column. The total kinetic energy is equal to the amount of energy absorbed through the crushing of the vehicle and deformation of the column.

Fujikake et al. (2009) conducted an experimental study to investigate the response of reinforced concrete beams subjected to an impact load. The experimental study consisted of three reinforced concrete beams having different longitudinal reinforcement

ratios and subjecting them to an impact of a drop hammer. The drop hammer had a hemispherical striking head with a 90-degree radius and a mass of 400 kg, and was dropped freely at heights ranging from 0.15 to 1.20 m. The major mode of failure in the test specimens was flexural failure. A nonlinear analysis was conducted to determine the relationship between load and mid-span deflection of reinforced concrete beams subjected to impact loads. The nonlinear analysis considered the strain rate effect of concrete and steel under rapid loading. The analytical method correlated well with the experimental test results. The experimental tests showed that the failure mode of the beams under impact loading was significantly affected by the ratios of longitudinal reinforcement. Flexural failure was the dominant mode of failure in the beam but as the amount of longitudinal reinforcement increased, it was observed that there was some local failure at the point of impact.

Mohammed (2011) studied reinforced concrete members under impact loading and how carbon fiber reinforced polymers could be used to rehabilitate aging structures. The finite element code LS-DYNA was utilized to study the response behavior of vehicle collisions with bridge piers and reinforced concrete beams subjected to impact loads. The Chevy C2500 pickup truck and Ford F800 single-unit truck were used to impact a single hammerhead type pier in the simulations. The impact simulations were validated by comparing the analytical results with rigid wall impact experiment data published by the NCAC to validate the C1500 vehicle model.

Adhikary et al. (2012) studied the behavior of reinforced concrete beams subject to various rates of concentrated loading through experimentation and finite element modeling. Reinforced concrete beams with varying transverse reinforcement layouts were

constructed and subjected to low, medium, and high rates of loading. The finite element code LS-DYNA was used to simulate the experimental test. The Karagonzian and Case concrete model was used to represent the solid concrete elements. The piecewise linear plasticity model was used to represent the steel reinforcing bar elements. The simulation results were validated by comparing the load versus mid-span deflection and crack profile on the side surface of the beam. It was observed that increasing the strain rate applied to the beam increased its capacity. A set of equations was proposed to determine the dynamic increase factor, the ratio of dynamic to static yield stress, of the whole reinforced concrete beams under varying loading rates.

Sha and Hao (2013) studied barge impact forces with circular reinforced concrete bridge piers through experimental tests and numerical simulations. The finite element code LS-DYNA was used to create a model of a barge colliding with a single-column bridge pier with a lumped mass on top to represent the mass of the superstructure. A parametric study was conducted to observe the effects of the pier support conditions, barge impact velocity, barge mass, pier diameter, superstructure mass supported by the pier, pier height, and location of impact. The pier support conditions were modeled in three ways: (1) fixed, (2) supported on a rigid pile foundation, and (3) supported on an elastic pile foundation. For the pile-soil-foundation models, the steel piles and soil-pile interactions were represented with beam elements and nonlinear discrete spring elements, respectively. The soil springs were applied in pairs equally spaced along the length and perpendicular to the pile shaft. It was observed that the impact force throughout the collision did not vary based on the support conditions, but the displacement response of the pier was dependent on the support conditions. The authors suggest using a detailed

model of the pile foundation to accurately capture the displacement response of the pier subjected to an impact load. The study showed that, as the impact velocity increased, the impact forces and displacements of the pier also increased. It was observed that as the mass of the barge increased the duration of the impact increased, but it did not significantly affect the peak impact force. The diameter of the circular piers had almost no effect on the peak impact force because the area of impact hardly changes with an increase in diameter. This observation does not hold true for rectangular piers due to the increase of contact area with an increase in the cross-sectional area. An increase in the mass of the superstructure was observed to decrease the displacements at the top of the pier and at the location of impact. As the location of the impact moved up along the pier, the bending moment and peak displacement increased.

Agrawal et al. (2013) investigated the effects of a vehicle impacting a bridge pier to observe the response of the entire bridge structure. The finite element code LS-DYNA was used to develop a model to simulate a vehicle impact with a three-span steel girder bridge with reinforced concrete piers. The pier consisted of a series of three rectangular columns. The model of the bridge consisted of the superstructure, substructure, and the foundation piles. The Ford F800 single-unit truck, developed by the NTRCI, was implemented into the model. The total energy in the system was monitored and recorded to assure that the amount of kinetic energy applied by the moving vehicle matched the amount of energy absorbed by the bridge and the vehicle. A parametric study was conducted considering the effects of vehicle velocity, pier diameter, and angle of incidence. It was observed that the peak impact force is always greater when the impact load is modeled using a dynamic impact force time-history rather than the 2,669 kN ESF

required by AASHTO LRFD (2012). A performance assessment of the vehicle impact was developed based on the observed failure modes in the bridge columns. The damage in the columns was categorized as minor, moderate, and severe. Minor damage was represented with spalling of the concrete cover and minor inelastic deformations in reinforcement. Moderate damage was represented with shear cracking of the concrete core and severing of the confining reinforcement. Severe damage was represented with buckling of longitudinal reinforcement, crushing of the concrete core, plastic hinge formation in the pier, and flexural failure in the bent cap. The different damage states corresponded to various damage ratios, calculated by dividing the peak dynamic impact force by the shear capacity of the pier. The various damage ratios could be used to design bridge piers to ensure different performance levels are met resulting from a vehicle impact event.

2.2. Design Standards and Their Development

Buth et al. (2010) conducted an analysis of vehicle collisions with bridge columns to determine the maximum peak load generated during the collisions and observe the distribution of impact forces along the height of the column. The primary mode of failure in bridges that have been struck by vehicles is shear failure of the impacted column; usually resulting in two 45-degree shear planes originating from the location of impact. A finite element model was created using LS-DYNA to simulate a 29.5 Mg single-unit truck and a 36.3 Mg tractor-trailer impacting rigid bridge columns. The single-unit truck simulation was used to identify that the greatest concentration of impact forces along the height of the column occurred at 1.524 m above the ground. The tractor-trailer simulation was used to determine the largest impact force that could possibly be generated during a

vehicle collision with a bridge pier. From the simulation, it was observed that the maximum force that was generated was greater than the 1,779 kN force recommended in the 5th edition of the AASHTO LRFD Bridge Design Specifications (2010). This findings raised concerns that the design specifications did not adequately account for the forces generated during a vehicle collision. A full-scale crash test was proposed to determine a realistic impact force when a fully loaded tractor-trailer impacts a bridge pier.

Buth et al. (2011) conducted two full-scale crash tests to record the force generated when a 36.3 Mg tractor-trailer impacts with a rigid bridge pier. The column was made rigid to record the maximum impact force that could be generated during the collision. The results of the impacting force was compared to the collision force required for design by the AASHTO LRFD; 1,779 kN applied at 1.219 m above the ground in any direction transverse to the column. After conducting the full-scale experiment, it was recommended that the design equivalent static vehicle collision load be increased to 2,669 kN applied at a height of 1.524 m at an angle of incidence of 0 to 15 degrees from the edge of the pavement.

The following design provisions arose from the full-scale crash tests and finite element modeling conducted by Buth et al. (2010 and 2011) and the Texas Transportation Institute. The American Association of State Highway and Transportation Officials (AASHTO) *Load and Resistance Factor Design (LRFD) Bridge Design Specifications* (2012) requires that abutments and piers within 9.144 m of the roadway to be considered for the extreme event of a vehicle collision. Those bridge structures found susceptible to vehicle collision forces must be designed to either redirect or absorb the impact force or provide structural resistance. When designing for structural resistance, the bridge

structure must be designed to resist an equivalent static force (ESF) of 2,669 kN applied as a single point load at a height of 1.524 m above the ground and at an angle of incidence from zero to 15 degrees with the edge of pavement in a horizontal plane. These design provisions are located under Section 3.6.5.1-Protection of Structures (AASHTO 2013).

CHAPTER 3.

VEHICLE IMPACT FORCE

A vehicle collision with a bridge column is a complex interaction. The forces generated by the impact have to be absorbed and resisted by the column, as well as the colliding vehicle, to assure the stability of the bridge structure. The impact energy is dissipated through heat, sound and the deformation of the vehicle and bridge column. The following chapter describes how the vehicle impact force is determined and dissipated during the impact event.

3.1. Stages of Vehicle Collision

The impact event that occurs between a moving vehicle and a stationary bridge column could be divided into two stages. The first stage occurs during the initial time of contact between the vehicle (containing an initial velocity) and the bridge column until the vehicle and column share a common velocity and move together. The vehicle begins to crumple and absorb some of the kinetic energy. The forces developed at this point are relatively low. As the vehicle reaches a point where it cannot absorb any more energy, the rest of the kinetic energy is transferred into the bridge column. When enough energy has been transferred into the column the velocity of the vehicle matches the velocity of the column, and they begin to move together. This is when the second stage begins. The second stage occurs between the time when the vehicle and bridge column begin to move together until the time when either column failure occurs or the vehicle comes to rest. The forces developed in this stage are much larger than those developed in the first stage. Failure of the bridge column will most likely result in a shear failure at, or around, the location of impact. This shear failure will be a direct result of the crushing and in-plane

cracking of the concrete throughout the cross-section of the column. The force transferred to the column during a vehicle impact event is identified as the required force the column needs to resist. This force is highly variable and depends on the stiffness, mass, and velocity of the impacting vehicle, in addition to the design and material properties of the bridge column. (Sharma et al. 2011)

3.2. Conservation of Energy

The principle of conservation of energy states that the total amount of energy in a closed system cannot change. As a vehicle moves with a particular velocity, it contains an inherent amount of kinetic energy (KE). The KE of the moving vehicle can be calculated using the following equation,

$$KE = \frac{1}{2}mV^2 \qquad \text{Equation 0-1}$$

where m is the mass of vehicle and V is the impact velocity (Tsang and Lam 2008). The KE is transformed into work to cause displacement of the column, W_{col}, and the deformation to the vehicle, W_{veh}, resulting in the following equation of equilibrium:

$$KE = W_{col} + W_{veh} \qquad \text{Equation 0-2}$$

Energy dissipation through heat and sound are neglected as they account for a relatively small amount of the total energy in the system. Vehicles are designed to protect the passengers by dissipating energy through crumple zones; where the material in parts of the vehicle are designed to yield without causing damage to the passenger compartment. Once the vehicle itself cannot absorb any more energy through deformation, the remainder of the energy is transferred into the bridge column. The amount of KE absorbed by the bridge column is proportional to the column's stiffness and inertia at rest. Because bridge columns often possess large amount of inertia, the force required to cause

a displacement of the column is very large. As the column displaces due to the impact, work is done. The amount of work, W, done can be defined by the following equation:

$$W = Fd \quad \text{Equation 0-3}$$

where F is the force required to cause a displacement, d. The work done to move the column and deform the vehicle is at the expense of the KE resulting from the impact. Therefore, Equation 0-1 and Equation 0-3 can be combined together to result in the following equation:

$$Fd = -\frac{1}{2}mV^2 \quad \text{Equation 0-4}$$

Rearranging Equation 0-4 results in the following equation:

$$F_{impact} = -\frac{1}{2}\frac{mV^2}{d} \quad \text{Equation 0-5}$$

where F_{impact} is the impact force resulting from the vehicle collision that can be determined by the mass of the vehicle, m, impact velocity, V, and the amount of displacement, d, of the vehicle. Similar equations have been developed in the *LRFD Bridge Design Specifications* for vessel collisions (AASHTO 2013).

3.3. Equivalent Static Force

The dynamic impact force time-history that results from a vehicle collision fluctuates in magnitude rapidly with many peaks. The peaks are a result of various parts of the vehicle coming into contact with the pier or a portion of the vehicle that has crumpled, transferring more kinetic energy into the column. The peak dynamic impact force observed in the force time-history is the maximum force that occurs; usually resulting from the impact of the vehicles engine block. The peak event occurs over an extremely short period of time where the structure cannot respond to the rapid rate of the

applied forces. According to El-Tawil et al. (2005), since the peak impact force occurs in such a short time duration and does not cause instantaneous displacement of the column, it cannot be used to determine the structural demands of the bridge column. Many design specifications have been determined using a 50 ms moving average to determine an equivalent static force (ESF) for vehicle collision (Buth et al. 2011). Alternatively, a dynamic analysis is conducted to determine an ESF to represent a more realistic structural demand on bridge columns subjected to elastic deformations.

An ESF is the external static force required to cause a known displacement resulting from a dynamic force. The ESF is a simplification of the complex dynamic loads generated during an impact event. The following equation is used to determine the equivalent static force, f_s, resulting from a dynamic impact event,

$$f_s = ku \qquad \text{Equation 0-6}$$

where k is the stiffness of the column and u is the resulting displacement (Chopra 2012). Calculating the ESF will determine whether or not the vehicle collision exceeds the design standards. This method of determining design loads can be used in piers subjected to elastic loading conditions. Significant displacement caused by material plasticity will not provide an appropriate equivalent static force that can be used for design.

The preceding equations are used to show how vehicle impact velocity and the stiffness of a structure influence the impact force. As the vehicle impact velocity increases, the kinetic energy that needs to be resisted by the pier and the vehicle also increases, resulting in an increase in impact force. As the stiffness of a structure increases, more force is required to cause the same amount of displacement. A stiffer pier is able to resist more impact force because more energy is needed to displace it.

CHAPTER 4.

VALIDATION OF FINITE ELEMENT MODELS

An important aspect of using finite element analysis for research is validating that the model accurately represents what is being depicted. Physical characteristics such as geometry, material properties, and boundary conditions have to be modeled to match precisely that of the experimental test setup. The model can be validated by matching displacements and forces with experimental results. Since experimental data for vehicle collisions with bridge piers was very limited, an experiment representing a similar impact phenomenon was used for validation purposes. In the current study, the series of experiments conducted by Fujikake et al. (2009) were used to validate finite element controls and material properties for use with vehicle impact simulations. The experiment consisted of a reinforced concrete beam subjected to a drop hammer test. The hammer was dropped at different heights where mid-span deflections and impact forces were recorded and used for validation. The following finite element models were created in units of N, mm, and seconds.

4.1. Beam Impact Experiment Setup

A series of reinforced concrete beams with a depth of 250 mm, width of 150 mm, and length of 1,700 mm were subjected to impact loads (Fujikake et al. 2009). Figure 4.1 shows the layout of the steel reinforcement cage and dimensions of the test beams. A concrete cover of 40 mm was provided around the reinforcement cage, except at the ends which had 25 mm of cover. The concrete beams were reinforced with four longitudinal reinforcing bars, two in compression and two in tension, and 23 transverse reinforcing bars spaced 75 mm apart. Three types of beams were modeled, each with a different ratio

of longitudinal reinforcement to gross cross-sectional area of the beam, ρ. The first beam, S1616, consisted of D16 bars in compression and tension for a ρ of 2.12%. The second beam, S1322, consisted of D13 bars in compression and D22 bars in tensions for a ρ of 2.40%. The third beam, S2222, consisted of D22 bars in compression and tension for a ρ of 4.13%. All transverse reinforcing bars consisted of D10 bars with yield strength of 295 MPa. The D13, D16, and D22 longitudinal reinforcing bars had yield strengths of 397, 426, and 418 MPa, respectively. It was assumed that the three reinforced concrete beams would be flexure controlled beams because the estimated bending resistance was less than that of the shear resistance according to the Japan Society of Civil Engineers (JSCE) Concrete Standard (Fujikake et al. 2009). The concrete compressive strength at the time of testing was 42.0 MPa. Table 0-1 shows the mix proportion of the ready mixed concrete for the reinforced concrete beam specimens. The maximum aggregate size in the concrete was 10 mm. The beams spanned 1,400 mm and were supported by two specially designed support devices which allowed free rotation of the beam but prevented the beam from displacing longitudinally and vertically. Figure 4.2 shows the drop hammer test setup.

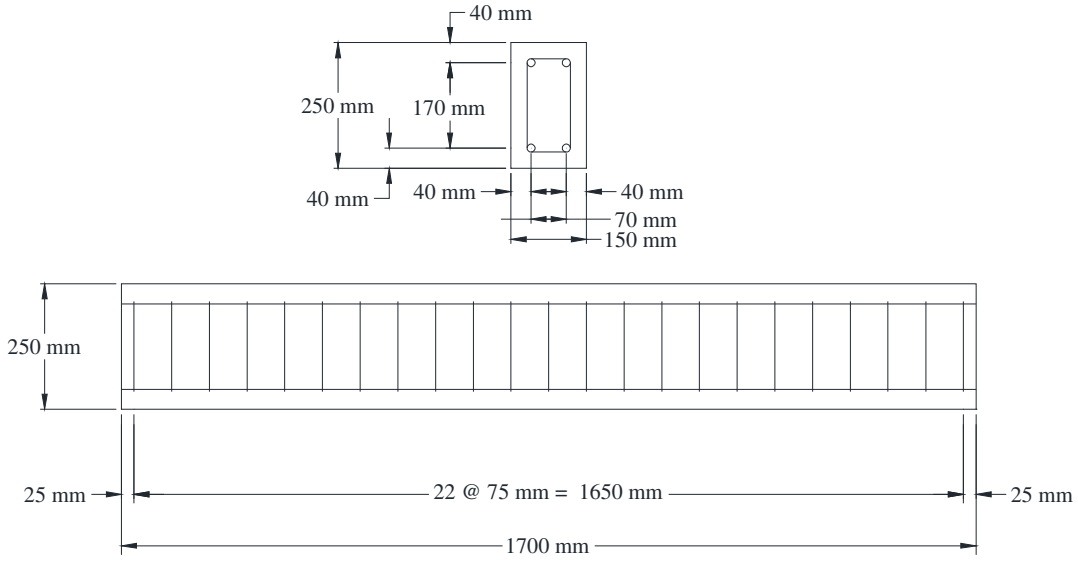

Figure 4.1. Schematic illustration of the beam cross-section (top) and side view (bottom)

Table 0-1. Ready mixed concrete mix portion

W/C	Unit Weight (kg/m^3)					Air	Slump
(%)	W	C	S	G	Ad	(%)	(cm)
44.5	185	416	726	943	4.16	4.5	15.5
Note: W = Water; C = Cement; S = sand; G = Gravel; Ad = Admixture							

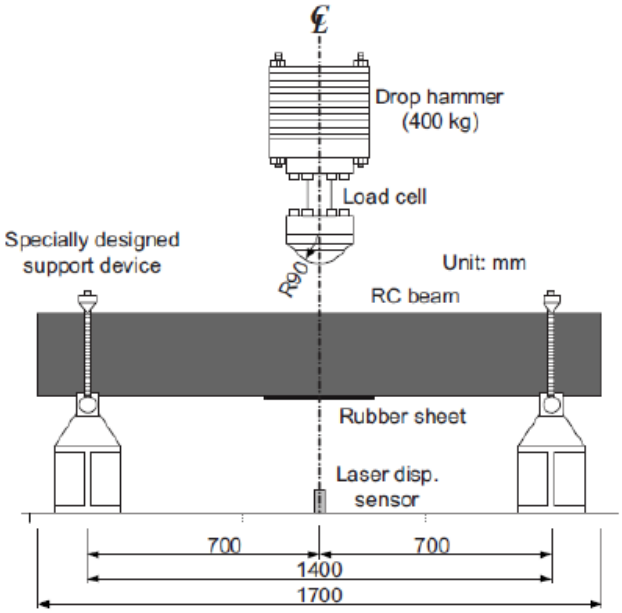

Figure 4.2. Drop hammer impact test setup (Fujikake et al. 2009)

The reinforced concrete beam specimens were subject to impact loads using a drop hammer impact loading machine. The drop hammer had a hemispherical striking head with a radius of 90 mm and mass of 400 kg. The hammer was dropped freely onto the top surface of the reinforced concrete beam at mid-span. The S1616 beam was subject to drop heights of 0.15, 0.30, 0.60, and 1.20 m. The S1322 and S2222 beams were subject to drop heights of 0.30, 0.60, 1.20, and 2.40 m.

The beam impact experiment was modeled using the advanced general purpose multiphysics simulation software package LS-DYNA. This software was selected because it has been widely used to study impact loads and vehicle collisions. The preprocessing consists of creating the geometry, material models, boundary conditions, and all other model parameters. The post-processing consists of analyzing the results.

4.2. Geometry

The finite element model of the beam impact test setup is presented in Figure 4.3. The geometry of the reinforced concrete beam was created with the shape mesher tool. A breakdown of the finite element model showing the steel reinforcement cage, the concrete core, concrete cover, and drop hammer sphere are shown in Figure 4.4. The concrete portion of the beam was created using eight node, constant stress, single-point integration solid hexahedron elements. Single-point integration, constant stress solid elements were selected because they are computationally efficient. The length of the beam was divided into 68 elements, each 25 mm in length. The cross section of the beam was discretized into finite elements, as shown in Figure 4.5, where the size of the elements ranged from 17.5 to 21.25 mm. The steel reinforcement cage was created using two node, Hughes-Liu with cross section integration, 2×2 Gauss quadrature, tubular beam elements. These beam elements were selected because they allow finite element strains to occur, are simple and computationally efficient, compatible with brick elements, and include finite transverse shear strains (LSCT 2006). The beam elements had an outer diameter that corresponded to the diameter of the reinforcement bar being represented and an inner diameter of zero. The beam elements coincided with the nodes that defined the solid elements, therefore it was assumed that the concrete and steel reinforcement bars formed a perfect bond. Figure 4.6 shows the beam elements coinciding with the solid element mesh. There are 6,528 solid elements, 824 beam elements, and 8,893 nodes that make up the finite element model of the reinforced concrete beam. The drop hammer was modeled using eight node, constant stress, single-

point integration solid elements. The drop hammer consisted of 3,584 solid elements and 3,817 nodes. In total, the model consists of 10,936 elements and 12,710 nodes.

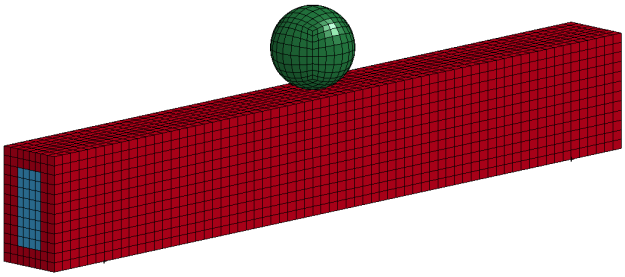

Figure 4.3. Finite element model of reinforced concrete beam and drop hammer

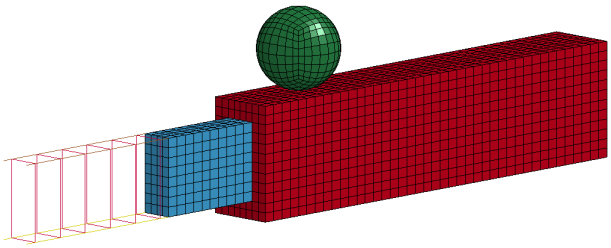

Figure 4.4. Breakdown of finite elements in the reinforced concrete beam

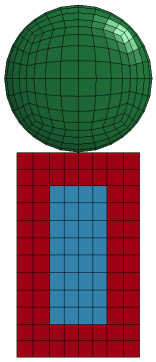

Figure 4.5. End view of finite element beam and drop hammer sphere

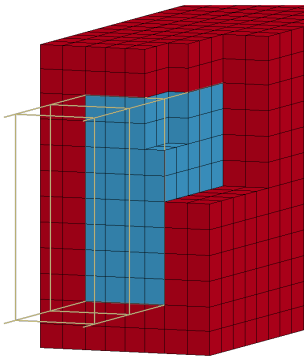

Figure 4.6. Beam elements coinciding with the solid element mesh

4.3. Material Models

4.3.1. Concrete

The concrete behavior of the beam was modeled using material model 159 (Mohammed 2011). This is a continuous surface cap model that was developed, evaluated, and validated for use by the Federal Highway Administration to predict the dynamic performance of concrete used in roadside safety structures subjected to vehicle collisions (Murray et al. 2007). The material model defined the required strength, stiffness, hardening, softening, and rate effect parameters as a function of concrete density, compressive strength, and maximum aggregate size. A viscoplastic formulation is used to model an increase in strength of the elements with an increasing strain rate. The size of the elements has no effect on the models ability to maintain constant fracture energy (LSTC 2013). Damage to the concrete elements is tracked through ductile and brittle damage parameters. Ductile damage occurs when stress is applied to the element in compression. Brittle damage occurs when stress is applied to the element in tension. The damage parameters range from 0, no damage, to 1, complete damage. Damage is initiated when strain-based energy terms exceed a specified damage threshold. The strength and stiffness of an element will be equal to zero when one of the damage parameters approaches a value of 1. The concrete that was modeled had a mass density of 2,274 kg/m^3, an unconfined compressive strength of 42 MPa, and a maximum aggregate size of 10 mm.

4.3.2. Steel Reinforcement

The steel reinforcing bars were modeled using material model 24; an elasto-plastic material model that accounts for a stress-strain curve and strain rate dependency. The material properties that had to be input for each different size reinforcement bar include mass density, modulus of elasticity, Poisson's ratio, yield stress, the stress-strain curve, and the strain rate scaling effect on the yield stress curve. All sizes of reinforcing bars had a mass density of 7,850 kg/m^3, a modulus of elasticity of 200 GPa, a tangent modulus of 1.5 GPa, and a Poisson's ratio of 0.30. The yield stress of the D10, D13, D16, and D22 bars were defined as 295, 397, 426, and 418 MPa, respectively. The stress-strain behavior was considered bilinear and is presented in Figure 4.7.

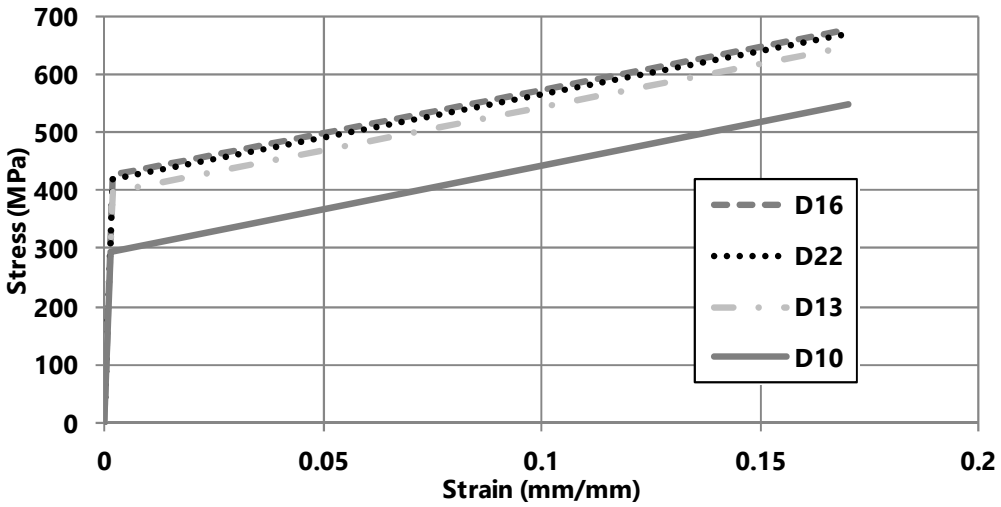

Figure 4.7. Bilinear stress strain curve for the reinforcement bars

At high strain rates, such as those experienced during blast loading and vehicle impacts, the yield strength of reinforcing bars can increase by 100% depending on the grade of the steel. The amount of increased yield stress is determined by the dynamic increase factor (DIF); the ratio of dynamic to static yield stress values. Malvar and Crawford (1998) collected data on dynamic tests conducted on steel reinforcement and proposed the following equations to determine the DIF of steel reinforcing bars:

$$DIF = \left(\frac{\dot{\varepsilon}}{10^{-4}}\right)^{\alpha}$$ Equation 0-1

for yield stress, $\alpha = \alpha_{fy}$ is expressed as follows:

$$\alpha_{fy} = 0.074 - 0.040\frac{f_y}{414}$$ Equation 0-2

for ultimate stress, $\alpha = \alpha_{fu}$ is expressed as follows:

$$\alpha_{fu} = 0.019 - 0.009\frac{f_y}{414}$$ Equation 0-3

where f_y is the bar yield strength in MPa. These equations are only valid for yield stresses between 290 and 710 MPa, and for strain rates between 10^{-4} and 225 s^{-1} (Malvar and Crawford 1998). The DIF was determined for each of the four sizes of steel reinforcement and are presented in Figure 4.8. A curve was defined for each reinforcement bar that was attached to each bar's material card. To assure that the strain rates were accounted for accurately, the viscoplastic formulation was also defined for each reinforcement bar.

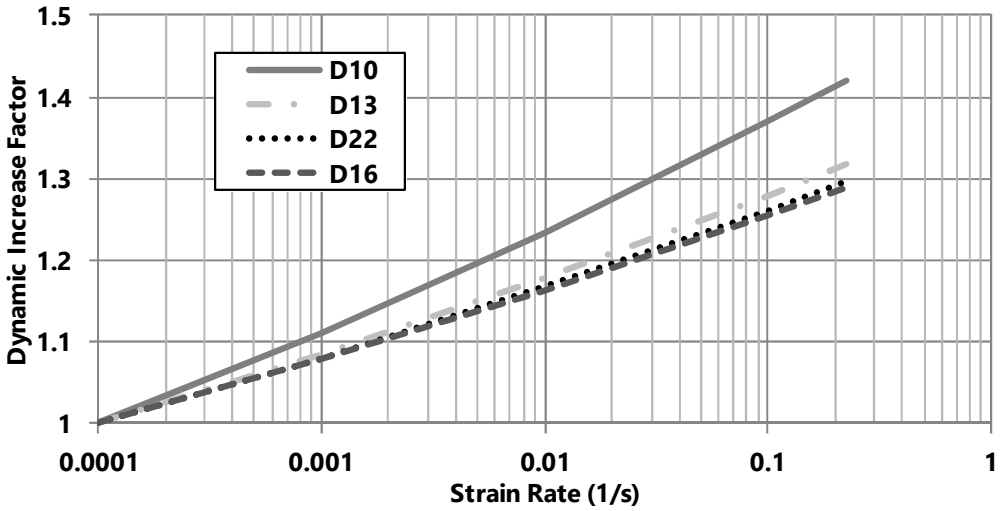

Figure 4.8. Dynamic increase factor due to strain rate effects

4.3.3. Drop Hammer

The drop hammer was assumed to act rigidly and was modeled using material model 20. Even though the drop hammer is modeled as rigid, reasonable values for the modulus of elasticity and Poisson's ratio have to be specified in the input parameters. The drop hammer had volume of approximately 0.003 m^3 and a mass of 400 kg, therefore the mass density input was 133,500 kg/m^3.

4.4. Finite Element Modeling Controls

The accuracy of the finite element model is highly dependable on the finite element controls, such as boundary conditions, initial conditions, contact between objects, and analysis controls. The following section describes how these conditions were accounted for in the modeling process.

4.4.1. Boundary Conditions

The beams used in the beam impact experiment had a span of 1,400 mm, supported by a specially designed device to allow free rotation while restraining displacement. Therefore, the beams were assumed as pinned-pinned. Single point constraints were applied to constrain nodal displacement in the X, Y, and Z directions on the nodes located on the bottom side and 150 mm from the ends of the beam.

4.4.2. Initial Conditions and Loads

An initial velocity was applied to the drop hammer corresponding to the drop height for a particular simulation. The following equation was used to determine the impact velocity of the drop hammer from free fall,

$$v = \sqrt{2gh}$$ Equation 0-4

where g is the acceleration due to gravity (9.806 m/s^2), h is the free fall height (m), and v is the impact velocity (m/s) (Fujikake et al. 2009). For drop heights of 0.15, 0.30, 0.60, 1.20, and 2.40 m, the corresponding impact velocities were 1.72, 2.43, 3.43, 4.85, and 6.86 m/s, respectively. The gravitational acceleration due to gravity was assigned to the system by defining a linear, horizontal curve to represent the acceleration due to gravity (9.806 m/s^2).

4.4.3. Contact

The finite element code requires that the contact surfaces between two colliding objects be defined. In order to transfer forces and velocities accurately, the proper master and slave parts had to be defined. The master part, the drop hammer, was defined to transfer its energy and velocity to the slave part, the reinforced concrete beam. The static coefficient of friction, dynamic coefficient of friction, and exponential decay coefficient between the steel hammer head and the concrete surface of the beam was defined as 0.5, 0.3, and 0.001, respectively.

4.4.4. Analysis Control

LS-DYNA requires an end time to determine whether the analysis has run for a sufficient amount of time to acquire a desired solution. A termination time of 0.035 seconds was selected because it adequately captured the impact and response from the drop hammer experiment.

The Flanagan-Belytschko stiffness form with exact volume integration for solid elements hourglass control was utilized to account for the nonphysical, zero-energy modes of deformation that produce zero strain and no stress.

4.4.5. Hourglass Energy Control

Hourglassing refers to nonphysical, zero-energy modes of deformation in solid, shell, and thick shell elements with a single integration point. Hourglass modes result in zero strain and no stress modes. Examples of hourglass modes for solid elements are shown in Figure 4.9. Hourglassing can be eliminated from the solution by implementing fully integrated elements but at the expense of longer analysis time. Single point integration elements are more commonly used because they are much faster to analyze, and with the implementation of hourglass control algorithms hourglass is minimized to a tolerable amount; usually less than 10% of the total energy of the system (Bala and Day 2004). The hourglass control algorithms apply internal forces to resist the hourglass modes and result in hourglass energy that is taken away from the physical energy of the system. Hourglass energy is controlled by viscous and stiffness formulations. Viscous and stiffness hourglass control formulations generate hourglass forces proportional to components of nodal velocity and displacement, respectively. Viscous forms are recommended for high velocity and high strain rate problems such as explosives. Stiffness forms are recommended for low strain rate problems such as crash simulations. LS-DYNA offers ten hourglass algorithm formulations that can be utilized to control hourglassing. Type 5, Flanagan-Belytschko with exact volume integration, hourglass control is a stiffness form algorithm and is used in this study to manage hourglassing in the drop hammer and vehicle impact simulations.

The hourglass coefficient is used to stiffen the response of the problem, particularly when deformations are large. The hourglass coefficient value has a

significant effect on the accuracy of the solution and was finely tuned in this study to best match the impact forces and mid-span deflections reported by Fujikake et al. (2009).

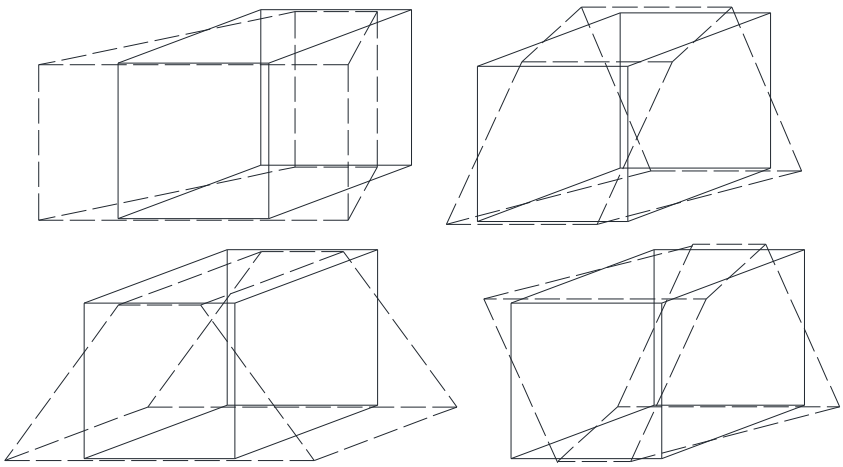

Figure 4.9. Hourglass mode examples for under-integrated solid elements (LSTC 2006)

A study was performed to observe the effect of the hourglass coefficient value on the results of the analysis. The S1616 beam with a drop height of 1.20 m was used to conduct this study. The hourglass coefficient values ranged from the default value of 0.10 to 0.001. The kinetic, internal, total, and hourglass energy distribution over time for hourglass coefficient values of 0.10 and 0.001 are shown in Figure 4.10 and Figure 4.11, respectively. It was observed that the ratio of hourglass energy to the total energy in the system is minimized as the hourglass coefficient decreased. This observation is shown in Figure 4.12. An hourglass coefficient value of 0.001 resulted in the hourglass energy accounting for a maximum of 2.2% of the total energy. This was significantly reduced from 9.6% for a coefficient value of 0.10. A reduction in the hourglass coefficient may increase the accuracy of the simulation but can also result in premature erosion of elements. Hourglass coefficient values less than 0.001 often result in the erosion of elements located near the constrained nodes. It was also observed that as the drop height increased the hourglass coefficient value had a greater effect on element erosion.

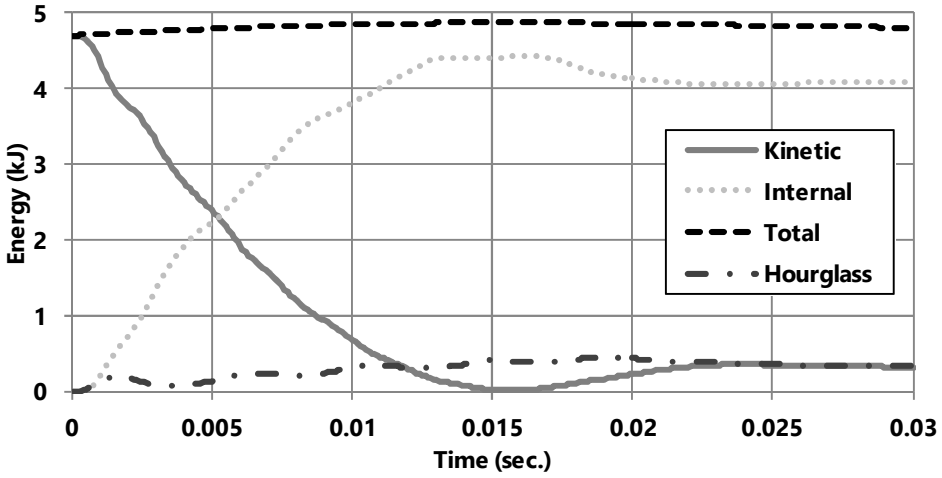

Figure 4.10. Energy distribution in the system with hourglass coefficient equal to 0.10

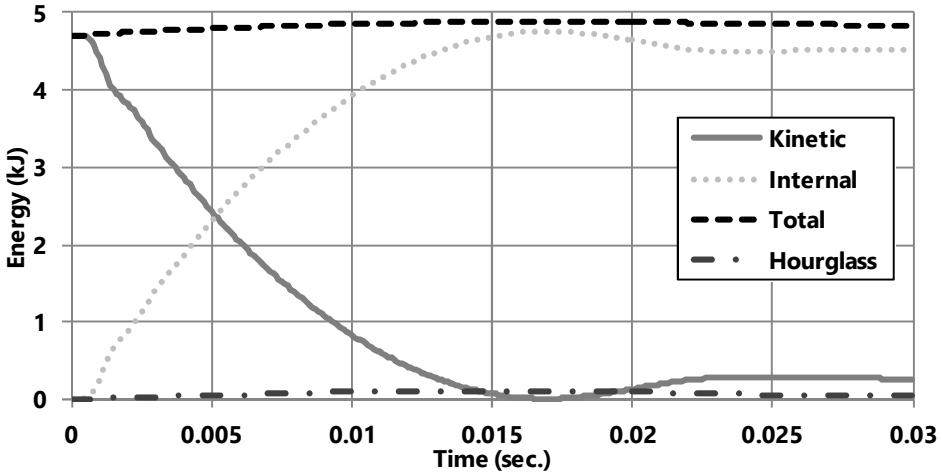

Figure 4.11. Energy distribution in the system with hourglass coefficient equal to 0.001

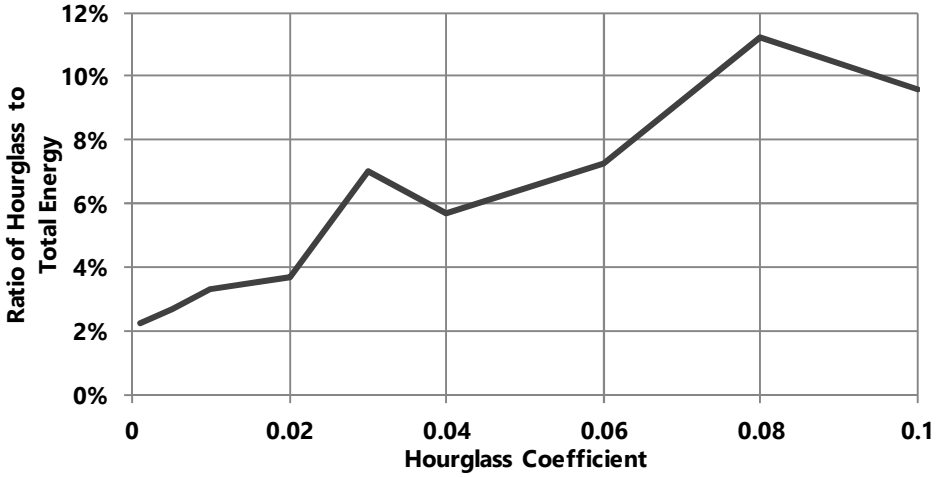

Figure 4.12. Ratio of hourglass to total system energy with respect to the hourglass coefficient

4.5. Analytical Results

The experimental results reported by Fujikake et al. (2009) were compared with the mid-span deflection and impact forces from the analyses. The S1616, S1322, and S2222 beam experimental and analytical results are presented in Figures 4.13-4.15, respectively. The average difference for mid-span displacement between the analytical and experimental results was 8.2%. Overall, the mid-span deflections matched well with the experimental results and are only off by a few millimeters. The average difference for peak impact force between the analytical and experimental results was 10.8%. Overall, the peak impact forces were in good agreement with the experimental results which indicates a realistic performance from the finite element model. The post-peak impact forces matched better with the experimental results as the drop height increased. The crack profile was observed using the plastic strain contours (Mohammed 2011). The crack patterns were in good agreement with the experimental results. The crack profiles of the analytical and experimental results are displayed in Figures 4.16-4.18.

By validating this beam impact experiment, it was concluded that the finite element procedures used in this study can be applied to developing vehicle impact simulations with bridge piers. Material models 24 and 159 can be used to represent the material properties of steel reinforcement and concrete, respectively, under dynamic impact loading simulations. An automatic surface-to-surface contact algorithm accurately captures the interaction between two impacting objects. Flanagan-Belytschko stiffness hourglass control minimizes hourglassing of under-integrated solid elements. The next chapter will consist of various validation methods used to assure the accuracy of the vehicle truck models that are available.

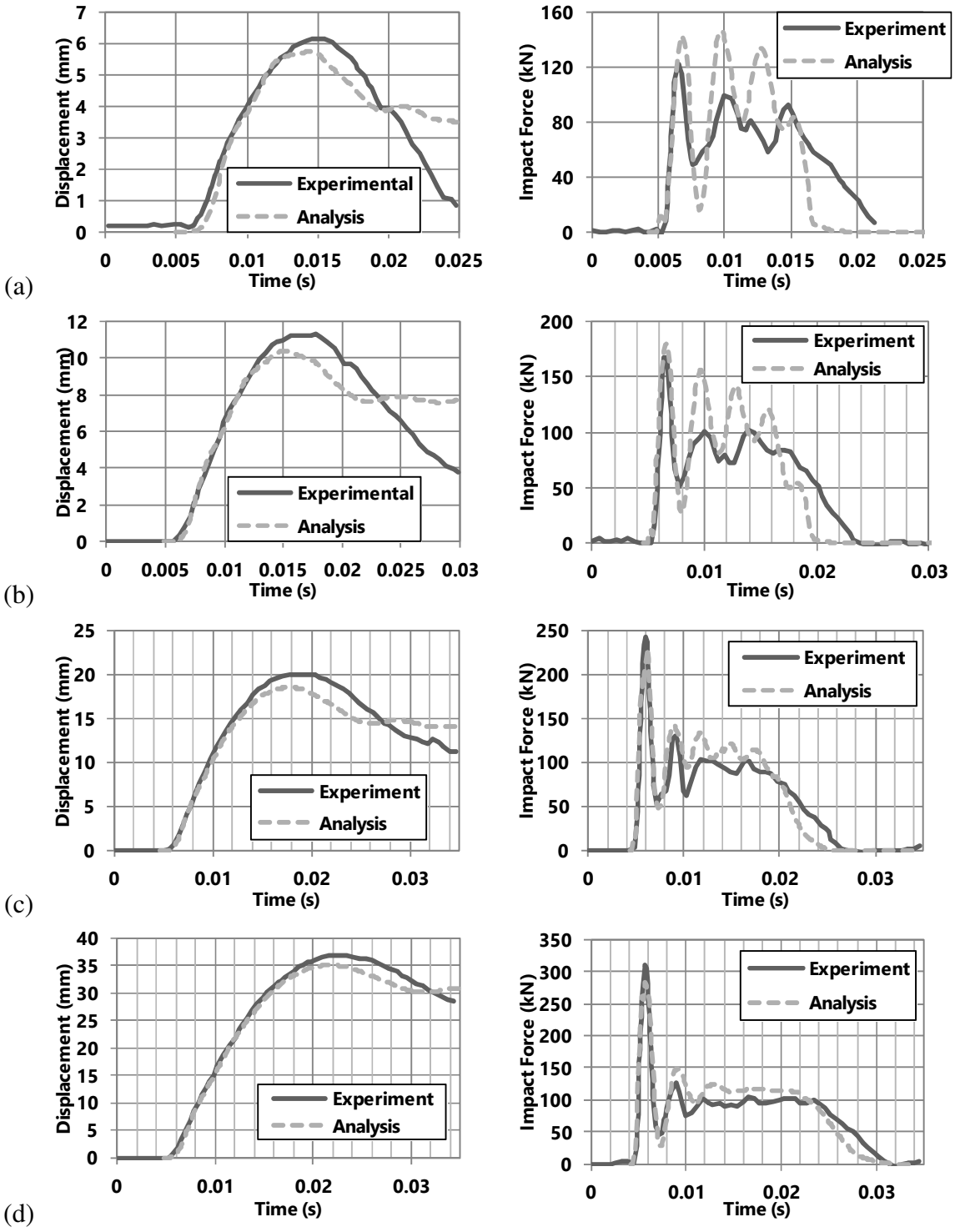

Figure 4.13. Mid-span deflection and impact force for S1616 beam for drop heights (a) 0.15, (b) 0.30, (c) 0.60, and (d) 1.20 m

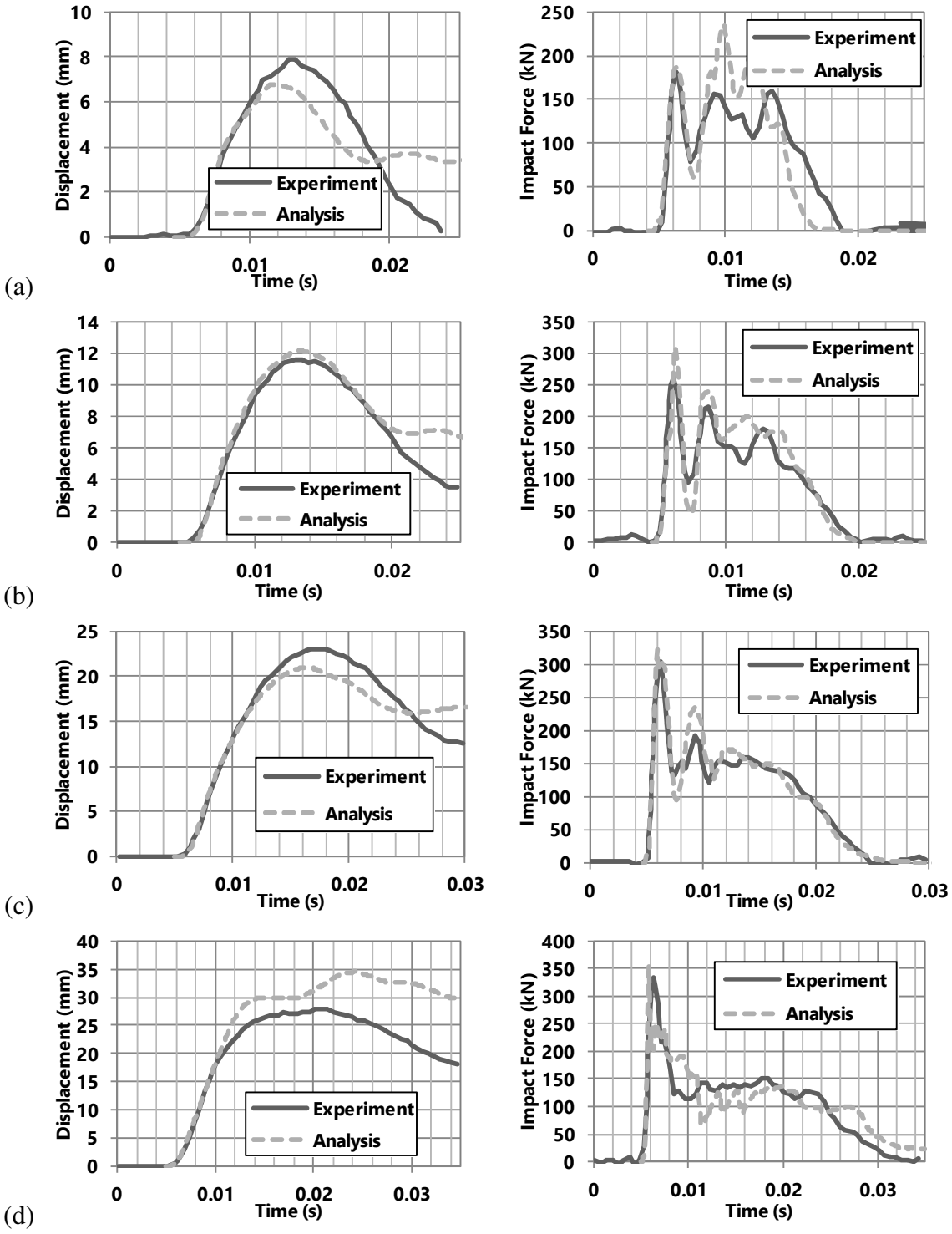

Figure 4.14. Mid-span deflection and impact force for S1322 beam for drop heights (a) 0.30, (b) 0.20, (c) 1.20, and (d) 2.40 m

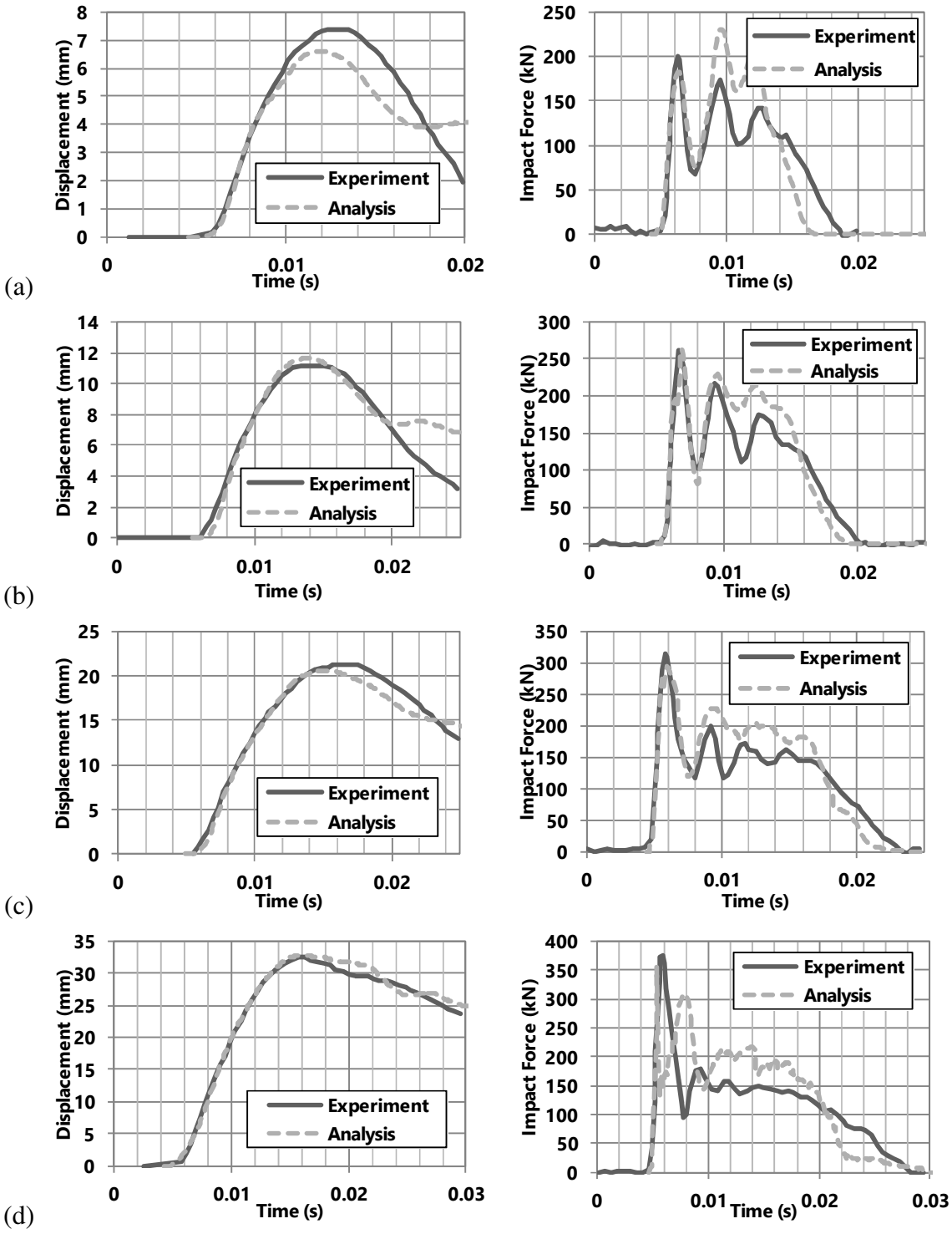

Figure 4.15. Mid-span deflection and impact force for S2222 beam for drop heights (a) 0.30, (b) 0.20, (c) 1.20, and (d) 2.40 m

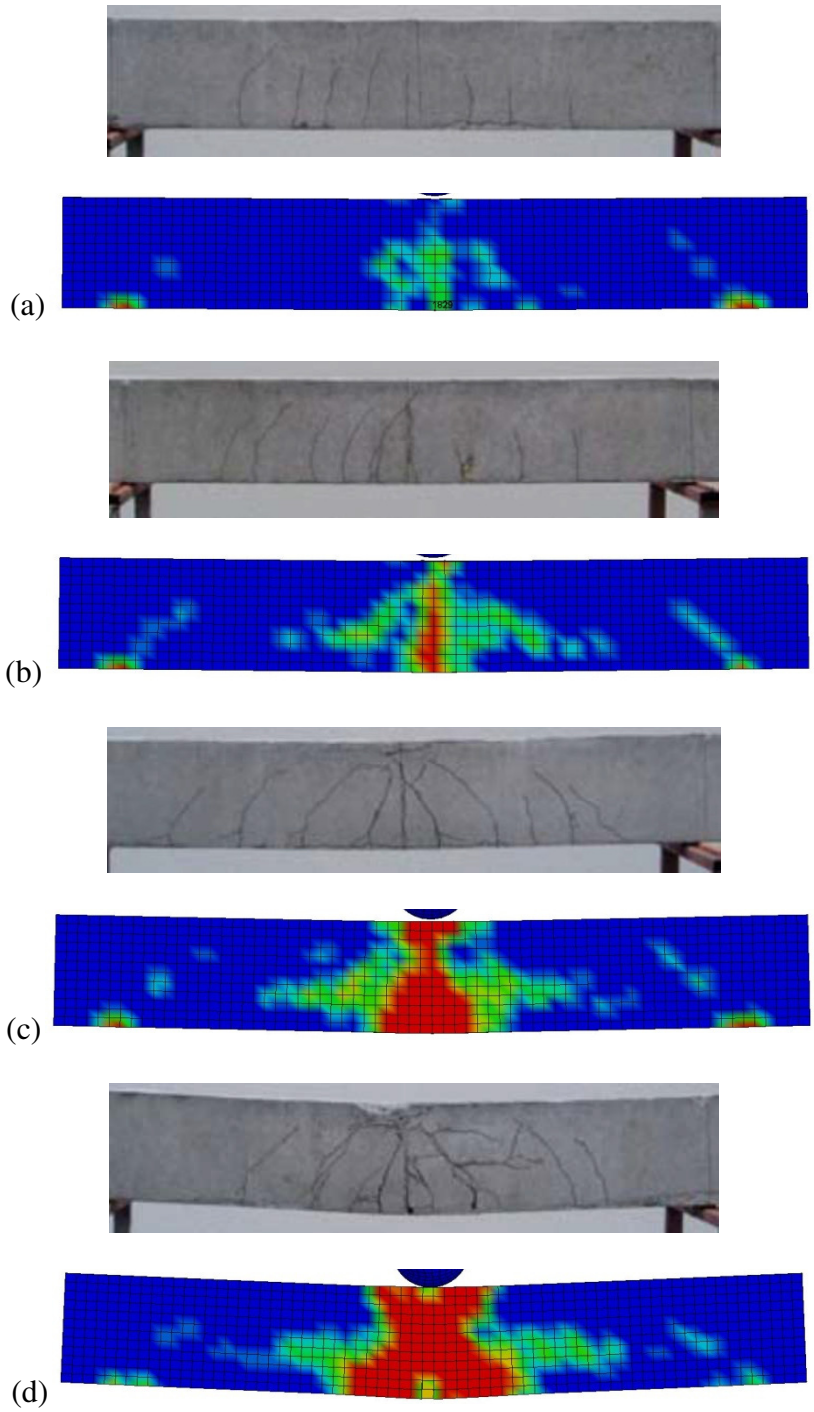

Figure 4.16. S1616 cracking at drop heights (a) 0.15, (b) 0.30, (c) 0.60, and (d) 1.20 m

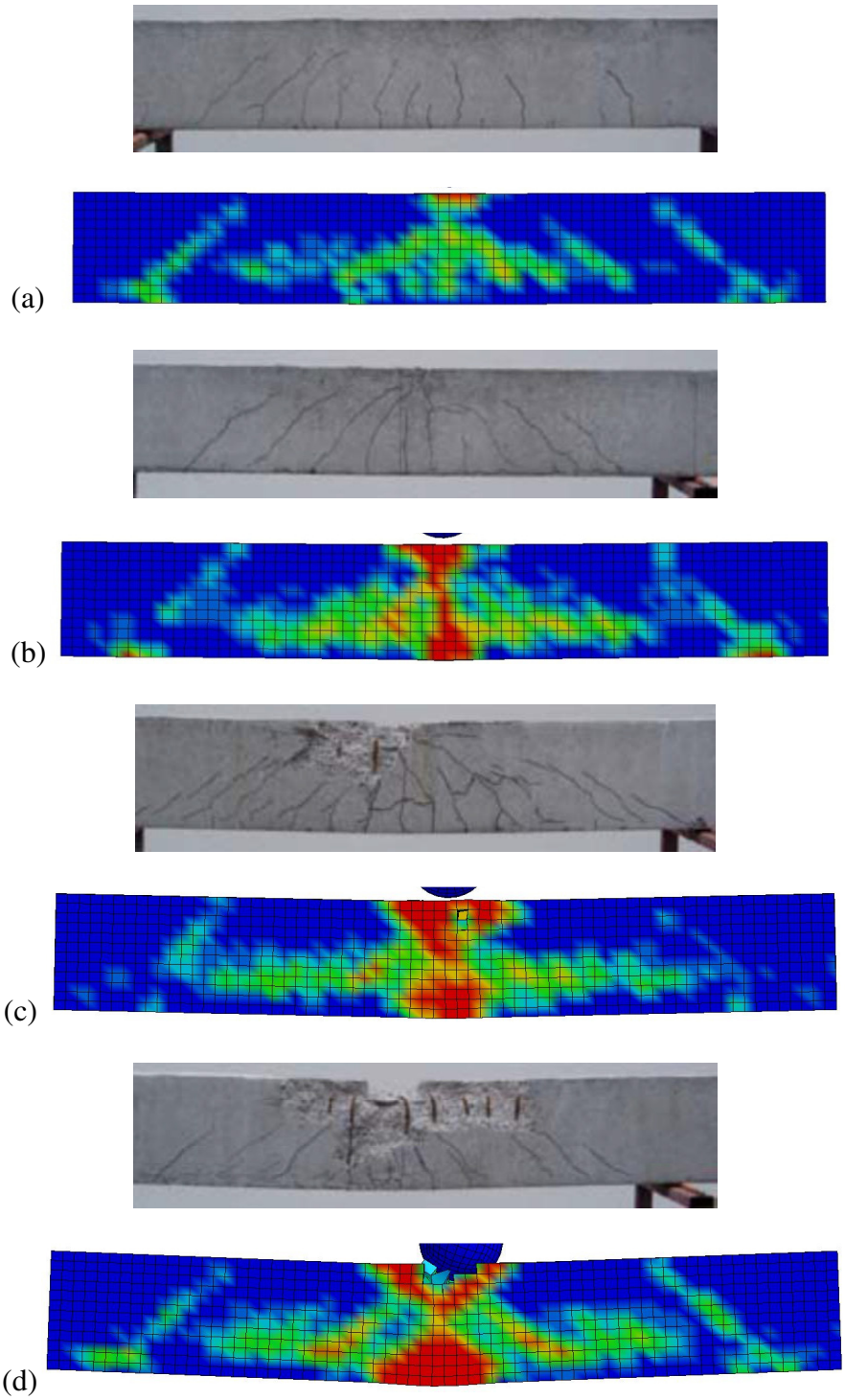

Figure 4.17. S1322 cracking for drop heights (a) 0.30, (b) 0.20, (c) 1.20, and (d) 2.40 m

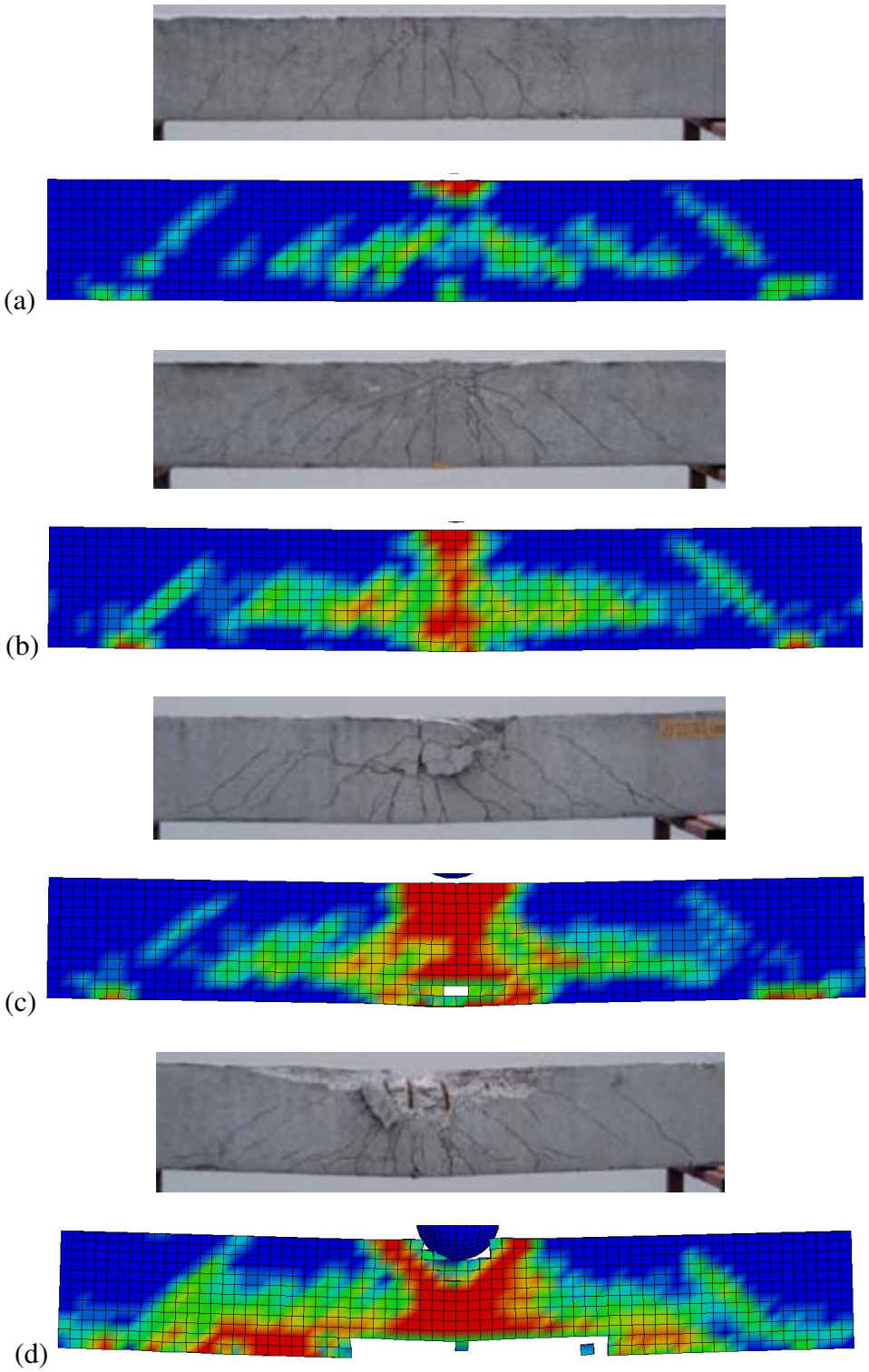

Figure 4.18. S2222 cracking for drop heights (a) 0.30, (b) 0.20, (c) 1.20, and (d) 2.40 m

CHAPTER 5.

FINITE ELEMENT MODELING OF VEHICLE COLLISIONS WITH BRIDGE PIERS

The following section outlines the process and results of the finite element modeling of the vehicle collision with bridge pier simulations. These simulations are an efficient and cost effective way of studying vehicle collisions with bridge piers. This is because many simulations can be conducted to fully understand all the mechanics involved in a collision event. Three vehicle models were investigated and validated for use in modeling vehicle collisions with bridge piers. The vehicle impact simulations were validated by comparing results to published reports using similar simulations.

5.1. Vehicle Models

Three vehicle models were used for simulating vehicle collisions with bridge piers. The three vehicles that were selected are the Chevrolet C2500 pickup truck, the Ford F800 single-unit truck, and a tractor-trailer. The reduced C2500 model, shown in Figure 5.1, had a total of 10,518 elements and a total mass of 1.84 Mg. The F800 model, shown in Figure 5.2, had a total of 35,353 elements and a total mass of 8.06 Mg. The tractor-trailer model, shown in Figure 5.3, had a total of 355,068 elements and a total mass of 13.15 Mg. These vehicles were selected because they represent light, medium, and heavy weight trucks. The vehicle models were used “as is”, meaning they were not changed in anyway; other than adjusting the initial velocity for various impact speeds. The kinetic energy generated by the moving vehicles, shown in Figure 5.4, was calculated using Equation 0-1 for the impact velocities of 55, 90, 110, and 135 km/h.

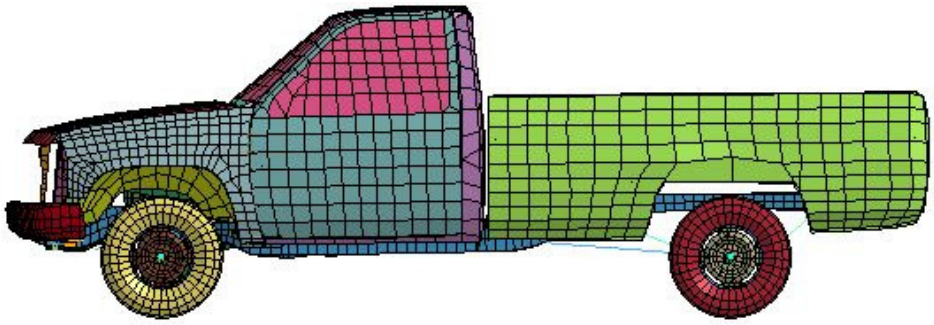

Figure 5.1. Finite element model of a Chevrolet C2500 pickup truck

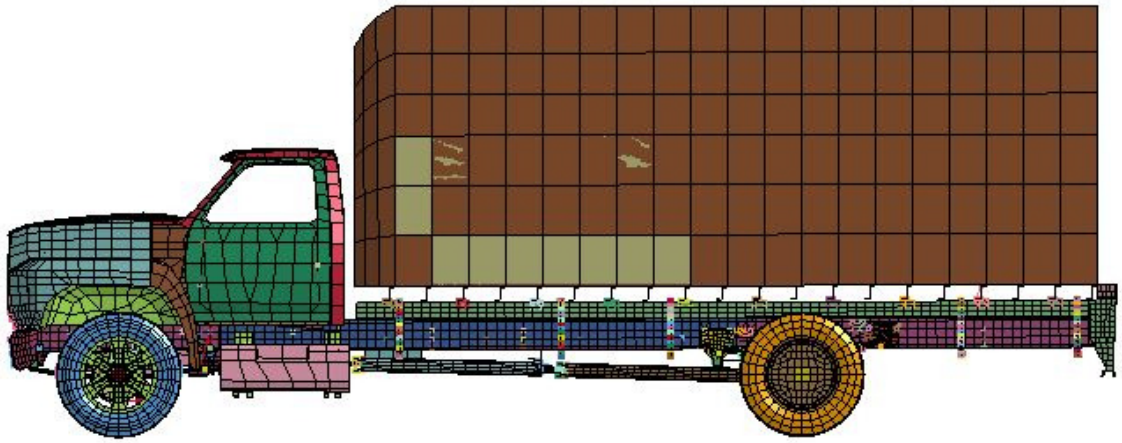

Figure 5.2. Finite element model of a Ford F800 single-unit truck

Figure 5.3. Finite element model of a tractor-trailer truck

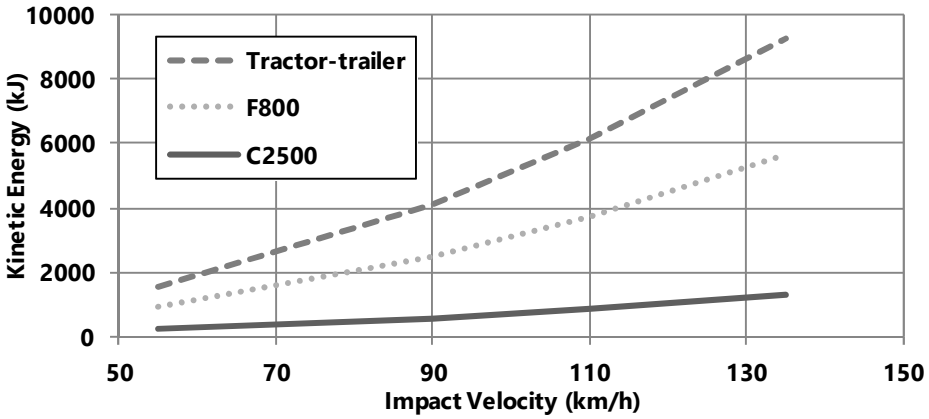

Figure 5.4. Kinetic energy versus impact velocity for the vehicle models

5.2. Vehicle Collision Validation

To verify the accuracy of the finite element model, it is necessary to validate the simulation responses with the results of available experimental tests. The C2500 and F800 vehicle models were validated by comparing impact forces reported by El-Tawil et al. (2005), Mohammed (2011), and Agrawal et al. (2013). The tractor-trailer vehicle model was validated by comparing impact forces and vehicle deformations with the full-scale vehicle impact test conducted by Buth et al. (2011). Another important aspect of assuring that the finite element models are behaving accurately, is to monitor the amount of hourglass energy introduced into the system and minimize it to an acceptable amount.

5.2.1. Pier Geometry

The C2500 and F800 vehicles models were validated by replicating the simulations conducted by El-Tawil et al. (2005). The validation exercise consisted of the vehicle models crashing into a circular reinforced concrete column at 55, 90, 110, and 135 km/h. The piers investigated consisted of circular reinforced concrete columns, 1,065 mm in diameter, 9,930 mm in height, and reinforced with fourteen No. 36 longitudinal bars and No. 16 transverse hoops spaced at 127 mm on center. The column rests on a pile cap 1,075 mm in depth and embedded 830 mm into the ground. The top of the column is loaded with a 32.5 Mg block to represent the mass of the supported superstructure. The cross-section and breakdown of the column used for validation is shown in Figure 5.5. The concrete has a compressive strength of 28 MPa and was modeled using material model 159. The steel reinforcement has a yield strength of 414 MPa and was modeled using material model 24. Because the impact forces were the only result of interest for validation, the base of the column was constrained and assumed fixed rather than

modeling the whole pile foundation. The hourglass energy was recorded for all simulations, and it was observed that very little hourglass energy was generated. Energy conservation was verified by assuring that hourglass energy in the system was less than 10% (Bala and Day 2004). Further verification checks were conducted to assure the accuracy of the models.

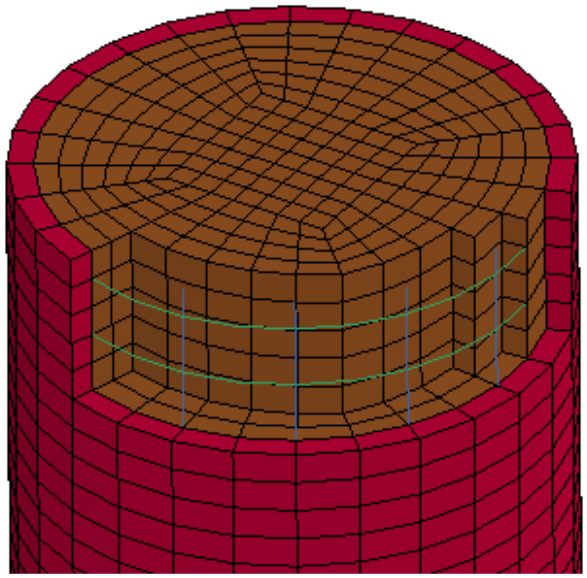

Figure 5.5. Cross-section and breakdown of column used by El-Tawil et al. (2005)

5.2.2. Boundary Conditions

The foundation of the column was constrained in the horizontal and vertical directions along the length of the section and over the entire base, respectively. A finite element study conducted by Sha and Hao (2013) showed that it is acceptable to use fixed boundary conditions at the base of an impacted column to predict the peak impact force to save on modeling and computational time. To obtain an accurate estimate of column displacement responses, the authors also suggest that it is necessary to use a detailed model of pile and soil spring interactions. For the purposes of this preliminary study, a fixed boundary condition has been used to validate vehicle-column impact responses. A detailed foundation is discussed further in the following section.

5.2.3. Initial Conditions and Loads

Vehicle impact simulations were conducted at four velocities: 55, 90, 110, and 135 km/h. The initial translational velocities were applied to the vehicles in the global x-direction using the initial velocity keyword.

Gravitational effects were applied to the system using dynamic relaxation to preload the model before conducting the transient analysis. Explicit dynamic relaxation is explained further later in this chapter.

5.2.4. Contact

Automatic surface-to-surface contact algorithms were utilized to model the interactions between the vehicles and the bridge piers. The master part, the vehicle model, transfers its energy and velocity to the slave part, the column, through the contact algorithms. From this interaction, it is possible to develop a time-history of the impact response due to the collision that can be used to compare results with experimental values and results published by other researchers. The static coefficient of friction and the dynamic coefficient of friction were set to a value of 0.30, based on a study conducted by El-Tawil (2005) to calibrate the coefficient of friction of the C2500 pickup truck colliding with a bridge pier.

5.2.5. Analysis Controls

The termination time for each simulation was determined based on the required amount of information that was desired. An analysis of 100 ms was sufficient to acquire peak impact forces, while a longer analysis would be required to observe the deformations in the columns.

Dynamic relaxation controls were used to determine the amount of iterations required to reach convergence when preloading the model under gravity loading. Explicit dynamic relaxation was activated and a termination time of 0.278 seconds was set to limit the time allowed for convergence to occur.

Hourglass energy was set to be computed and included in the energy balance. This allows for hourglass energy to be considered and observed when plotting the energy in the system throughout the analysis. The Flanagan-Belytschko stiffness form hourglass control with a coefficient of 0.05 was utilized to account for the nonphysical, zero-energy modes of deformation that produce zero strain and no stress, as discussed in the previous chapter. The hourglass coefficient value was assumed to be acceptable as this is the preferred method used by most users for automotive crash simulations (LSTC 2013).

5.2.6. Database Collection

The analysis results were recorded at time steps specified by the user. A time interval of 0.1 ms between each output was selected to obtain finely detailed results from the crash analysis. Data such as kinetic energy, hourglass energy, material energies in the model, and resultant impact forces between contacting parts were recorded.

5.2.7. C2500 Pickup Truck Model Validation

The easiest comparison to conduct is vehicle behavior upon impact. A comparison of the progression of the C2500 pickup truck impact at 110 km/h was conducted and is shown in Figure 5.6. The vehicle behavior is very similar between the two analyses with crumpling of the engine bay and passenger compartment. The resultant impact force time-history for the C2500 pickup truck at various impact velocities is shown in Figure 5.7. A comparison of the obtained peak impact forces with the published results for a

similar test procedure is shown in Figure 5.8. These results were in good agreement with those values reported by El-Tawil (2004) for low impact velocities, and the results fell between the values reported by El-Tawil and Mohammed (2011) for the higher impact velocities. The vehicle model simulations are believed to match well with published studies and will be used to draw conclusions for future work.

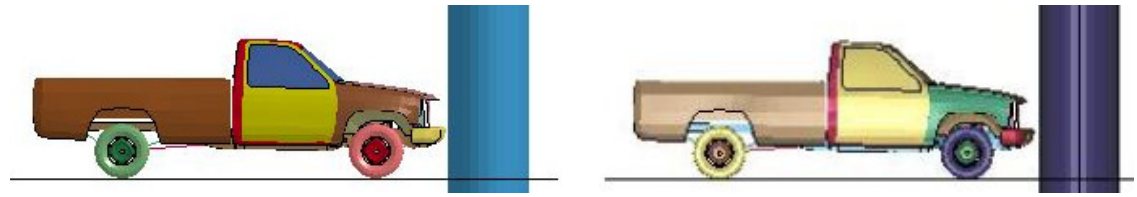

a) Time at 0.000 seconds

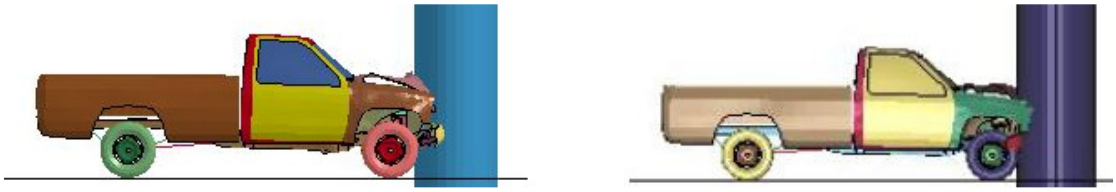

b) Time at 0.021 seconds

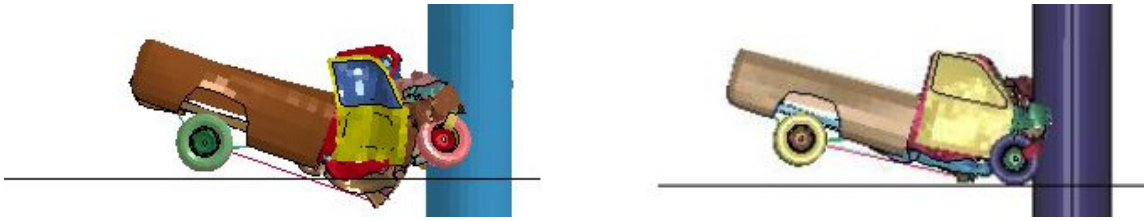

c) Time at 0.111 seconds

d) Time at 0.300 seconds.

Figure 5.6. Progression of impact of C2500 pickup truck at 110 km/h comparing simulation results (left) with El-Tawil (2004) results (right)

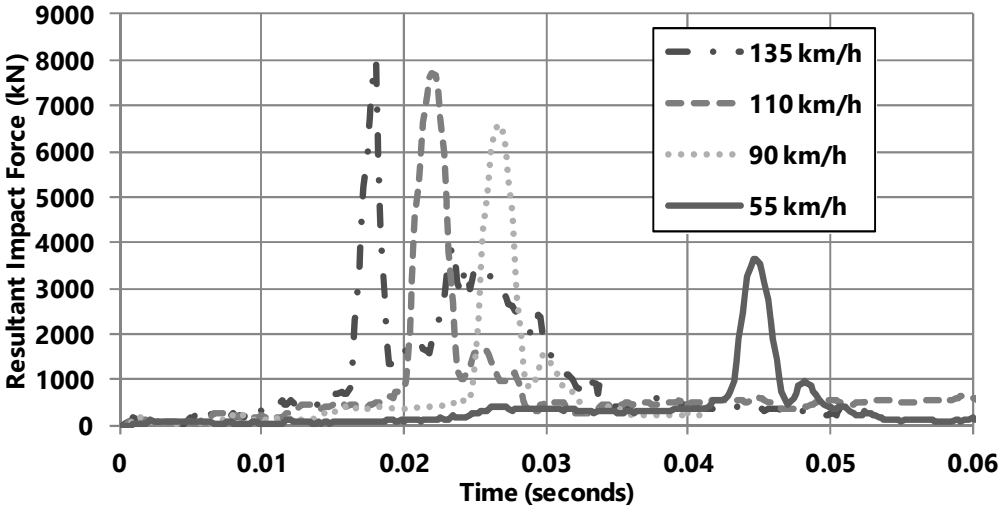

Figure 5.7. Resultant impact force data for the C2500 pickup truck at various impact velocities

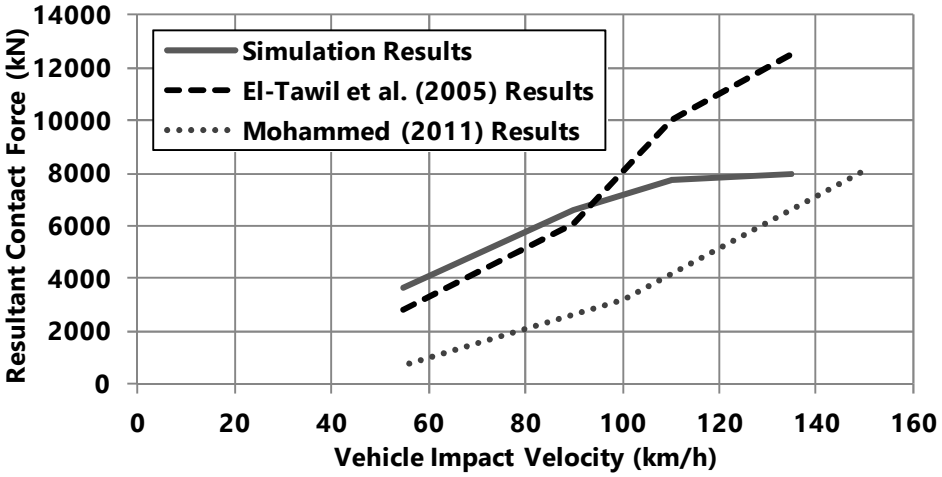

Figure 5.8. Comparison between the simulation results and the results published by El-Tawil et al. (2005) and Mohammed (2011)

5.2.8. F800 Single Unit Truck Model Validation

A comparison of the progression of the F800 single-unit truck impact at 110 km/h was conducted and is shown in Figure 5.9. The vehicle behavior is very similar between the two analyses with crumpling of the front of the vehicle and the rear wheels lifting off the ground. The resultant impact force time-history for the F800 single-unit truck at various impact velocities is shown in Figure 5.10. The peak impact forces from the simulations, shown in Figure 5.11, were compared to the peak impact forces published by

El-Tawil et al. (2005), Mohammed (2011), and Agrawal et al. (2013). The analytical peak impact forces fell within the range of reported values in the published literature and are therefore considered to be validated. The F800 single-unit truck simulations matched better than the C2500 pickup truck simulations and will most likely be used to conduct future work.

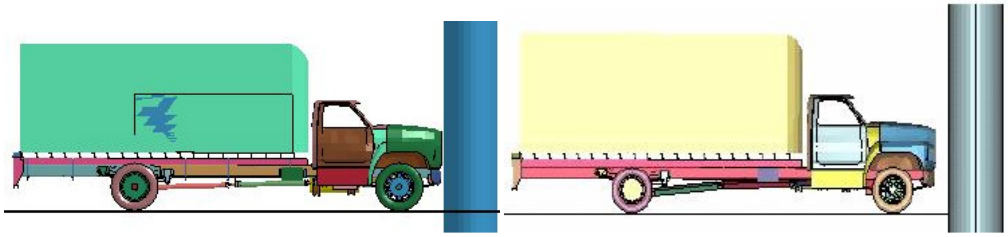

a) Time at 0.000 seconds

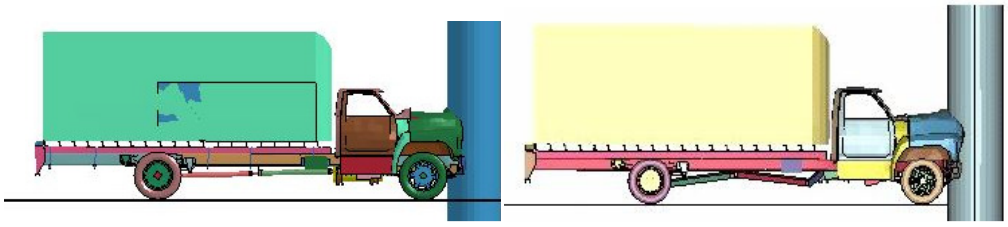

b) Time at 0.021 seconds

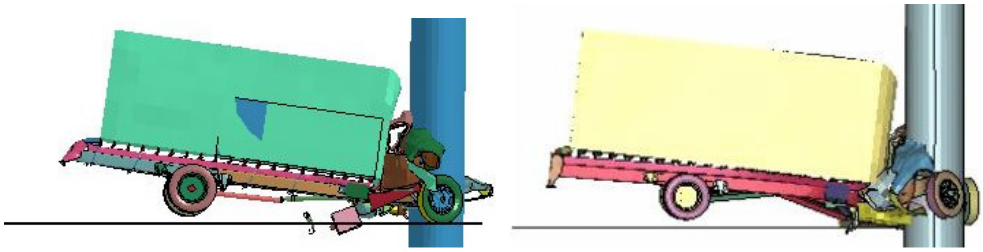

c) Time at 0.111 seconds

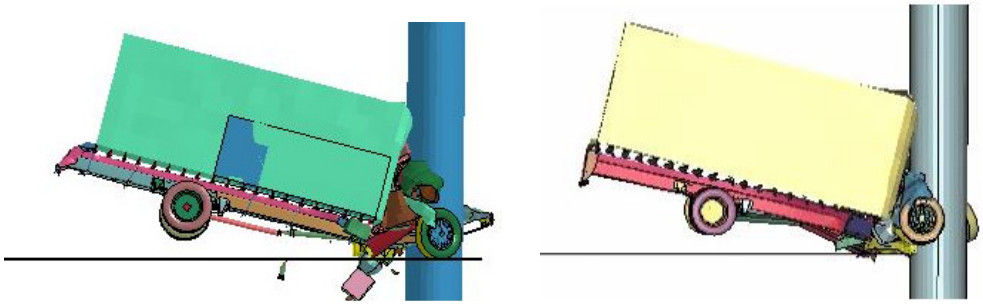

d) Time at 0.165 seconds

Figure 5.9. Progression of impact of F800 single-unit truck at 110 km/h comparing simulation results (left) with El-Tawil (2004) results (right)

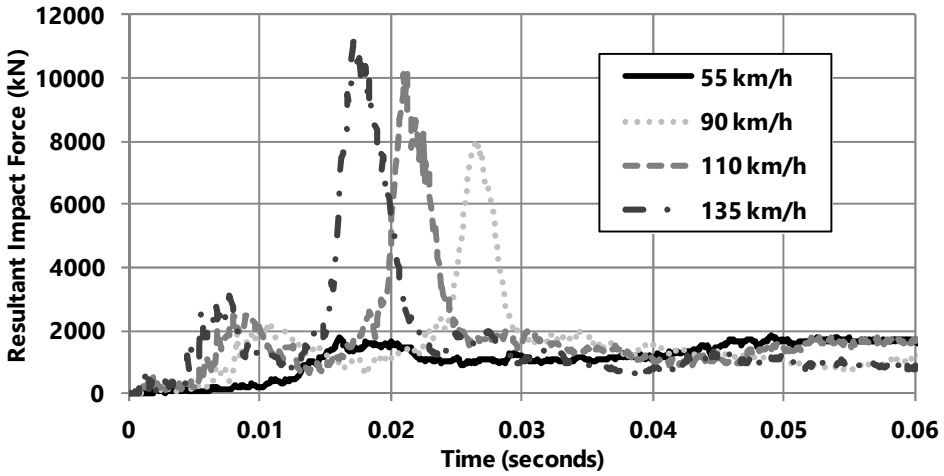

Figure 5.10. Resultant impact force data for the F800 single-unit truck at various impact velocities.

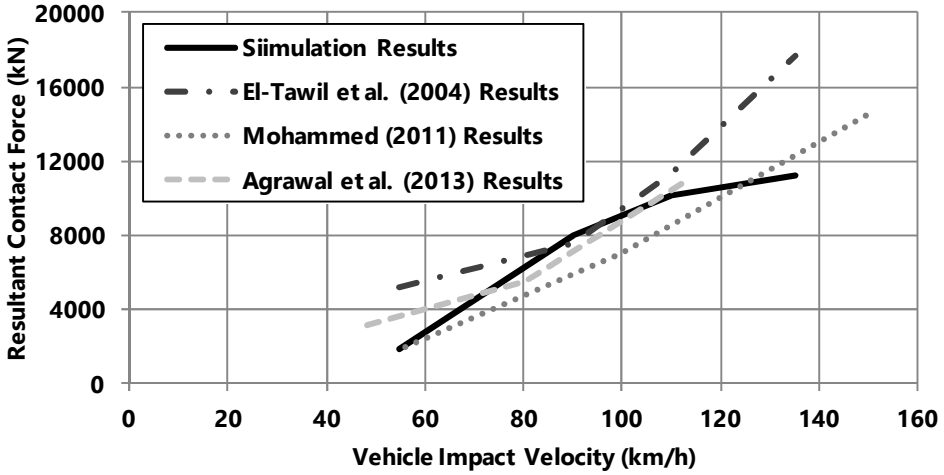

Figure 5.11. Comparison between the simulation results and the results published by El-Tawil et al. (2004), Mohammed (2011), and Agrawal et al.

5.2.9. Tractor-Trailer Vehicle Model Validation

The tractor-trailer vehicle model was validated by comparing the impact force of the numerical model with the results reported by Buth et al. (2011). The validation exercise consisted of the tractor-trailer crashing into a rigid steel column at 80.5 km/h. The simulation and experimental data of the resultant impact force time-history is shown in Figure 5.12. The peak impact force that occurred during the simulation was 10,600 kN, nearly two and half times larger than the reported experimental peak impact force of 4,240 kN. The obtained data was filtered with various moving averages, shown in Figure

5.13, to eliminate high spikes in short durations that can be considered noise in the data and not meaningful to the response of the structure. A moving average of 50 ms is commonly used to filter and analyze full-scale vehicle crash tests to establish design standards for impact forces (Buth et al. 2011). Caution must be used when applying a moving average with a time interval that is too long, because the impact forces can be reduced too much and forces the structure experiences will be inaccurate. Using a 50 ms moving average resulted in a peak dynamic impact force of 2,920 kN, just over the design impact force of 2,669 kN. Applying a 16 ms moving average reduced the peak impact force to around 4,940 kN and 3,160 kN for the analytical and experimental results, respectively. A 10 ms moving average resulted in a peak impact force around 6,500 kN and better represented the shape of the impact response, compared to the 16 ms moving average. The time of the peak impact force in the numerical analysis occurred at around the same time, 0.032 seconds, as the experimental peak impact force. The behavior of the impact force over the duration of the impact is comparable to the impact force time-history recorded during the experiment. The hourglass energy was observed to account for less than 10% of the total energy in the system; verifying the proper use of hourglass energy control. Overall the numerical analysis matches well with the experimental results.

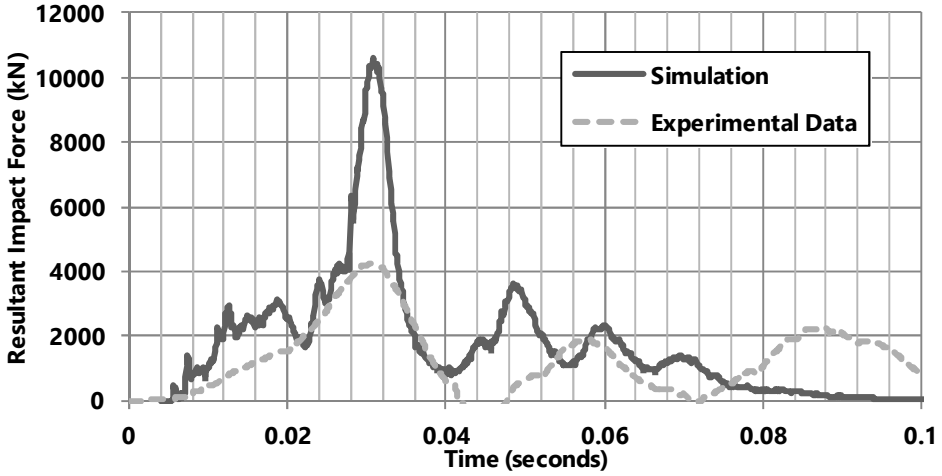

Figure 5.12. Simulation and experimental data of the resultant impact force versus time for the tractor-trailer collision with a rigid pier

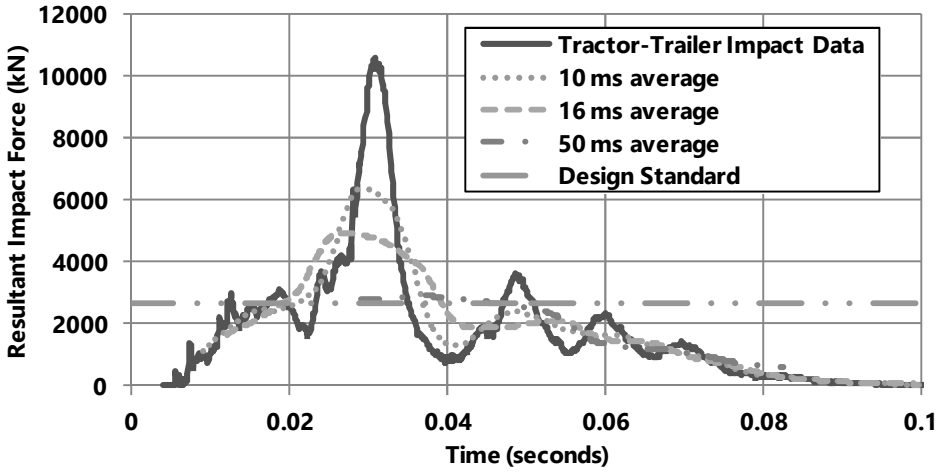

Figure 5.13. Filtered data for tractor-trailer impact

5.2.10. Failure Modes

Bridge piers subjected to vehicle impact forces are typically found to have large shear and bending forces. Shear failure is the major mode of failure typically observed in the field where the shear force generated by the impact exceeds the shear capacity of the pier (Buth et al. 2010). The design specifications calculate the nominal shear capacity of the column based on two 45^{o} shear failure planes radiating out from the location of the impact force, as shown in Figure 5.14. This type of failure mode was observed in the C2500 and F800 impact simulations, as shown in Figure 5.15. The fringe levels display

the plastic strain contours throughout the system, where the color red represent cracking of the concrete. Figure 5.16 shows the fringe levels of the cross-section of the column during the impact of the F800 truck. Cracking of the unconfined concrete cover and portions of the core were observed. The failure modes of the column in the finite element model appear to be consistent with the observed failure modes of actually impacted columns.

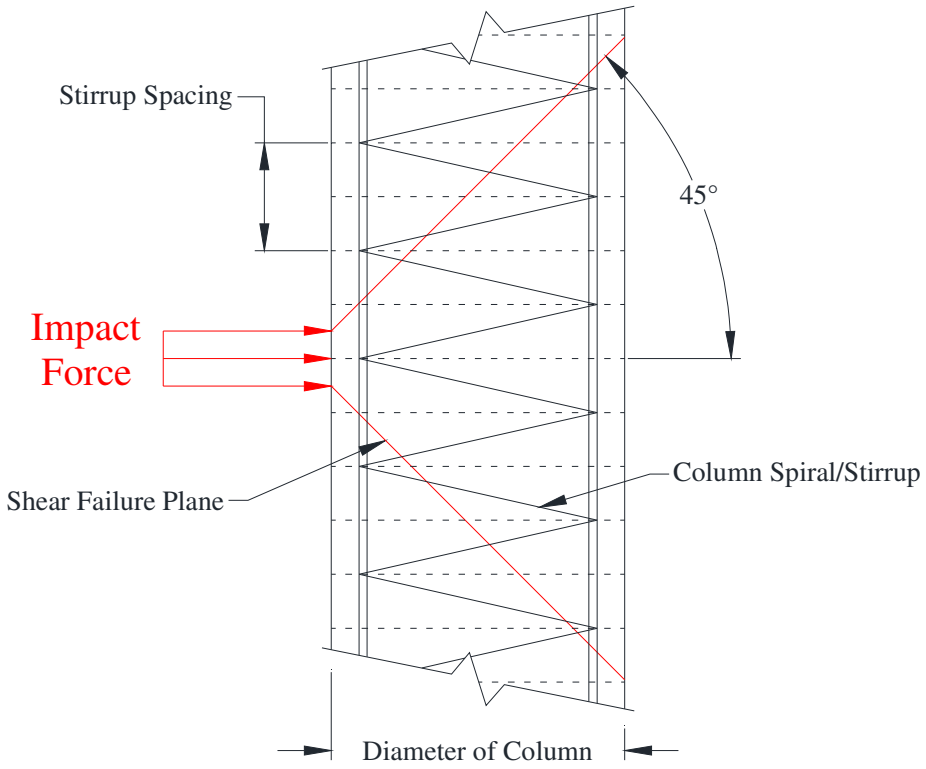

Figure 5.14. Shear failure mechanism due to vehicle impact force (Buth et al. 2010)

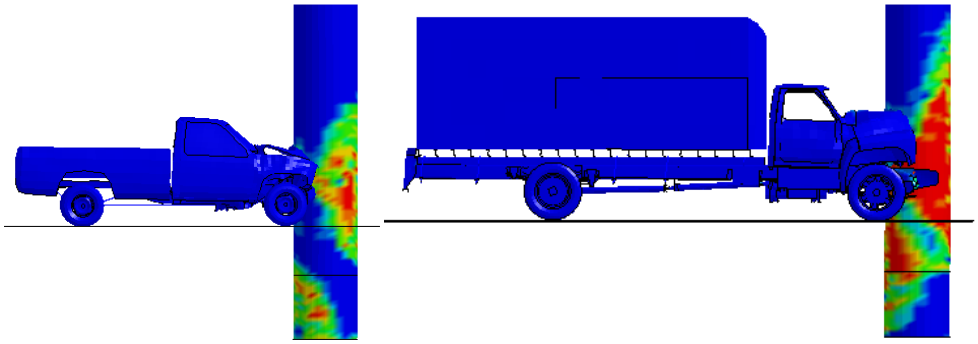

Figure 5.15. Plastic strain contours for the C2500 pickup (left) and F800 SUT (right) resulting from an impact at 110 km/h

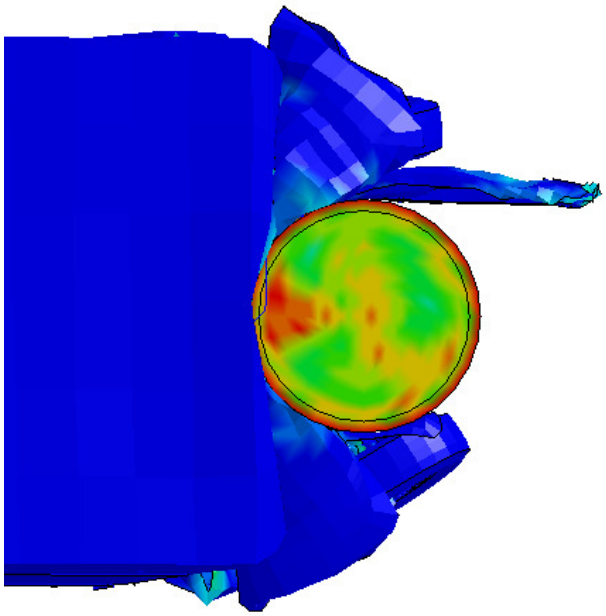

Figure 5.16. Plastic strain of the cross-sectional area of the column subjected to the F800 single unit truck at 110 km/h

5.3. Explicit Dynamic Relaxation

Explicit dynamic relaxation is a transient analysis used to preload a model to a steady-state that precedes a regular transient analysis. Preloading is an important way of inducing gravity loads prior to conducting an analysis.

Explicit dynamic relaxation was invoked by defining a curve to be used for stress initialization by dynamic relaxation (SIDR) parameter. The curve ramps the acceleration due to gravity from 0 to 9.806 m/s^2 and then holds it constant until dynamic relaxation convergence is achieved. This allows for the acceleration due to gravity to be gradually applied to the system and not cause excessive oscillation of the elements and their nodes. Another curve is defined to be used during transient analysis only. This curve has an identical horizontal acceleration as the previous curve to continue to apply gravity throughout the transient analysis. The two curves used in the analysis are shown in Figure 5.17. A scale factor of 9.806 m/s^2 was applied to each load curve.

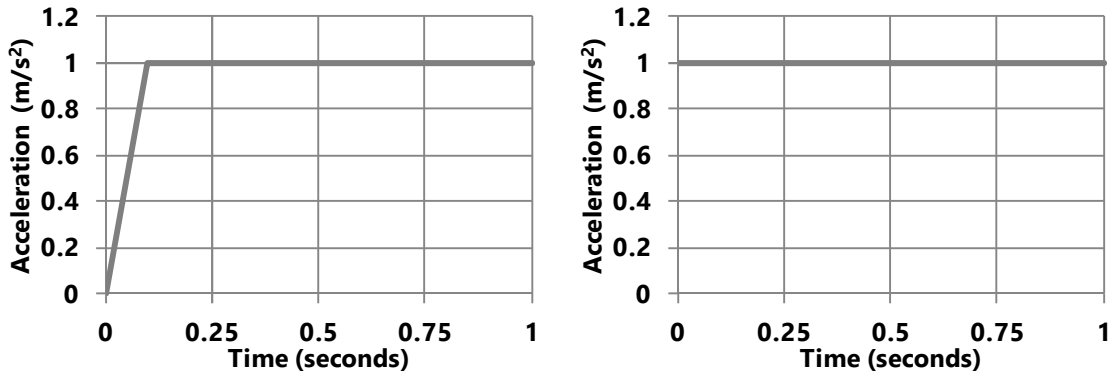

Figure 5.17. The stress initialization by dynamic relaxation (left) and transient analysis (right) load curves for acceleration due to gravity

A study was conducted to determine how long it took to preload the bridge pier with gravity and what effect it had on the response of the structure due to the impact of a rigid plate. For this study a plate with dimensions of 2000 mm width, 2000 mm height, and 100 mm thick was constructed and made rigid using material model 20. The masses of the rigid plates were specified to be 1.84, 8.06, and 13.15 Mg; corresponding to the masses of the three trucks used in the simulations. Simulations were conducted with and without dynamic relaxation invoked. Dynamic relaxation convergence of the column under gravity load was reached at 0.278 seconds. In all instances, dynamic relaxation had almost no effect on the impact response, as shown in Figure 5.18. The horizontal displacement of a single node was monitored to identify a difference between applying and not applying dynamic relaxation in an analysis. The displacement time-history for the three impact events is shown in Figures 5.19-5.21. It was observed that nodal displacements were reduced when dynamic relaxation was utilized. This study suggests that preloading a model before conducting a transient analysis should be done to obtain more realistic results, and a termination time of approximately 0.3 seconds can be applied to the dynamic relaxation controls in order to effectively preload the column in the vehicle collision simulations for the model used to conduct this study.

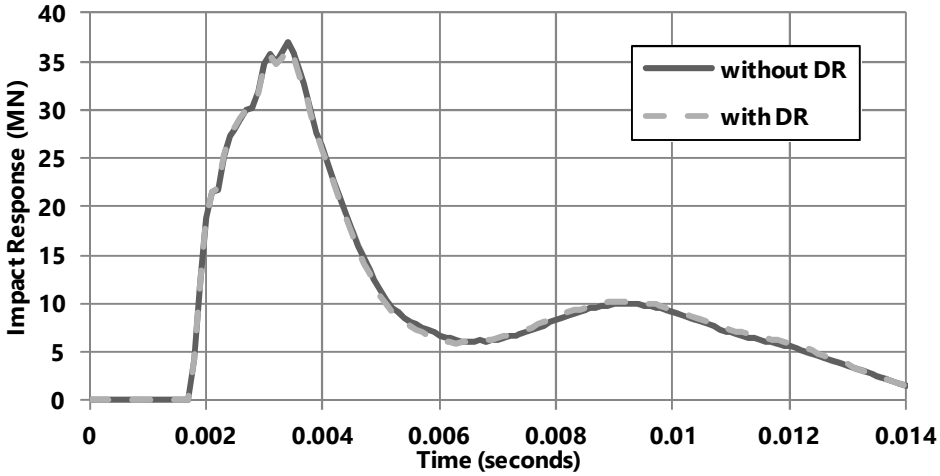

Figure 5.18. Impact response of 13.15 Mg rigid plate with column at 32 km/h

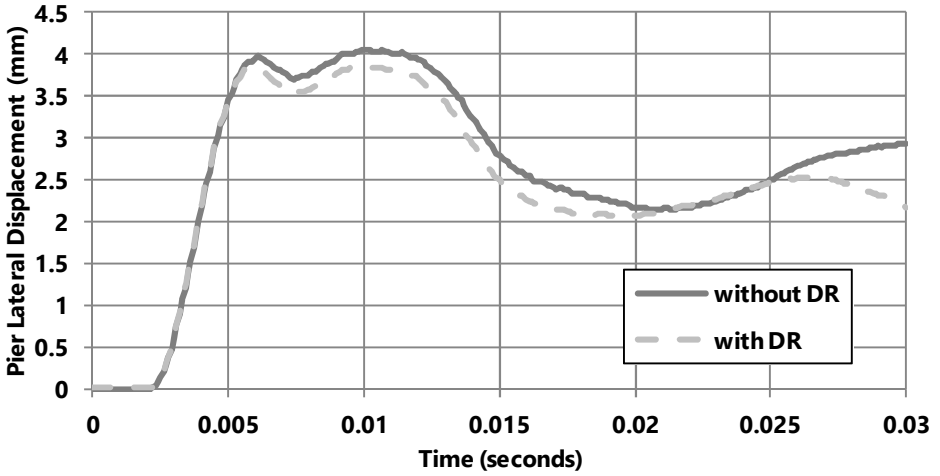

Figure 5.19. Displacement versus time for 1.84 Mg rigid plate impact simulation with and without dynamic relaxation

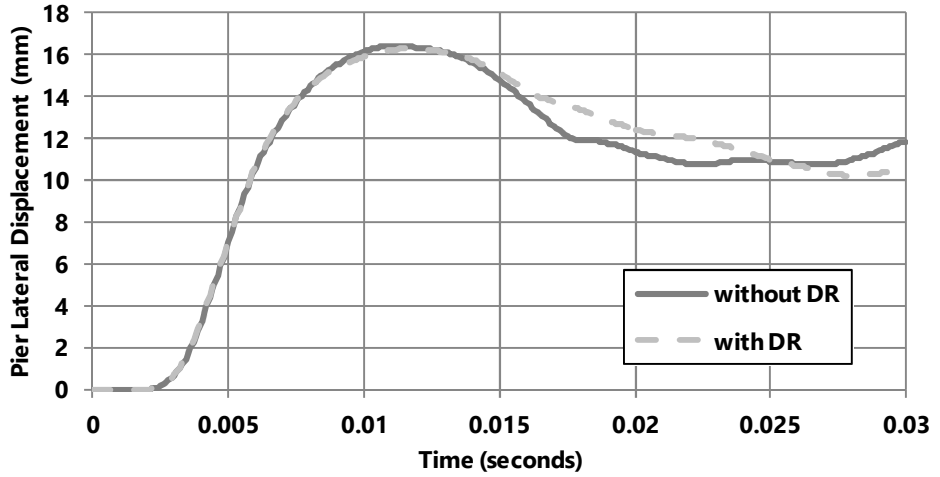

Figure 5.20. Displacement versus time for 8.06 Mg rigid plate impact simulation with and without dynamic relaxation

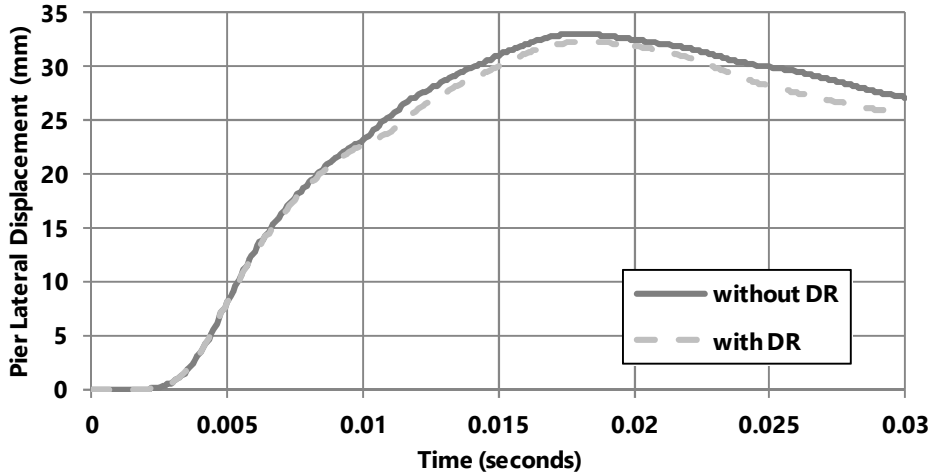

Figure 5.21. Displacement versus time for 13.15 Mg rigid plate impact simulation with and without dynamic relaxation

By validating these vehicle models, it was concluded that the finite element procedures used in these simulations can be applied to develop vehicle impact simulations with bridge piers. The vehicle damage and peak impact forces for the Chevrolet C2500 pickup truck and the Ford F800 single unit truck models are consistent with those values reported by other researchers. The simulation data of the tractor-trailer can be filtered using a moving average to match the design vehicle collision force specified by AASHTO. A 10 ms moving average window was found to sufficiently smooth out the minor peaks while still following the general curve of the impact response. The results from the F800 single unit truck matched the best with the results reported by the other researchers and were considered for use with further research. It was observed that dynamic relaxation is necessary to obtain accurate impact forces and lateral displacements of the impacted pier.

CHAPTER 6.

SENSITIVITY ANALYSIS OF PIER PARAMETERS

To evaluate the impact of different parameters, such as pier diameter, transverse hoop spacing, and vehicle impact velocity, a sensitivity analysis has been conducted. Two studies were conducted to observe the effect of pile cap height and modeling the pier as part of a multi-pier bent configuration. This section includes a thorough review of AASHTO LRFD specifications for designing bridge piers, the process taken to develop the vehicle collision models for LS-DYNA analysis, and a summary of the impact results. The purpose of this research was to observe different failure modes that could possibly occur when bridge piers were subjected to vehicular collisions. Therefore, not all of the piers in the following parametric study possess adequate shear resistance for vehicular collision loads.

6.1. AASHTO LRFD Bridge Pier Design Specifications

An extensive review of the AASHTO design specifications was conducted in order to create bridge piers that possessed realistic values for material properties, dimensions, and strength capacities. The following provisions were taken into account and used to construct a bridge pier for this parametric study.

6.1.1. Material Unit Weights

The unit weight for various construction materials were specified as follows: 22.78 kN/m^3 (2,325 kg/m^3) for normal weight concrete with a compressive strength of 35 MPa or less, 76.98 kN/m^3 (7,850 kg/m^3) for structural steel components, 18.85 kN/m^3 (1,922 kg/m^3) for compacted sand, silt, or clay, and 15.71 kN/m^3 (1,602 kg/m^3) for loose

sand, silt, or clay (AASHTO, 2012). The minimum concrete strength to be used in bridge components is 16.5 MPa.

6.1.2. Concrete

Five classes of concrete are specified that correspond to the different types of concrete to be used in various structural components and are outlined in Table C5.4.2.1-1 (AASHTO 2012). Class A concrete was selected as the primary class of concrete for the following parametric study. Class A concrete possesses the following material properties: minimum cement content of 362 kg/m^3, maximum water to cement ratio of 0.49, coarse aggregate size of 4.75 to 25 mm, and a 28-day compressive strength of 28 MPa (AASHTO 2012). The modulus of elasticity, E_c, was calculated with the following equation:

$$E_c = 0.043 K_1 w_c^{1.5} \sqrt{f'_c} \qquad \text{Equation 0-1}$$

where K_1 is a correction factor for the source of aggregate and is taken as 1.0, w_c is the unit weight of concrete (Mg/mm^3), and f'_c is the specified compressive strength of the concrete (MPa). The modulus of elasticity for the concrete used was 25.35 GPa. The Poisson's ratio is assumed to be 0.2. The modulus of rupture, f_r, was estimated using the following equation:

$$f_r = 0.63 \sqrt{f'_c} \qquad \text{Equation 0-2}$$

where f'_c is in MPa. The modulus of rupture for the concrete was calculated to be 3.34 MPa.

Table 5.12.3-1 in the AASHTO LRFD outlines the various cover depths that are specified for unprotected steel reinforcement (AASHTO 2012). A 25 mm minimum cover depth should be provided for main reinforcement that is protected by an epoxy

coating. It was assumed that the bridge piers to be modeled would be exposed to deicing salts and therefore requires a concrete cover depth of 65 mm be provided to protect the steel reinforcement cage from corrosion (AASHTO 2012).

6.1.3. Reinforcing Steel

The steel bars used for reinforcement should have nominal yield strength of 420-520 MPa. The nominal yield strength of 420 MPa was selected for the reinforcement for the parametric study. The modulus of elasticity was considered to be 200 GPa.

Circular reinforced concrete columns must have a minimum of six No. 16 longitudinal bars in circular arrangement. The area of longitudinal reinforcement must be between 0.01 to 0.04 times the gross cross sectional area of the column according to Section 5.10.11.4.1a (AASHTO, 2012). The size of the transverse reinforcement bars is based on the selected size for longitudinal bars. No. 10 bars are used for transverse reinforcement when No. 32 bars, or smaller, are used for longitudinal reinforcement; otherwise No. 13 bars are used for transverse reinforcement. The maximum spacing of transverse reinforcement in compression members should not exceed the pier diameter or 300 mm, as specified in Section 5.10.6 (AASHTO 2012).

6.2. Bridge Pier Models

The models developed for this sensitivity analysis consist of three major components: the bridge pier, foundation, and vehicle. An example of a layout view of the entire model is shown in Figure 6.1. The AASHTO design specifications were used to design the piers for the sensitivity analysis study. The bridge piers consisted of circular reinforced concrete columns with 5 m in height above the ground surface. Resting atop the piers were a 1 m tall cylindrical mass of 250 metric tons representing the mass of a

superstructure proportional to the tributary area supported by the pier. Three pier diameters of 600, 900, and 1,200 mm were investigated for the purposes of this parametric study. The piers were reinforced with 6, 12, and 24 No. 25 longitudinal bars, respectively, to provide a 1% longitudinal reinforcement ratio. The piers were reinforced transversely with No. 10 hoop bars spaced at 50, 150, and 300 mm to capture the effect of transverse reinforcement on the shear capacity of the piers. The considered hoop spacing followed the requirements of AASHTO for concrete compression members. A concrete cover of 65 mm was provided for all the piers. An example of the layout for the pier cross sections is shown in Figure 6.2. The concrete has a compressive strength of 28 MPa, maximum aggregate size of 24 mm, and a mass density of 2,325 kg/m^3. The steel reinforcement was assumed to have a yield strength of 420 MPa, modulus of elasticity of 200 GPa, tangent modulus of 1,500 MPa, and a mass density of 7,850 kg/m^3. Rate effects on yield stress for the steel reinforcement were modeled using the dynamic increase factor formulas established by Malvar and Crawford (1998). The piers were supported by a deep pipe pile foundation, discussed further later in this chapter. The pipe piles have a yield strength of 250 MPa, modulus of elasticity of 200 GPa, tangent modulus of 1,500 MPa, and a mass density of 7,850 kg/m^3. A 50 mm thick elastic material layer was applied atop of the pile cap to represent the weight of the 1 m deep soil layer that is supported by the foundation The impact velocity of the vehicle is set to 55, 80, and 120 km/h.

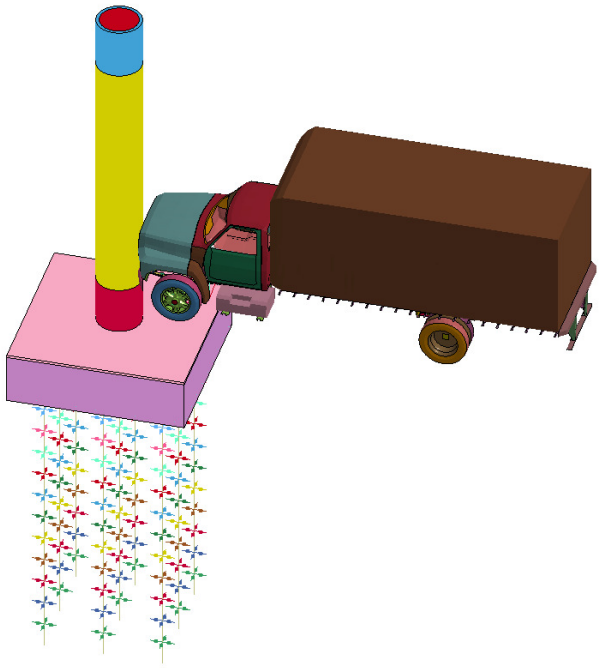

Figure 6.1. Complete model for vehicle collision with a bridge pier

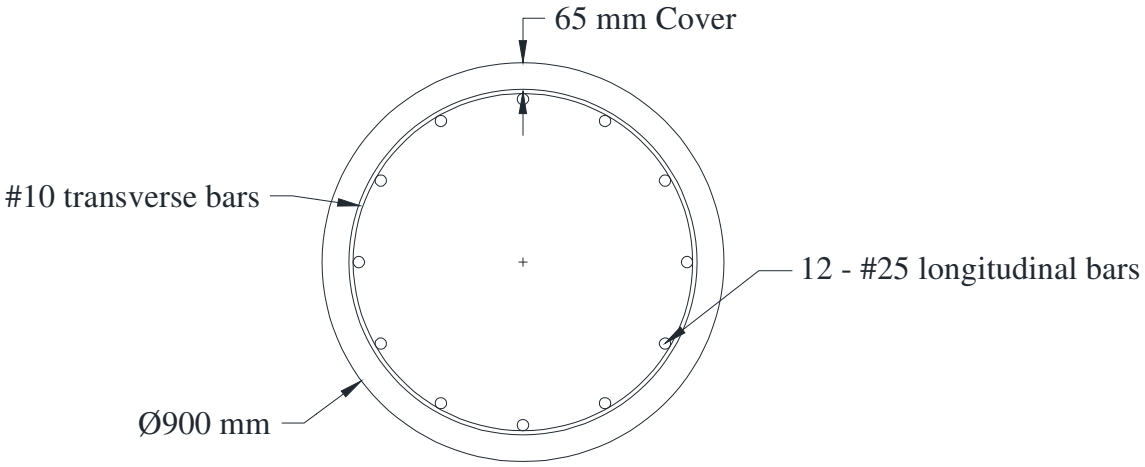

Figure 6.2. Cross sectional layout of 900 mm diameter bridge pier

6.2.1. Deep Pile Foundation

The soil supporting the bridge piers is very dense sand with a unit weight of 21.0 kN/m^3 (21.43 kg/m^3), internal friction angle of 40°, and allowable soil pressure of 250 kPa. A deep pile foundation was utilized to support the bridge piers. The foundation consisted of a pile cap with nine PP360×11.12 pipe piles. The tops of the pile caps are placed 1 m below the assumed ground surface. The pile caps are designed as square mat

foundations following ACI specifications (Coduto 2001). The pile caps for the 600 and 900 mm diameter piers have dimensions of 3.5 m wide, 3.5 m long, and 1 m deep. The pile cap for the 1,200 mm diameter pier have dimensions of 3.6 m wide, 3.6 m long, and 1 m deep. The pile caps are reinforced with 9 No. 13 bars in the X and Y axes. The pile cap element mesh and reinforcement is shown in Figure 6.3. A pinned connection at the base of the pipe piles has been considered.

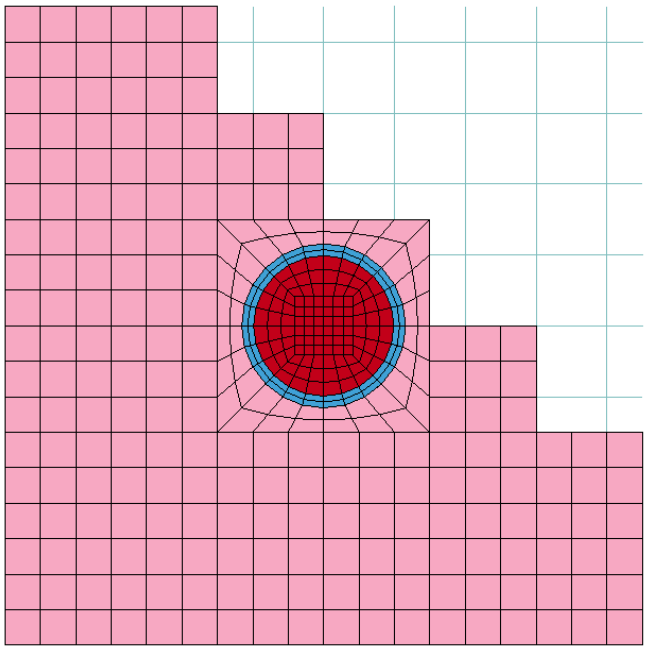

Figure 6.3. Mesh used to connect pier to pile cap with pile cap reinforcement shown

To effectively capture the interaction that occurs between the deep pile foundation and the surrounding soil, the American Petroleum Institute (API) method of determining load-displacement curves for laterally loaded sand was used (API, 2005). The load-displacement curves represent the stiffness of the surrounding soil at various depths along the length of the piles and were modeled using inelastic springs. Springs were placed every 500 mm along the length of the piles in the X and Y axes (along the horizontal plane). The springs were set to only act in compression, as soil has no tensile stiffness. The springs were created with 250 mm long discrete elements and the stiffness properties

were modeled using the inelastic spring model in LS-DYNA. The springs at similar depths were all assigned the same material and sections properties.

The dense sand surrounding the foundation was assumed to have an effective soil weight of 21 kN/m^3 and an angle of internal friction of 40°. The pipe piles had a diameter of 360 mm and a length of 6000 mm. At a given depth, the ultimate lateral bearing capacity for sand was determined as the smallest value given by Equation 0-3 for shallow depths and Equation 0-4 for deep depths:

$$p_{us} = (C_1 H + C_2 D)\gamma H \quad \text{Equation 0-3}$$

$$p_{ud} = C_3 D \gamma H \quad \text{Equation 0-4}$$

where p_u is the ultimate lateral bearing capacity (kN/m) (s = shallow, d = deep), γ is the effective soil weight (kN/m^3), H is the soil spring depth (m), the C_1, C_2, and C_3 coefficients are determined from Figure 6.8.6-1 of API (2005) as a function of the internal friction angle, φ', and the average pile diameter, D, from surface to depth (m), and were defined as 4.6, 4.25, and 100, respectively. For each soil spring spaced at 500 mm along the length of the piles, a $p - y$ curve was defined describing the lateral soil resistance at each depth versus the lateral displacement of the foundation. These $p - y$ curves for sand are nonlinear and were approximated using Equation 0-5:

$$P = A p_u \tanh\left[\frac{kH}{A p_u} y\right] \quad \text{Equation 0-5}$$

where A is the factor to account for cyclic or static loading condition, p_u is the ultimate bearing capacity at depth H (kN/m), and k is the initial modulus of subgrade reaction (kN/m^3). Determined as a function of angle of internal friction, φ', using Figure 6.8.7-1 of API (2005), y is the lateral deflection (m), and H is the soil spring depth (m).

Equation 0-5 was used to determine the resistive force per length of foundation to laterally displace the pile. The curves were multiplied by the tributary length of the springs, 500 mm, to give the spring stiffness $p - y$ curves for various depths, shown in Figure 6.4.

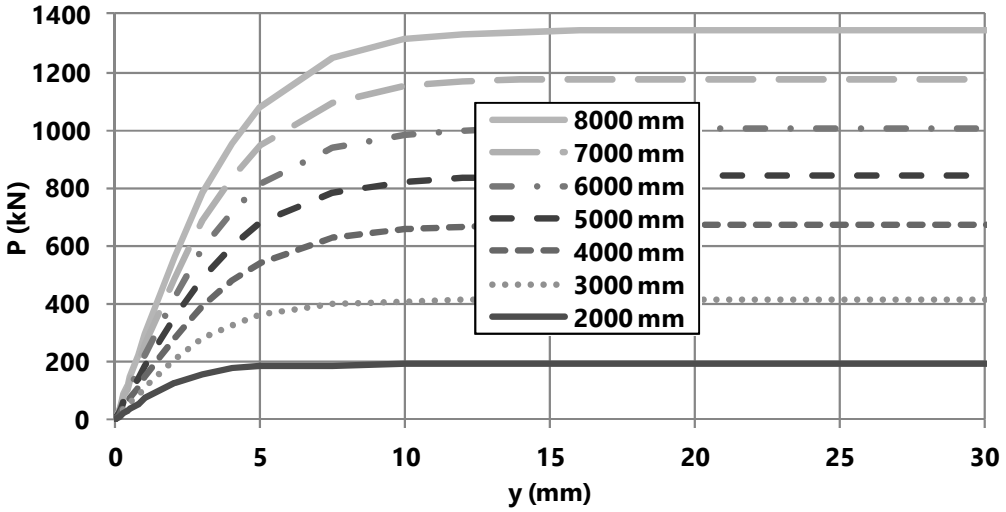

Figure 6.4. Example of the spring stiffness p-y curves used for the soil springs

6.2.2. Stress Initialization Through Dynamic Relaxation

Bridge piers carry a huge load due to the mass that is imposed by the hefty superstructure they support. A bridge pier exposed to gravity will not have the same compressive strength of an unstressed bridge pier. Hence, it becomes necessary to develop a model of a bridge pier that is loaded under gravity before a vehicle impact simulation can be performed. As the pier is loaded axially, the concrete material expands slightly in the transverse direction due to Poisson's effect. The tensile strength of the steel reinforcing bars helps to confine and reduce the expansion of the concrete core, increasing the compressive strength of the concrete slightly. This confining effect plays a large part in the response of structures under impact loads. The transverse reinforcement in a compression member is provided for shear strength but also helps to confine the concrete core under axial loading.

LS-DYNA utilizes three methods to develop an initially stressed state of equilibrium: quasi-static transient analysis with mass damping, explicit dynamic relaxation, and implicit dynamic relaxation. Dynamic relaxation is an analysis used to preload a system prior to the start of the regular transient analysis phase. Preloading stresses and displacements are typically very small. Dynamic relaxation effectively dampens the system to reduce computed nodal velocities until the distorted kinetic energy is reduced to a convergence limit. When the convergence limit is reached, or a termination time is met, the dynamic relaxation phase terminates and the transient analysis phase begins.

All stress initialization methods in LS-DYNA involve ramping up gravity slowly over time. This prevents the dynamic oscillation of elements that can occur under instantaneous acceleration. Stress initialization due to quasi-static transient analysis with mass damping involves applying a gravity curve that ramps up and then holds steady during the regular transient analysis. Then mass damping is applied to reduce dynamic oscillation of the elements until preloading is established. The mass damping is reduced to zero once the preloaded state is established. The rest of the analysis follows once the preloaded state is accomplished. This method is simple to apply and perform but cannot be used in problems where initial velocities are used, therefore this method was ruled out for vehicle impact studies.

When using dynamic relaxation, two acceleration curves are required: a ramped gravity curve that holds constant when the acceleration due to gravity is reached, which is used during stress initialization, and a constant gravity curve that is used during the proceeding transient analysis. Explicit dynamic relaxation uses the known displacements,

velocities, and accelerations of the nodes to solve directly for nodal displacements at future time steps. This method of preloading was mentioned earlier in Section 5.3. Implicit dynamic relaxation uses the unknown values for nodal velocities and accelerations to solve for nodal displacements at future time steps. Implicit dynamic relaxation is iterative but is the ideal method for stress initialization because the displacement and stresses are very small. While conducting this research, both methods were attempted, and implicit dynamic relaxation was found to be significantly faster and more computationally efficient at preloading the bridge piers. It should be noted that the vehicle models that are available have already been preloaded, so they should not be included during dynamic relaxation.

The implicit analysis will run until a specified termination time is reached (0.8 ms in the current study). A time step size of 0.2 ms was used for implicit analysis. After the dynamic relaxation analysis, the element stresses and nodal displacements are recorded in a separate file. The contents of this file were then used to create a pre-stressed pier model that could be used in combination with the already preloaded vehicle model.

6.2.3. Vehicle Model

The impacting vehicle used during this parametric study was the 1997 Ford F800 single unit truck (SUT) model. The F800 truck has a mass of 8,063.4 kg, and it falls under the category of Class 5 trucks with a gross vehicle weight rating of 7,258 – 8,845 kg, representing medium weight trucks. The impact velocity of the truck was investigated at 55, 80, and 120 km/h. The vehicle was placed with its bumper roughly 120 mm away from the pier. The engine compartment of the F800 SUT impacts the pier between 0.5 and 1.7 m above the surface of the ground. The only change made to the F800 SUT

model was to the initial velocity. It should be noted that the vehicle model used during this study was approximately one third the weight of the vehicle used to determine the 2,669 kN vehicle collision force specified in the design provisions.

6.2.4. Model Input Parameters for Transient Analysis

The following input parameters were used during the vehicle impact analyses. Any of the cards used to initiate dynamic relaxation or collect data for stress initialization were no longer needed at this phase in the modeling process.

Various parameters were used to control the transient analysis. The hourglass energy was computed and included in the energy balance. This assures that hourglassing is accounted for and recorded during the impact analysis. Flanagan-Belytschko stiffness hourglass control was used to control hourglassing in the system. An hourglass coefficient of 0.05 was considered.

An automatic surface-to-surface contact algorithm was used to allow for the contact between the bridge pier and the vehicle. All parts of the vehicle were assigned as the master part set. All parts of the pier were assigned as the slave part set. The static and dynamic coefficients of friction were set to represent the coefficient of friction between concrete and steel (El-Tawil 2004).

The displacements, shear forces, and moments at various heights along the length of the pier were recorded. Node and solid sets were used to identify the piers cross sections every 500 mm along the length of the pier to obtain such results. The resultant impact forces that occurred between the vehicle and pier elements were also captured. Time histories of the kinetic, internal, total, and hourglass energy during the simulation were recorded.

6.2.5. Model Summary

A total number of 75,952 nodes and 69,373 elements made up the vehicle and pier models. The pier models, including the foundation and soil springs, consisted of 37,003 nodes and 34,020 elements. There were 2,664 beam elements, 30,960 solid elements, and 396 discrete elements in the pier models. The height of the elements along the Z axis was set to 50 mm. The mesh size of the elements in the pier ranged from 30 to 75 mm due to the unique construction of the circular cross section of the pier, shown in Figure 6.3. The same mesh was used for the three different diameter piers. Connectivity between different parts of the model was assured by merging the nodes at the same locations.

6.3. Vehicle Impact Results

6.3.1. Visual Response Due to Vehicle Collision

A total of twenty seven analyses were conducted; three pier diameters with three different hoop spacing at three vehicle impact velocities. The results are divided by pier diameter to observe the failure mechanisms, if any, which occurred due to vehicle impact at a time of 100 ms.

The following results show the effects of hoop spacing and concrete confinement. Using the method developed by Mander et al. (1988), the confined concrete strength for the various bridge piers with various hoop spacing was updated, presented in Table 0-1. It can be observed that at the maximum hoop spacing of 300 mm, there is minimal increase to the concrete strength due to confinement. As the hoop spacing decreases to 50 mm, the strength of the confined concrete increases between 25% and 50%. The confinement of the core concrete plays a huge role in the pier's ability to effectively resist collision forces, which can be observed in the following impact results. Smaller hoop spacing

provides higher confined concrete strength in the core and increases shear capacity of the pier.

Table 0-1. Confined concrete strength (MPa) for various piers and hoop spacing

Hoop Spacing	Pier Diameter		
	600 mm	900 mm	1200 mm
300 mm	29.4	29.2	29.0
150 mm	32.1	30.9	30.2
50 mm	41.7	37.2	34.9

The 600 mm pier had the least amount of structural stiffness of the piers in this study. As a result a significant amount of failure was observed in these piers. The results occurring in the 600 mm pier with hoop spacing of 300, 150, and 50 mm are shown in Figure 6.5. It can be observed that as vehicle impact velocity increases, the amount of damage done to the pier also increases. This is a correct observation because as the vehicle's velocity increases from 55 to 120 km/h the amount of kinetic energy the vehicle possess increases quadratically, which will then be transferred to the pier after the crash. The effect of the pier concrete confinement due to the hoop spacing can be observed at the various impact velocities. As the hoop spacing increases, the confined strength of the concrete core decreases, the shear capacity decreases, and the amount of damage increases at the location where the pier connects to the pile cap.

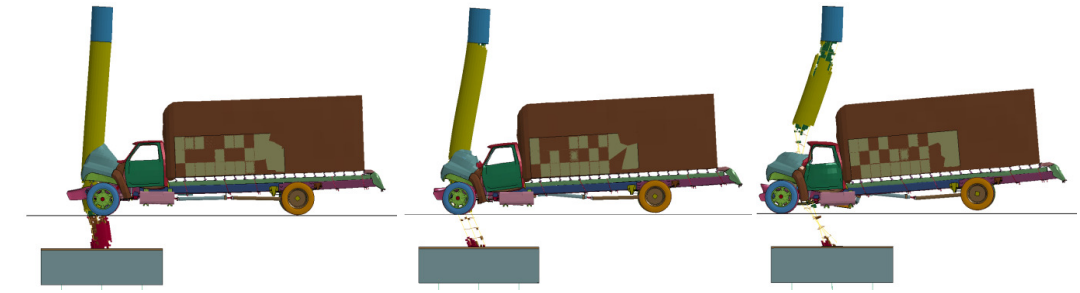

a)300 mm hoop spacing

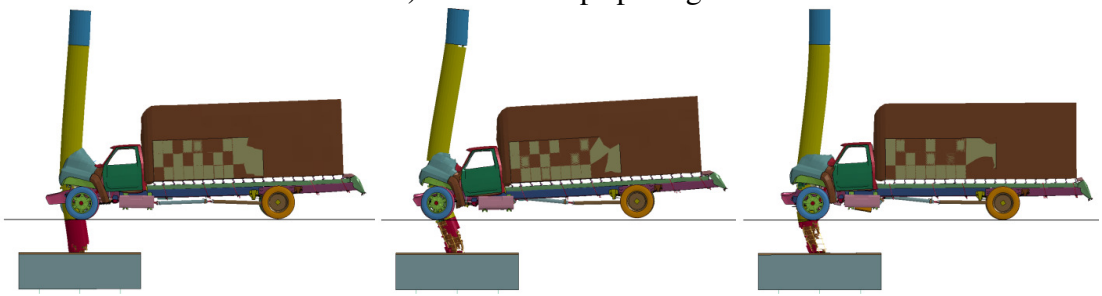

b) 150 mm hoop spacing

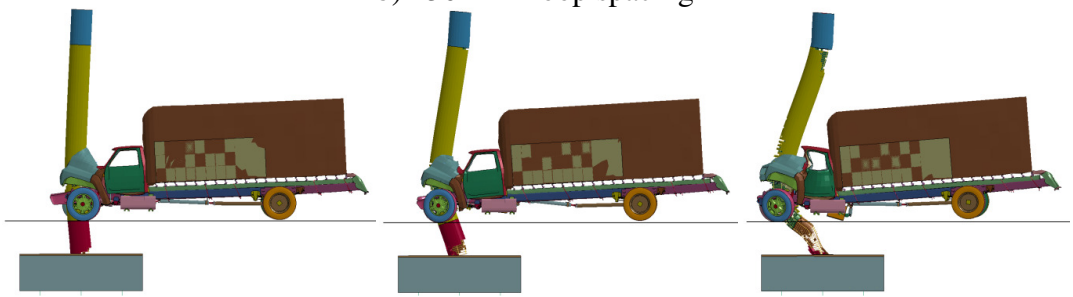

c) 50 mm hoop spacing

Figure 6.5. Collision response at 100 ms for 600 mm diameter pier with different hoop spacing at vehicle impact velocities of 55 (left), 80 (center), and 120 km/h (right)

The results occurring in the 900 mm diameter pier with hoop spacing of 300, 150, and 50 mm are shown in Figure 6.6. The damage resulting from the 55 and 80 km/h vehicle impacts was minimal and did not cause much erosion of the concrete elements. The 120 km/h vehicle impacts caused significant failure at the base of the pier. This type of failure could be expected since high shear forces are generated when there are sharp changes in geometry. It was observed that more damage occurs when the hoop spacing increases and the confinement effect in the concrete core decreases.

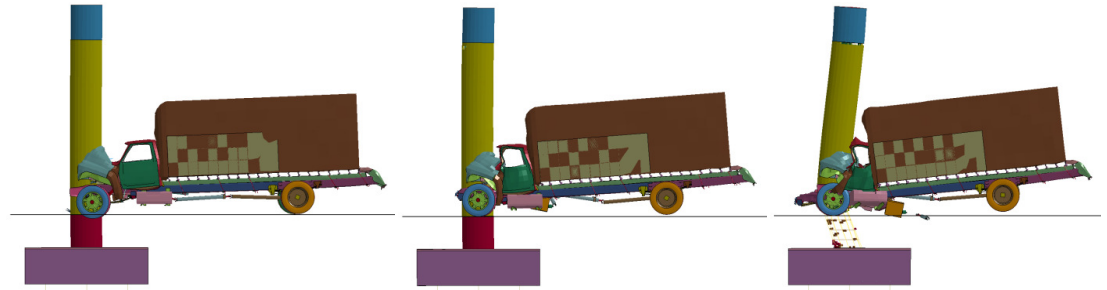

a) 300 mm hoop spacing

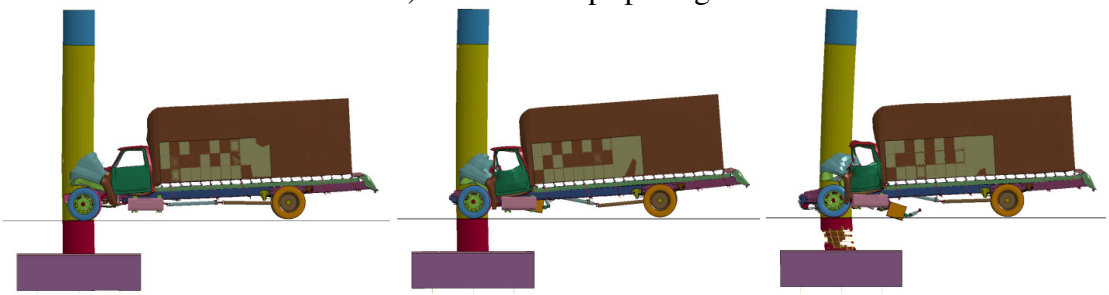

b) 150 mm hoop spacing

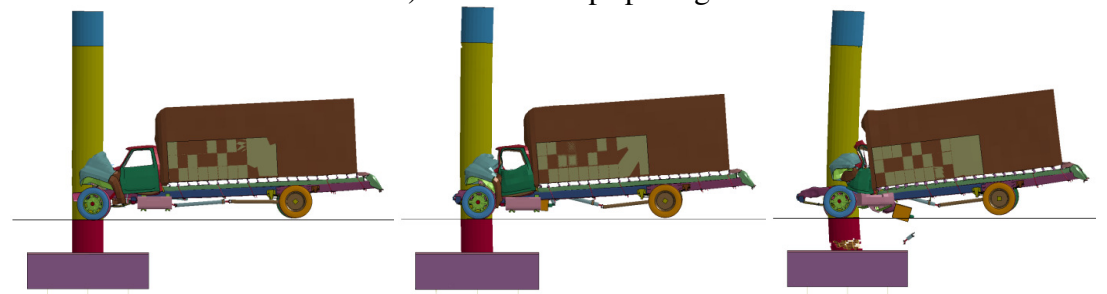

c) 50 mm hoop spacing

Figure 6.6. Collision response at 100 ms for 900 mm diameter pier with different hoop spacing at vehicle impact velocities of 55 (left), 80 (center), and 120 km/h (right)

The 1,200 mm diameter pier had the largest structural stiffness of the piers in this study. As a result, there were no significant failures observed in these piers between varying hoop spacing or due to vehicle impact velocity. This is because, as the stiffness of the pier increases, the amount of impact energy the pier can absorb increases. The results of the vehicle collision with the 1,200 mm diameter pier with hoop spacing of 300, 150, and 50 mm are shown in Figure 6.7.

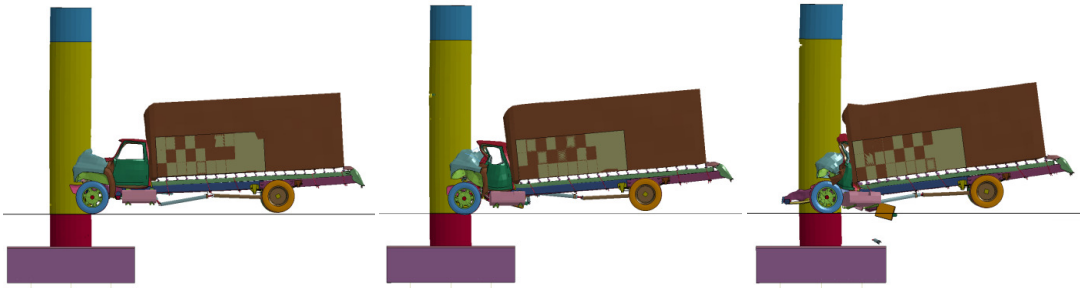

a) 300 mm hoop spacing

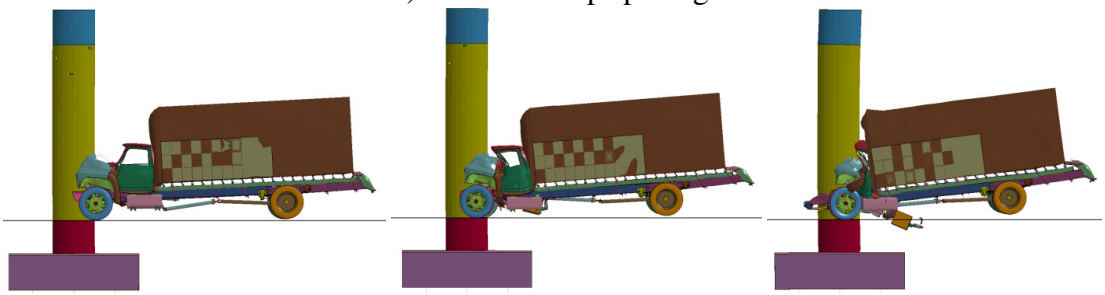

b) 150 mm hoop spacing

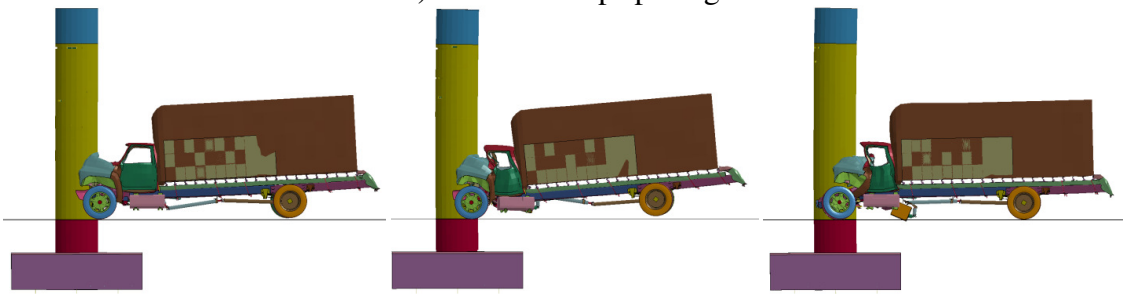

c) 50 mm hoop spacing

Figure 6.7. Collision response at 100 ms for 1,200 mm diameter pier with different hoop spacing at vehicle impact velocities of 55 (left), 80 (center), and 120 km/h (right)

Two types of failure modes were observed as a result of the vehicle collisions: flexural and shear failure. Failure of the longitudinal reinforcement is a sign of flexural failure, where the concrete has cracked due to tensile stresses from the loading and the tensile force is mainly resisted by the steel reinforcement. Plastic hinges form in regions where concentrated inelastic deformations occur due to the stresses exceeding the nominal moment strength of the structure. Examples of flexural failure and plastic hinge formation are observed in the 600 mm diameter piers with hoop spacing of 50, 150, and 300 mm at impact velocities of 80 and 120 km/h, shown in Figure 6.5. Flexural failure was also observed in the 900 mm diameter pier with hoop spacing of 300 mm at an

impact velocity of 120 km/h. Three plastic hinges were formed in this cases: at the location of impact, at the base of the pier, and at the top of the pier. Diagonal tensile cracking through the concrete core is a sign of shear failure. During shear failure, the tensile forces in the concrete cause cracking prior to developing the full flexural strength of the structure. Examples of a shear failure are observed in the 900 mm diameter pier with a hoop spacing of 50 and 150 mm at an impact velocity of 120 km/h. Shear failure was also observed in the 600 mm diameter pier with hoop spacing of 50 and 150 mm at impact velocities of 55 km/h. The diagonal shear failure occurs near the base of the pier and propagates diagonally through the cross-section. No failure modes were observed in the 1,200 mm diameter piers subjected to vehicle collisions. The stiffness of these piers was great enough to absorb the kinetic energy applied to them by the moving vehicle without causing noticeable damage, regardless of vehicle impact velocity or hoop spacing.

6.3.2. Energy Conservation

The energy distribution for the 55, 80, and 120 km/h vehicular impact velocities are shown in Figure 6.8 for the 1,200 mm diameter pier with 300 mm hoop spacing. In general, the energy distribution curves look similar for all of the piers analyzed in this study as can be seen in APPENDIX A. Conservation of energy is one of the key indicators that assure the models are stable, the simulation results make sense, and that energies are being transferred effectively throughout the system. The total energy of the system should remain fairly constant. The kinetic energy is transferred into internal energy, suggesting that the kinetic energy of the moving vehicle is being transformed into

the internal energy that is associated with the deformation of the vehicle and displacement of the bridge pier.

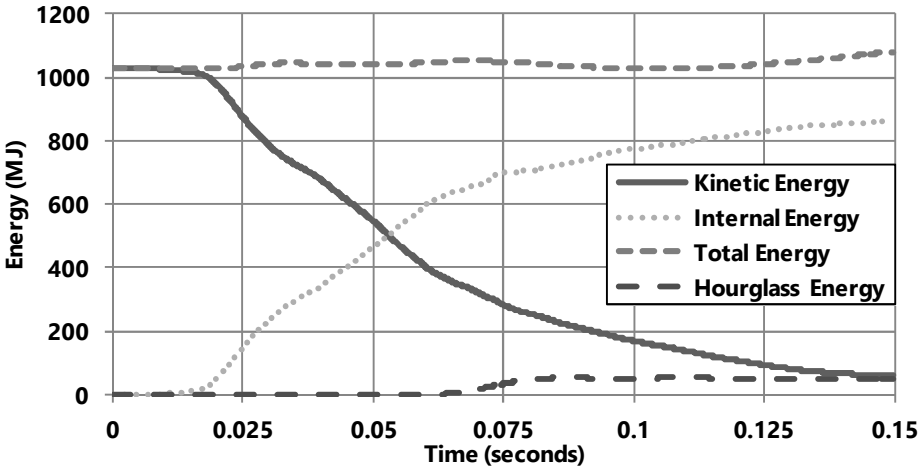

a) 55 km/h impact velocity

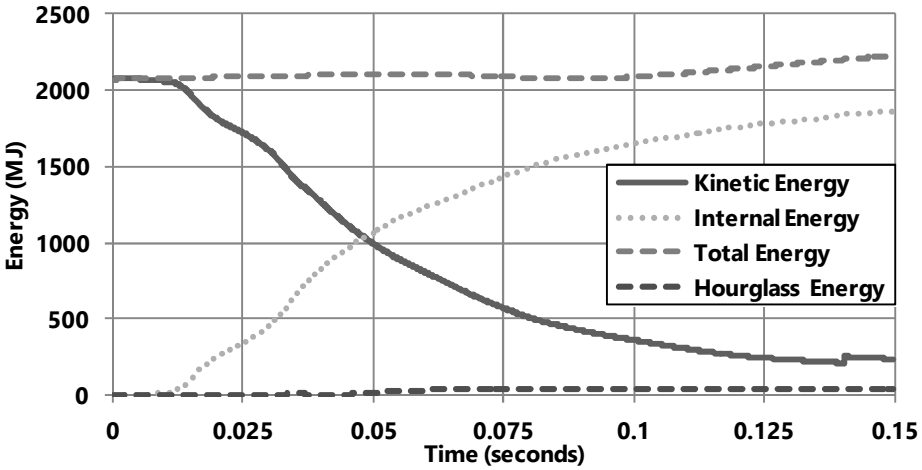

b) 80 km/h impact velocity

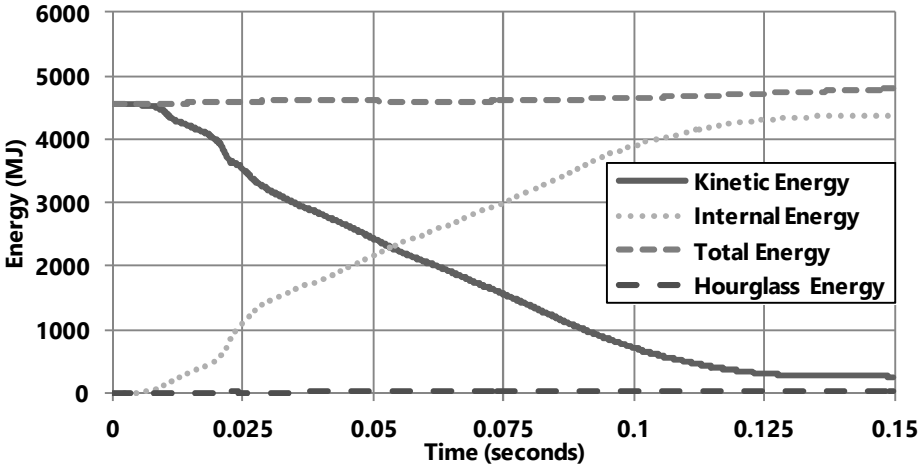

c) 120 km/h impact velocity

Figure 6.8. Energy distribution of the 1,200 mm pier with 300 mm hoop spacing

The maximum kinetic energy in the vehicle impact simulations was checked using Equation 0-1, and was calculated to be 941, 1,990, and 4,480 MJ for the 55, 80, and 120 km/h impact velocities, respectively. The maximum kinetic energy of the simulations was observed to be 1,030, 2,075, and 4,555 MJ for the 55, 80, and 120 km/h impact velocities, respectively. The kinetic energies derived from the simulations were within 10% of the calculated values. The simulations were considered to be correlated well with expected values for kinetic energy.

A major concern in energy conservation is to assure that less than 10% of the total energy is attributed to hourglass energy (Bala and Day 2004). The percentage of hourglass to total system energy is shown in Table 0-2 for the 900 and 1,200 mm diameter piers. Based on the energy distributions from the results, hourglass energy accounted for a very minimal amount of the total energy, ranging from 0.2% to 4.9% of total energy. It can therefore be assumed that the hourglass controls were working properly to minimize hourglassing of the underintegrated solid elements.

Table 0-2. Percentage of hourglass to total system energy

		900 mm Diameter Pier			1200 mm Diameter Pier		
Hoop Spacing (mm)	Impact Velocity (km/h)	Hourglass Energy (MJ)	Total Energy (MJ)	Hourglass to Total Energy Ratio	Hourglass Energy (MJ)	Total Energy (MJ)	Hourglass to Total Energy Ratio
50	55	2.4	1091	0.2%	34.4	1072	3.2%
	80	16.2	2158	0.8%	26.2	2205	1.2%
	120	41.3	4863	0.8%	25.7	4623	0.6%
150	55	13.8	1095	1.3%	36.7	1081	3.4%
	80	16.1	2118	0.8%	26.5	2222	1.2%
	120	22.1	4612	0.5%	29.0	4826	0.6%
300	55	10.3	1059	1.0%	53.3	1082	4.9%
	80	19.1	2221	0.9%	39.6	2230	1.8%
	120	33.2	4743	0.7%	32.1	4794	0.7%

6.3.3. Resultant Impact Force

The resultant impact forces created at the interface between the pier and the vehicle elements were recorded during the analysis. The resultant impact force time histories for the 1,200 mm diameter pier with a hoop spacing of 300 mm are shown in Figure 6.9. The resultant impact force time histories for all of the piers investigated during this study are presented in APPENDIX B. It can be observed that as vehicle impact velocity increases, the peak dynamic force increases. The duration of the peak impact force occurs over a shorter period of time as vehicle impact velocity increases.

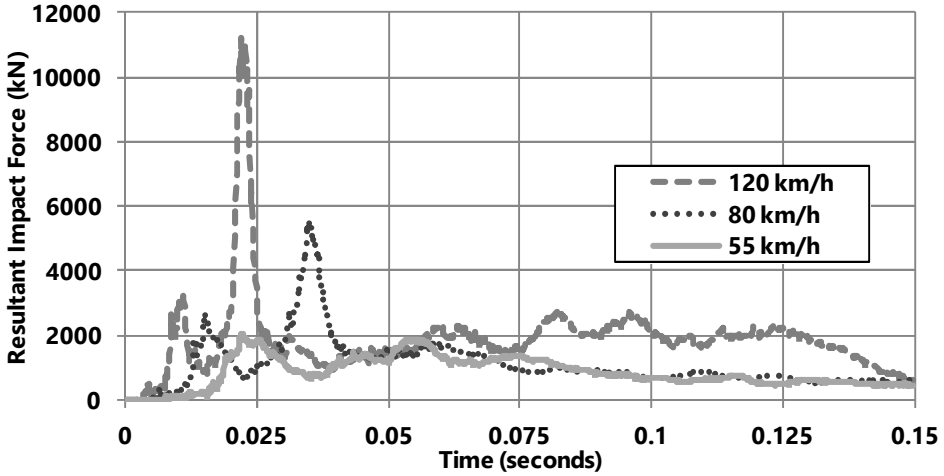

Figure 6.9. Resultant impact force time history at various impact velocities for 1,200 mm diameter pier with 300 mm hoop spacing

A summary of the resultant impact forces is presented in Table 0-3. This table shows the peak dynamic forces (PDF) and the peak 10 ms moving averages of the resultant impact force time histories that occurred between the vehicles and the bridge piers. It should be noted that the 10 ms moving average forces are significantly less than the peak impact forces. It is only for the low impact velocities, 55 km/h for all pier diameters and 80 km/h in the 600 mm diameter pier, that the design impact force is higher than the 10 ms moving average. This highlights the fact that for higher impact

velocities, bridges designed with the AASHTO recommendations would sustain significant damage. The peak 10 ms moving average may act as a better representative value that can be used to determine the forces resisted by the pier over a duration of time, where the structure has time to respond to the impulse loading. A moving average window of 10 ms was considered because it was roughly the duration of the peak impact force.

Table 0-3. Summary of peak dynamic and 10 ms moving average forces

		600 mm Diameter		900 mm Diameter		1200 mm Diameter	
Impact Velocity	Hoop Spacing	PDF (kN)	Peak 10 ms avg. (kN)	PDF (kN)	Peak 10 ms avg. (kN)	PDF (kN)	Peak 10 ms avg. (kN)
55 km/h	50 mm	2,122	1,550	1,997	1,701	2,054	1,738
	150 mm	2,150	1,613	2,081	1,678	2,256	1,841
	300 mm	2,065	1,530	1,978	1,549	2,030	1,661
80 km/h	50 mm	3,311	2,262	4,896	2,687	6,284	3,408
	150 mm	3,234	2,245	4,427	2,704	5,621	3,223
	300 mm	2,905	2,206	4,792	2,702	5,563	3,332
120 km/h	50 mm	7,336	2,802	9,299	4,018	11,966	4,869
	150 mm	6,756	2,762	9,691	4,020	11,650	4,915
	300 mm	7,383	2,696	8,949	4,034	11,203	4,694

It was observed that the PDF increases with an increase of the vehicular impact velocity. The PDF for the vehicle impact velocity of 55 km/h was fairly consistent for all three pier diameters, roughly around 2,000 kN. At medium to high impact velocities, the PDF increased with an increase in pier diameter. Equation 0-6 shows that the an impact force is proportional to the stiffness of the pier and the amount of displacement caused by the collision. As the pier diameter increases, the PDF increases because the structure's stiffness, k, increases resulting in the impact force, f_s, going up. As the impact velocity goes up, the PDF increases because the kinetic energy of the vehicle increases. As the

hoop spacing increases, the PDF decreases because the structure's become more flexible with a decreases in stiffness.

6.3.4. Displacement, Shear, and Moment

At the top of the pier, a large mass represents the weight that a superstructure imposes on the pier. The mass is unconstrained and free to displacement and rotate. The huge mass, however, has a high inertia that resists large lateral displacements. As a vehicle impacts the pier, displacements at the base of the pier are constrained by the soil-structure interaction of the deep pile foundation. At the top of the pier, the lateral displacement is constrained by the large inertia of the superstructure mass. An example of the lateral displacement of a 600 mm diameter pier with a 150 mm hoop spacing subjected to a 55 km/h vehicle collision at different time steps is shown in Figure 6.10. This figure shows the propagation of lateral displacement along the length of the pier over the duration of the impact event. The lateral displacements along the length of the piers for each simulation are shown in APPENDIX C. A summary of the maximum positive and negative lateral displacements of the piers are presented in Table 0-4. Positive displacement occurs in the direction of the applied impact. It was observed that the maximum positive displacement of the pier occurs at the location of impact, and the maximum negative displacement occurs at the top of the pier. It was observed that the pier displacement increases with increasing impact velocity and hoop spacing. This is because the stiffness of the structure decreases as the hoop spacing decreases, allowing for more displacement of the pier under the same amount of impact force. It was also observed that a decrease in pier diameter increases lateral displacement. This is justifiable

since the moment of inertia decreases significantly with a decrease of pier diameter, resulting in a lower lateral stiffness.

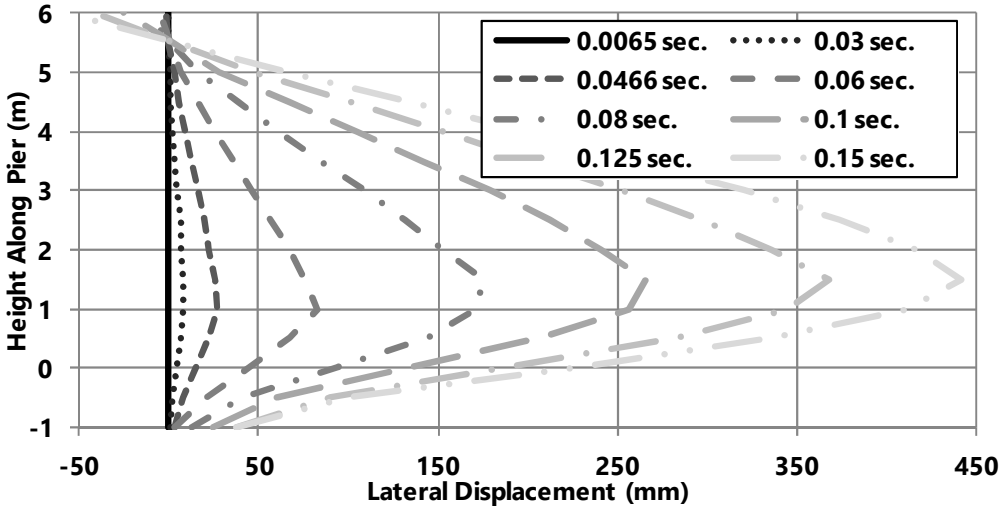

Figure 6.10. Lateral displacement of the 600 mm diameter pier with 150 mm hoop spacing at a 55 km/h impact velocity at different time steps

Table 0-4. Summary of maximum positive and negative lateral displacements in the various piers

		Lateral Displacement (mm)					
		600 mm Diameter		900 mm Diameter		1200 mm Diameter	
Impact Velocity	Hoop Spacing	Postive	Negative	Postive	Negative	Postive	Negative
55 km/h	50 mm	294	-38	13	-2	23	-1
	150 mm	442	-58	38	-2	25	-1
	300 mm	481	-46	24	-2	29	-1
80 km/h	50 mm	920	-62	52	-9	31	-9
	150 mm	828	-59	48	-9	26	-2
	300 mm	916	-51	46	-7	30	-3
120 km/h	50 mm	1269	-38	211	-40	57	-7
	150 mm	828	-59	207	-18	56	-7
	300 mm	1314	-51	550	-32	75	-6

The shear resistances of the circular piers were calculated using the following method described in Section 5.8.3.3 of the AASHTO LRFD Bridge Design Specifications (2012). The shear resistance, V_n, was calculated to be the lesser of:

$$V_n = V_c + V_s + V_p$$ Equation 0-6

$$V_n = 0.25 f_c' b_v d_v + V_p$$ Equation 0-7

in which:

$$V_c = 0.0316 \beta \sqrt{f_c'} b_v d_v$$ Equation 0-8

$$V_s = \frac{A_v f_y d_v (cot\theta + cot\alpha) sin\alpha}{s}$$ Equation 0-9

where f_c' is the compressive strength of the unconfined concrete (MPa), b_v is the effective web width taken as the diameter of the pier (mm), d_v is the effective shear depth determined using Figure 6.11 (mm), s is the spacing of the transverse reinforcement hoops parallel to the longitudinal bars (mm), β is the factor indicating ability of diagonal cracked concrete to transmit tension and shear, θ is the angle of inclination of diagonal compressive stresses (degree), α is the angle of inclination of transverse reinforcement to longitudinal axis (assumed to be 0 degrees), A_v is the area of shear reinforcement within distance s (mm^2). In Equation 0-6 through 6-9, V_c, V_s, and V_p are shear capacities of contributed to the concrete, steel reinforcement and prestressing strands, respectively. The values for β and θ were calculated using the following expressions:

$$\beta = \frac{4.8}{(1+750\varepsilon_s)}$$ Equation 0-10

$$\theta = 29 + 3500\varepsilon_s$$ Equation 0-11

where ε_s is the net longitudinal tensile strain in the section, assumed to be 0.006 mm/mm based on the maximum strain that would occur during a severe impact condition (Buth et al. 2010). A shear resistance factor, φ_v, of 0.9 was applied to determine the nominal shear resistance of the piers. It was assumed that two shear planes would result from the vehicle impact, therefore the nominal shear resistance of the piers were doubled.

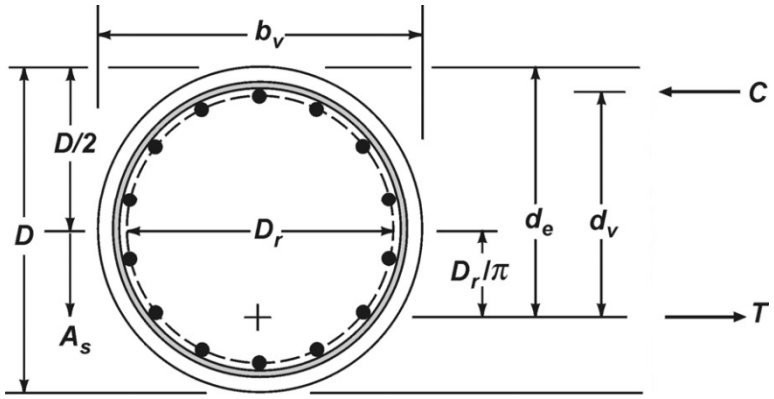

Figure 6.11. Illustrations of terms b_v, d_v, and d_e for circular sections (AASHTO 2012)

The nominal shear resistance of the circular reinforced concrete pier is presented in Table 0-5. A summary of the maximum positive and negative shear forces for the various piers is presented in Table 0-6. The typical shear force distribution for the 600 mm pier with hoop spacing of 50, 150, and 300 mm at the time of peak impact, 466 ms, is presented in Figure 6.12. An example of the lateral displacement of a 600 mm diameter pier with a 150 mm hoop spacing subjected to a 55 km/h vehicle collision at different time steps is shown in Figure 6.13. This figure shows the propagation of shear forces throughout the pier over the duration of the impact event. It was observed that the negative shear forces are generated below the location of impact, and are much greater than the positive shear forces located at the location of impact. These large negative shear forces led to the shear failures in the base of the piers observed in Section 6.3.1. The shear forces at the time of peak impact force for all of the simulations are presented in APPENDIX D. It was observed that the shear forces increase with an increase in impact velocity and pier diameter. Hoop spacing does not have a significant effect on the amount of shear force generated throughout the pier due the vehicle impact, and this is consistent with the observations that the peak impact forces are similar for the same columns with

different hoop spacing. Although a larger hoop spacing decreases the shear capacity, as shown in Table 0-5, the shear force in the pier is not greatly effected.

Table 0-5. Shear resistance for two shear planes as determined by AASHTO (2012)

Nominal Shear Resistance (kN)			
Hoop Spacing	Pier Diameter		
	600 mm	900 mm	1200 mm
50 mm	1019	1653	2319
150 mm	459	781	1134
300 mm	318	562	837

Table 0-6. Summary of maximum positive and negative shear forces in the various piers

		Shear Force (kN)					
		600 mm Diameter		900 mm Diameter		1200 mm Diameter	
Impact Velocity	Hoop Spacing	Positive Shear	Negative Shear	Positive Shear	Negative Shear	Positive Shear	Negative Shear
55 km/h	50 mm	568	-1182	1007	-1761	1129	-1546
	150 mm	557	-1160	1010	-1583	844	-1667
	300 mm	621	-1083	1111	-1537	871	-1534
80 km/h	50 mm	957	-1280	1289	-2664	2263	-3500
	150 mm	928	-1277	1280	-2533	2257	-3231
	300 mm	933	-1282	1242	-2605	2293	-3253
120 km/h	50 mm	1219	-1910	2226	-3138	3133	-4969
	150 mm	1089	-1882	2226	-3338	3172	-5149
	300 mm	1072	-1846	1948	-3130	3170	-4884

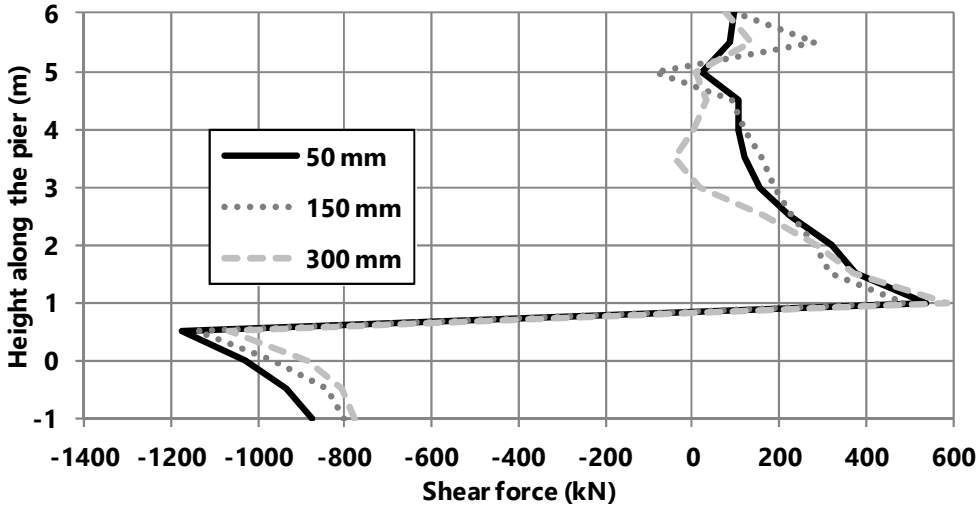

Figure 6.12. Shear distribution for the 600 mm pier with 55 km/h vehicle impact velocity

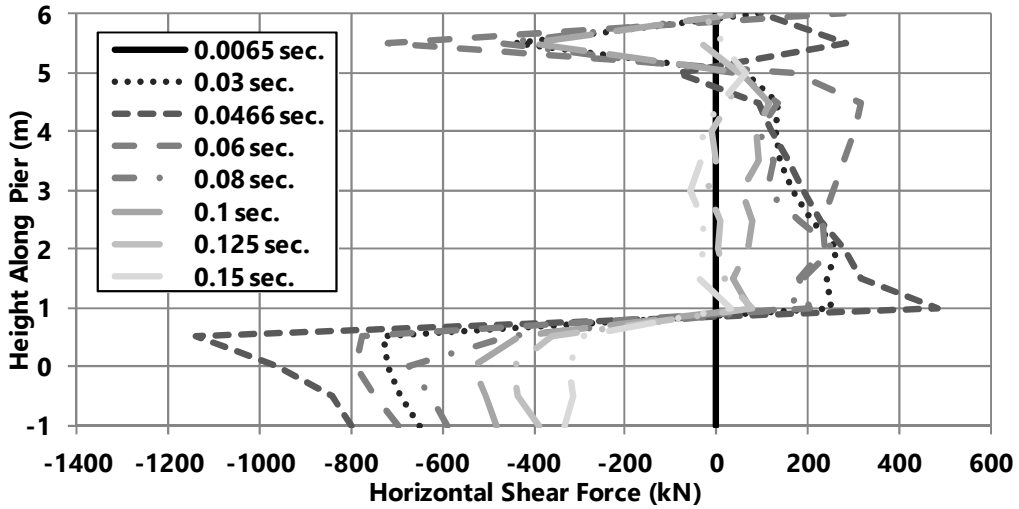

Figure 6.13. Shear distribution along the length of the 600 mm diameter pier with 150 mm hoop spacing at a 55 km/h impact velocity at different time steps

A summary of the maximum positive and negative moments in the pier are presented in Table 0-7. The moments for the various hoop spacing in the 600 mm pier with an impact velocity of 55 km/h are shown in Figure 6.14. The moments along the length of all the simulations are shown in APPENDIX E. An example of the lateral displacement of a 600 mm diameter pier with a 150 mm hoop spacing subjected to a 55 km/h vehicle collision at different time steps is shown in Figure 6.15. It was observed that the maximum and positive moments in the 600 mm diameter pier were consistent for all hoop spacing and vehicle impact velocities. The maximum negative moments occurred where the pier connects to the pile cap, effectively acting as fixed connection. The maximum positive moments occurred at the location of impact. It was observed that the moments increased as the pier diameter increased. This is true because as the stiffness of the structure increases it allows for more absorption of kinetic energy in the pier from the impacting vehicle. At the larger pier diameters, the moments were increased as the vehicle impact velocity increased, because of the increased amount of kinetic energy transferred into the pier. Figure 6.15 shows the time lapse of energy absorption in the

column. At the time of peak impact, 0.466 sec., maximum moment is created at the location of the impact and the closest support, base. Later on, as the energy is propagated throughout the column and the huge mass gets the time to respond, larger moments form in the top portion of the piers.

Table 0-7. Summary of moments in the various bridge piers

		Moment (kN-m)					
		600 mm Diameter		900 mm Diameter		1200 mm Diameter	
Impact Velocity	Hoop Spacing	Positive Moment	Negative Moment	Positive Moment	Negative Moment	Positive Moment	Negative Moment
55 km/h	50 mm	548	-696	960	-1310	1832	-1574
	150 mm	483	-661	875	-1673	1181	-1520
	300 mm	480	-644	903	-1469	1132	-1043
80 km/h	50 mm	567	-677	1295	-1754	2040	-2174
	150 mm	521	-659	1255	-1743	2355	-2003
	300 mm	470	-647	1189	-1726	1950	-2057
120 km/h	50 mm	532	-664	532	-1551	2473	-3225
	150 mm	499	-661	499	-1553	2496	-3251
	300 mm	506	-657	1132	-1548	2342	-3028

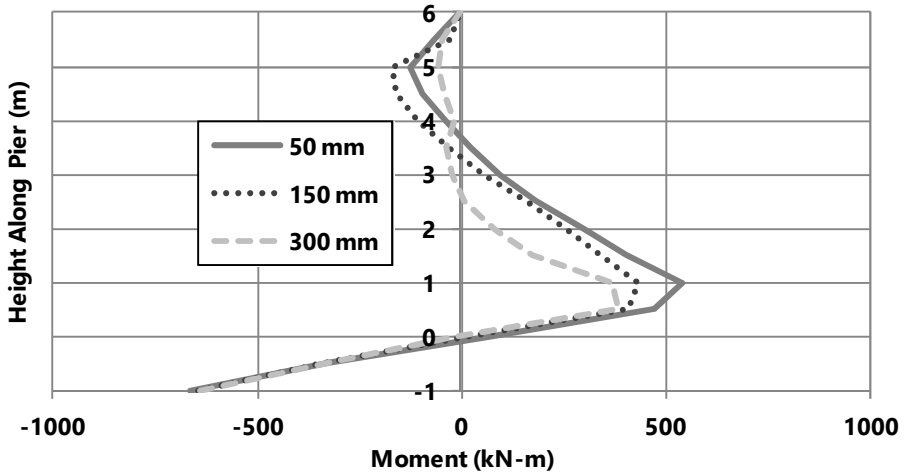

Figure 6.14. Moment distribution of the 600 mm dia. piers at 55 km/h impact velocity

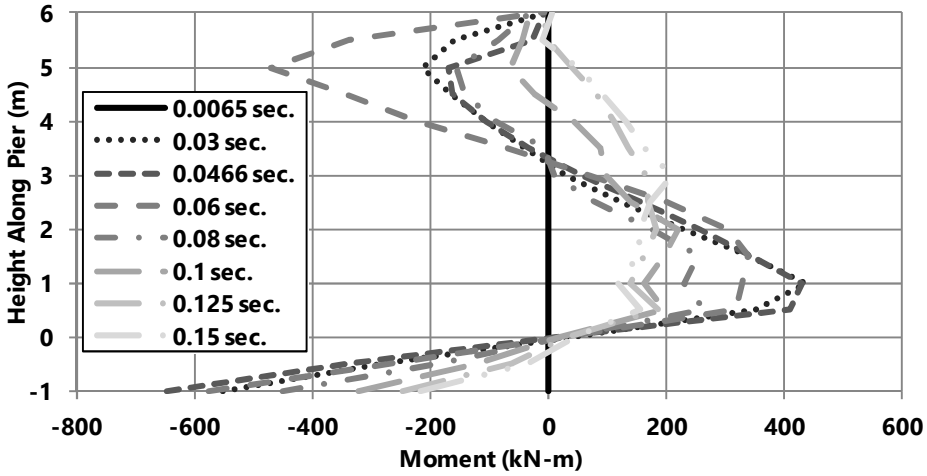

Figure 6.15. Moment distribution along the length of the 600 mm diameter pier with 150 mm hoop spacing at a 55 km/h impact velocity at different time steps

6.3.5. Stresses in Longitudinal Reinforcement

The longitudinal reinforcement of bridge piers plays an important role in resisting tensile stresses resulting from vehicle collisions. When the concrete section cracks, the stresses are redistributed to the transverse and longitudinal reinforcement. Yielding of the longitudinal reinforcement at concentrated locations result in the formation of plastic hinges. Axial force contours were generated, presented in the APPENDIX G, for the 600 mm diameter piers with different hoop spacing and at various impact velocities. Figure 6.16 shows the axial force contours at 80 ms after impact for the 600 mm diameter pier with a hoop spacing of 150 mm subjected to a vehicle impact velocity of 55 km/h. Yielding of the longitudinal bars was observed at the base of the pier, around the area of impact, and at the top of the pier. These were the same areas where plastic hinges were formed. The propagation of axial stresses in the 600 mm diameter pier, with hoop spacing of 150 mm, subjected to 55 km/h impact velocity, is presented in APPENDIX G.

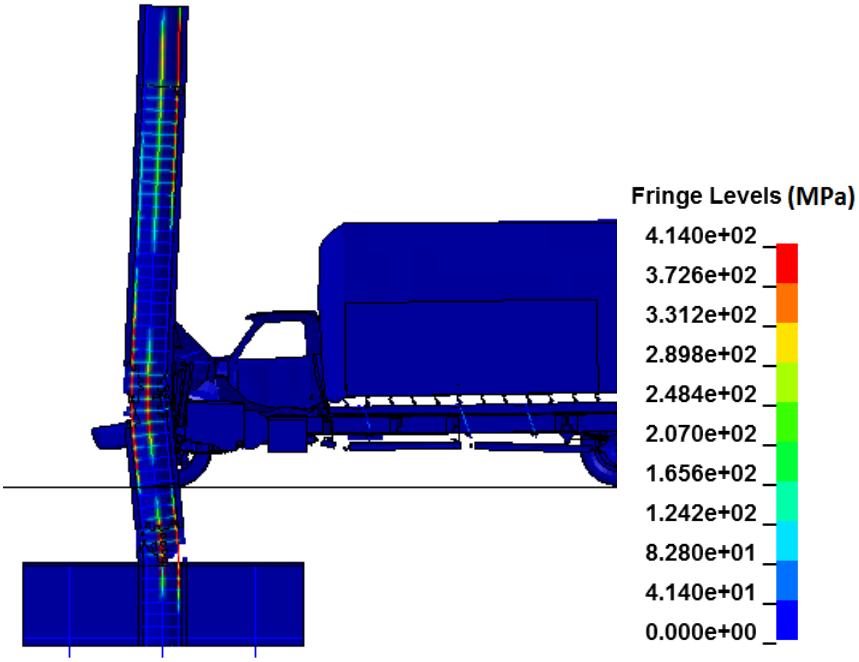

Figure 6.16. Axial stress contours of the steel reinforcement

6.3.6. Pile Cap at Ground Surface Experiment

For the sake of comparison, the top of the pile cap was placed at the ground surface to observe the difference resulting from the vehicle impact. For this simulation, a 600 mm diameter pier, with hoop spacing of 300 mm, and a vehicle impact velocity of 80 km/h was used. The simulation set up is shown in Figure 6.17.

The damage resulting from the vehicle impact was investigated at 75 ms post impact, shown in Figure 6.18. The damage in the pier with the pile cap 1 m below the ground surface was found to be greater than that observed in the pier with the pile cap at the ground surface. Flexural failure was observed in the pier with the pile cap 1 m below the ground surface. Plastic hinges are observed at the base, location of impact, and at the top of the pier. Shear failure was observed at the base of the pier with the pile cap at the ground surface. The pier with deeper pile cap exhibited more extensive damage throughout the portion of the pier below the location of impact, which is a result of having enough length to form a plastic hinge in the pier.

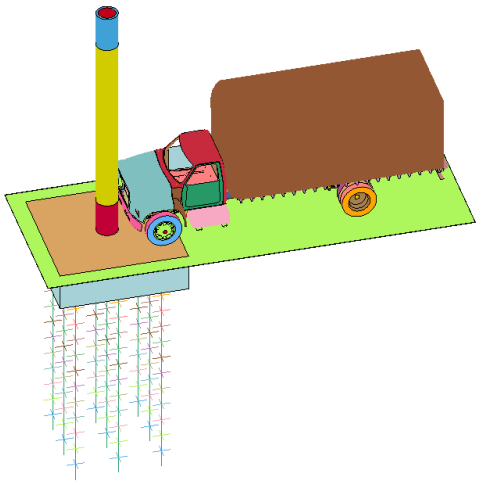

Figure 6.17. Isometric view of the pile cap placed at the ground surface

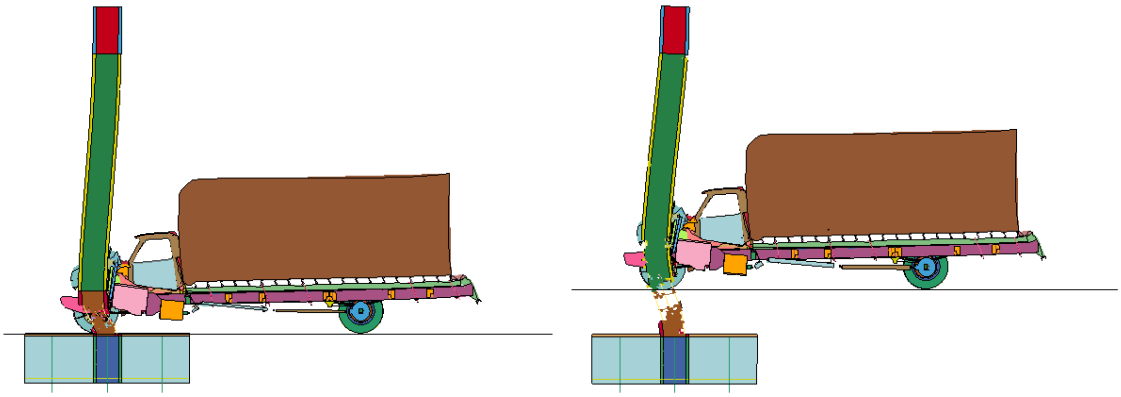

Figure 6.18. Damage resulting from vehicle impact with the pile cap placed at the ground surface (left) and at 1 m below ground surface (right) at 75 ms post impact

The lateral displacement along the X-axis was investigated for these two cases and is shown in Figure 6.19. The lateral displacements along the length of the piers are shown in Figure 6.20, where the dark black lines are the displacements of the pier with the pile cap at 1 m below the ground surface and the gray lines are the pier with the pile cap at the ground surface. It was observed that the lateral displacement of the pier was reduced significantly by placing the pile cap at a higher level. The lateral displacements were graphed at the 35 ms, the time of peak impact force, as well as 50 and 100 ms post impact. The lateral displacement of the pier with the pile cap placed at the ground surface

were less than the displacements with the pile cap 1 m below the ground surface at each time investigated.

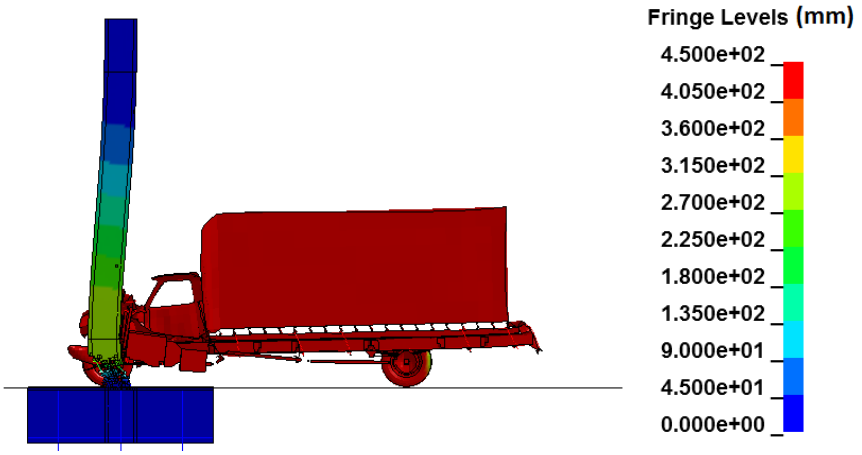

a) Pier with pile cap at ground surface

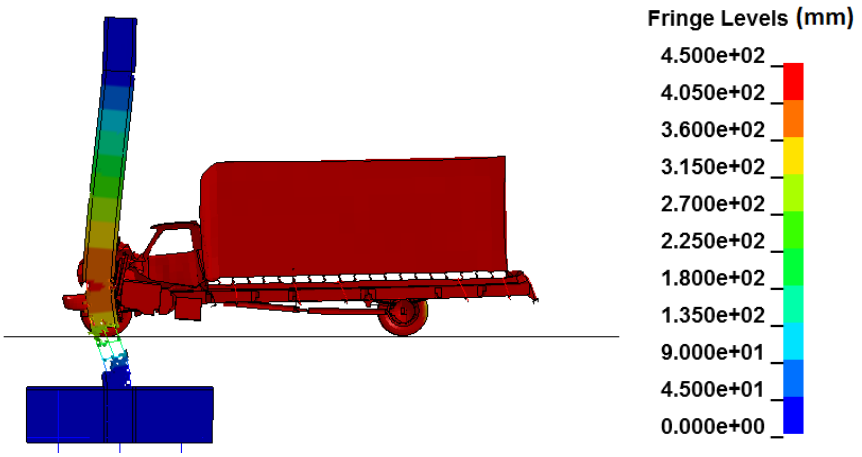

b) Pier with pile cap 1 m below ground surface

Figure 6.19. Lateral displacement in piers in at 75 ms post impact

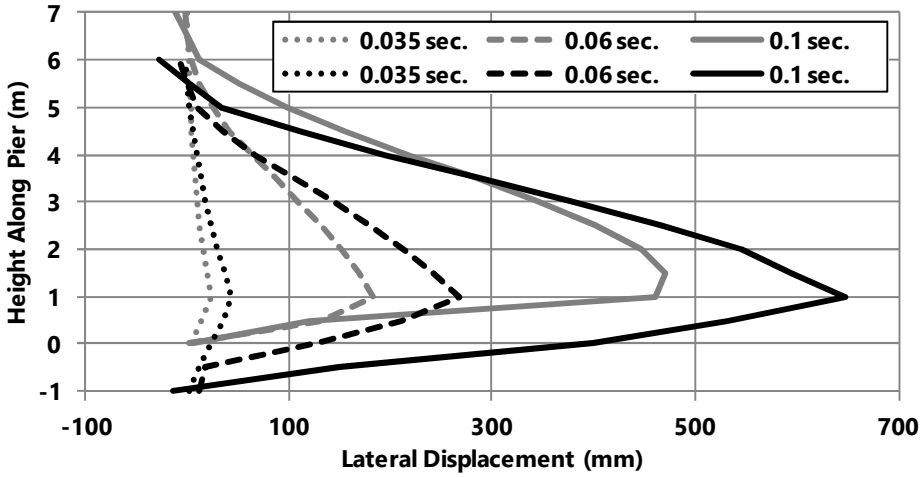

Figure 6.20. Lateral displacement along the length of the pier

The plastic strain of the concrete elements was investigated in the two piers to identify locations where cracking of the concrete occurs. Figure 6.21 and Figure 6.22 show the plastic strains resulting from vehicle impacts with a pier having the pile cap at the ground surface and 1 m below the ground surface, respectively. It was observed that much of the pier was subjected to high strain levels, regardless of the pile cap location.

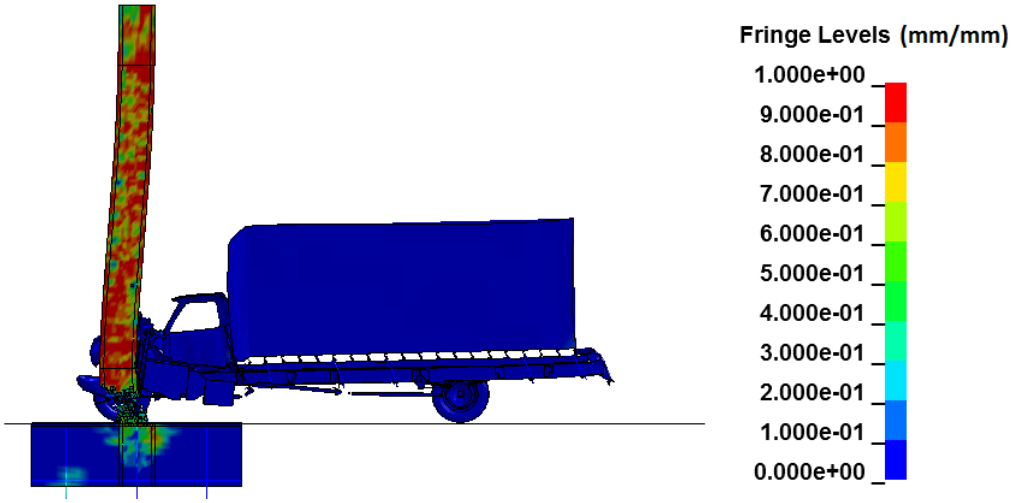

Figure 6.21. Plastic strain in pier with pile cap at ground surface at 75 ms post impact

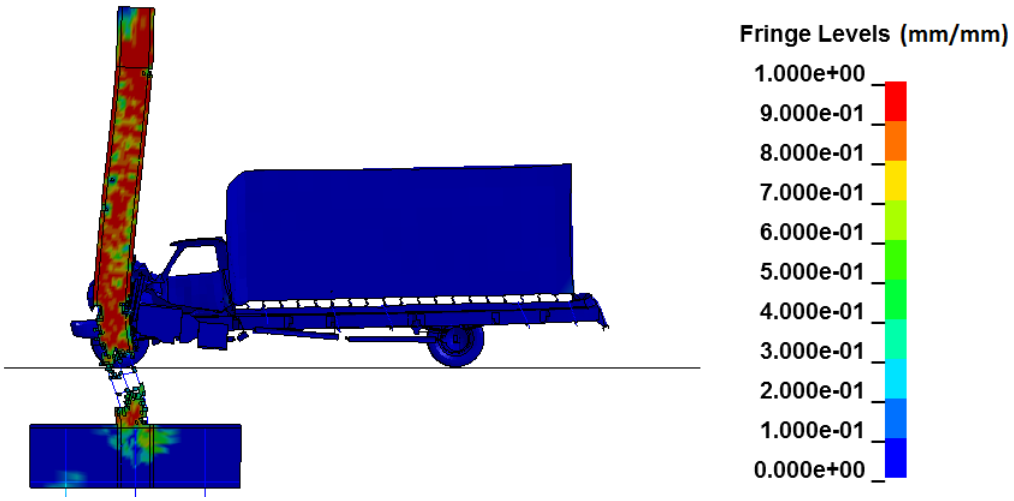

Figure 6.22. Plastic strain in pier with the pile cap below the ground surface at 75 ms post impact

The Von Mises stress was investigated throughout the piers with pile caps at the ground surface, shown in Figure 6.23, and 1 m below the ground surface, shown in

Figure 6.24. The stresses at 75 ms post impact were relatively low, most likely due to the peak impact force, occurring at 35 ms, when the greatest stress would be resisted by the pier.

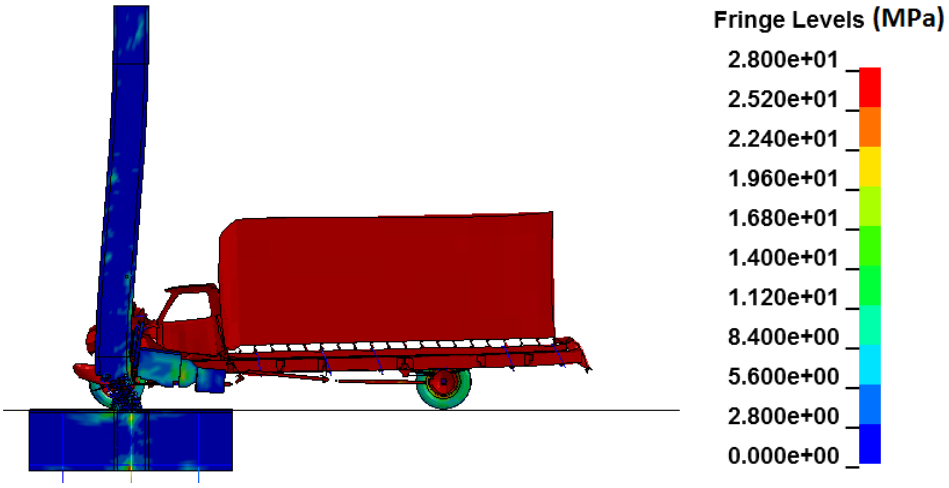

Figure 6.23. Von Mises stress in pier with pile cap at ground surface at 75 ms post impact

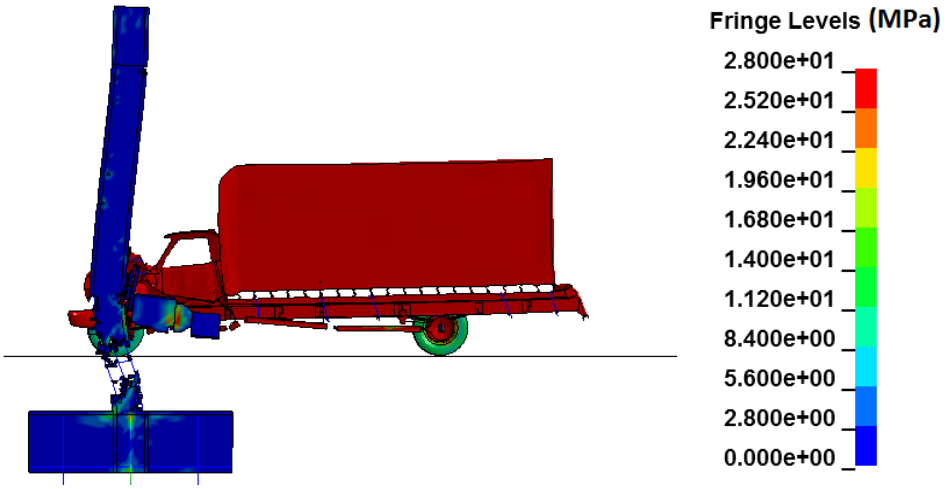

Figure 6.24. Von Mises Stress in pier with the pile cap below the ground surface at 75 ms post impact

The shear and moment forces along the length of the piers, shown in Figure 6.25 and Figure 6.26, respectively, were investigated for the pier with the pile cap at the ground surface and at 1 m below the ground surface. The gray lines are the results of the pile cap being placed 1 m below the ground surface, and the black lines are the results of the pile cap placed at the ground surface. It was observed that the shear stress at the time

of the peak impact force that occurred with the pile cap at the ground surface was significantly higher when compared with the resulting shear with the pile cap 1 m below the ground surface. The shear capacity of these piers was calculated to be around 318 kN. The impact forces exceeded the shear capacity resulting in a shear failure in the pier with pile cap at the ground surface, and flexural failure in the pier with the pile cap 1 m below the ground surface. The shear stresses that occur at the impact location are very similar. The maximum moment that occurs at the base of the piers are almost identical, regardless of pile cap location.

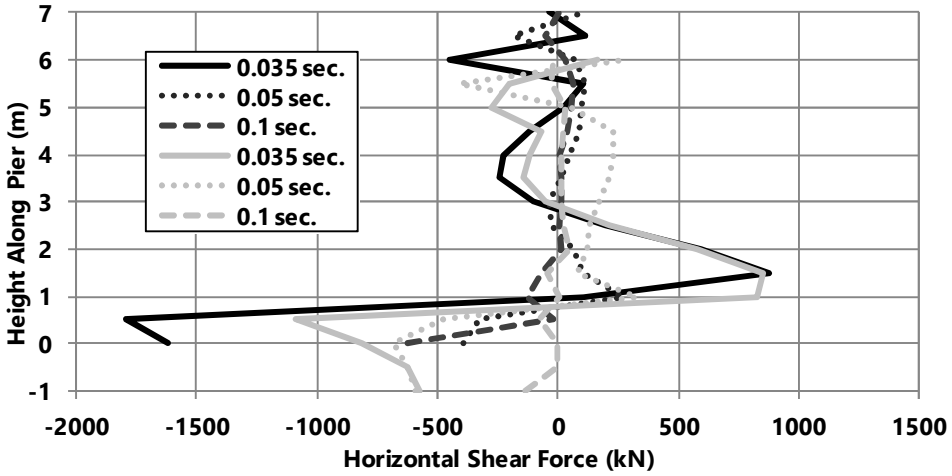

Figure 6.25. Shear force along the length of the piers

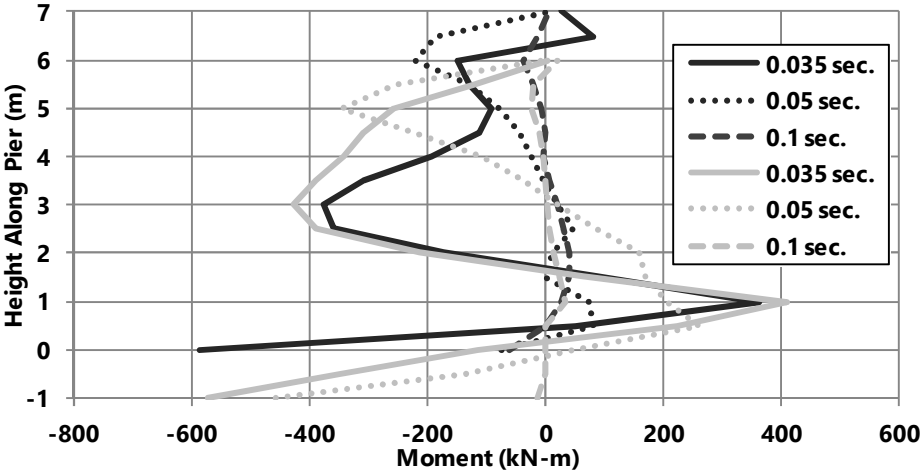

Figure 6.26. Moment along the length of the pier

Based on this study of pile cap depth location, it was observed that pile cap depth had a significant effect on pier displacement, shear force, and the amount of damage resulting from the impact event. The distribution of moment forces throughout the pier differed, but the maximum moment stayed the same, regardless of pile cap depth.

6.3.7. Two Pier Bent Experiment

For the sake of comparison, a two pier bent finite element model was constructed to observe how the structural response differed from that of the single pier with a large mass placed on top of it. In the single pier model, the inertia of the large mass that was used to represent the weight of a superstructure that effectively resists lateral displacement of the top of the pier. In a multi-pier bent, the bent cap aids in resisting lateral displacement and bending of the top of the impacted pier.

For this simulation, a two pier bent was developed using two 900 mm diameter piers, with hoop spacing of 150 mm, and a vehicle impact velocity of 120 km/h. The piers were connected together with a 1 m deep bent cap. The same foundation and boundary conditions were used as mentioned before. The simulation set up is shown in Figure 6.27.

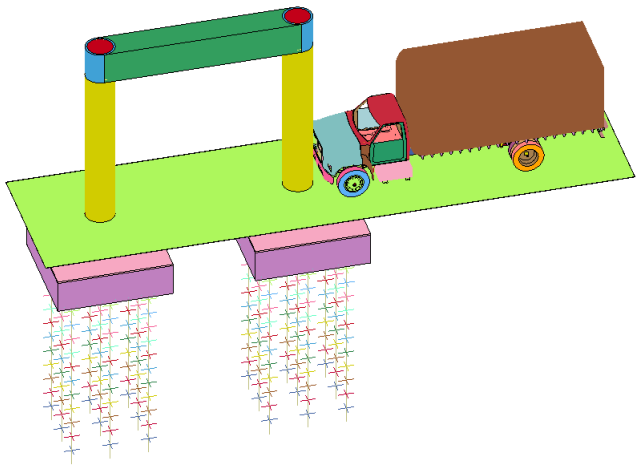

Figure 6.27. Isometric view of the two pier bent test simulation

The results of the two pier bent were compared with the results of the single 900 mm diameter pier with a hoop spacing of 150 mm at an impact velocity of 120 km/h. The resultant impact force time histories, shown in Figure 6.28, illustrate that the force resulting from the vehicle is not affected by the pier being part of a multi-pier bent.

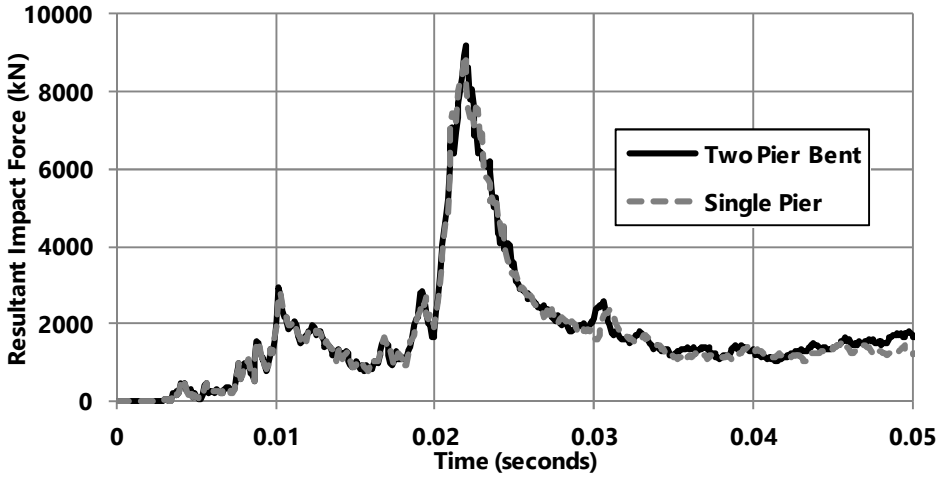

Figure 6.28. Resultant impact force time histories for the single and two pier bent simulations

The damage in the two pier bent, shown in Figure 6.29, was similar to that observed in the single pier simulation, shown in Figure 6.30. The damage was mainly located around the base of the pier, where the pier connects to the pile cap.

In the single pier simulation, some element erosion was observed on the tension side of the pier that was not seen in the two pier bent. This tensile failure is most likely due to the lateral displacement of the pier. The displacement of the two pier bent and single pier bents along the X-axis is shown in Figure 6.31 and Figure 6.32, respectively. From these figures, it was observed that the displacement of the pier at a time of 50 ms post impact was greater in the single pier around the location of the vehicle impact. The lateral displacement along the length of the impacted piers, shown in Figure 6.33, illustrates the difference between the two simulations. The top of the column in the single

pier simulation had the same amount of displacement as the two pier bent simulation. The lateral displacement of the single pier was greater than the two pier bent because the stiffness between the two structures is different. The two pier bent has greater stiffness because the two piers work together, through being connected together by the bent cap, to resist displacements and forces. Increasing stiffness in the piers reduces displacements when they are subjected to the same impact force.

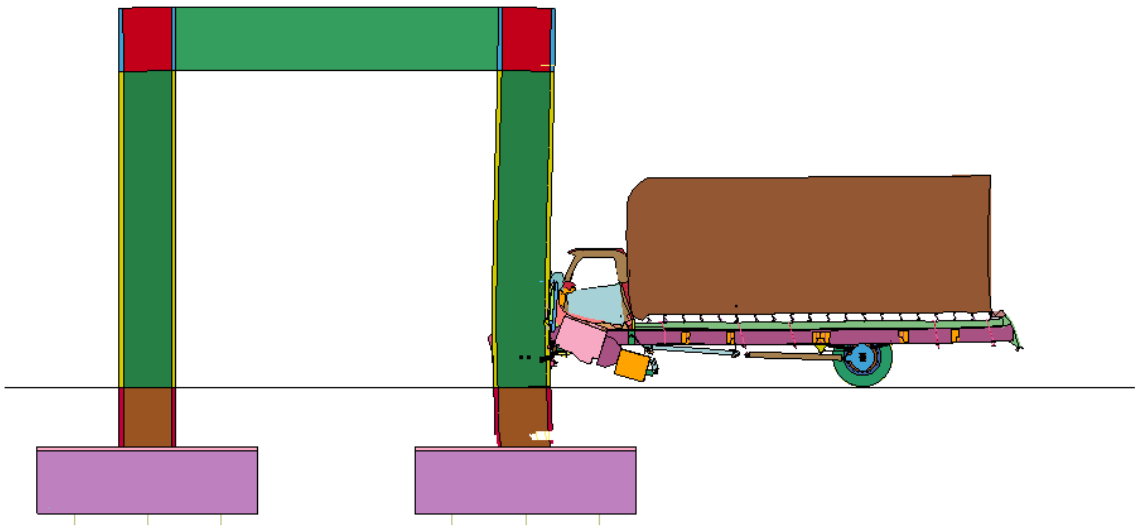

Figure 6.29. Impact result of the two pier bent at 50 ms post impact

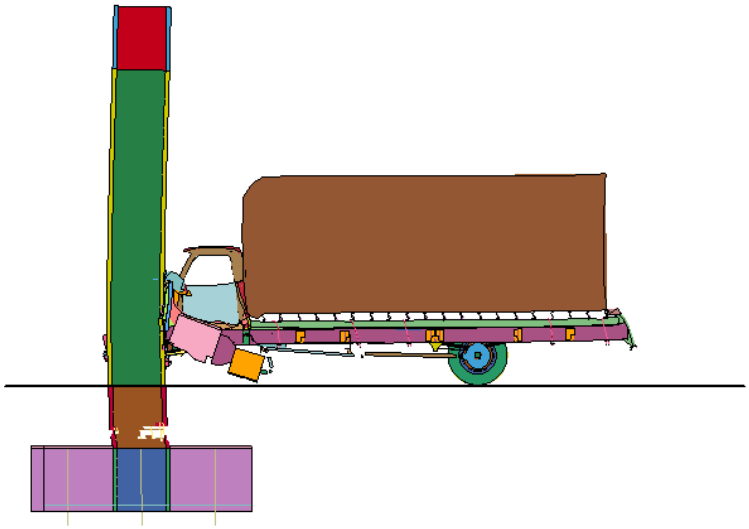

Figure 6.30. Impact result of the single pier at 50 ms post impact

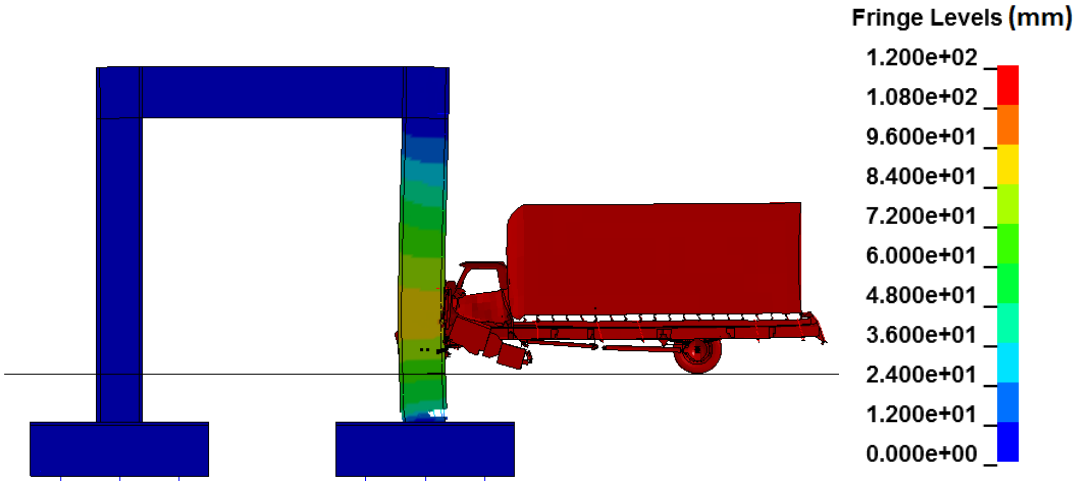

Figure 6.31. Nodal displacements in X-direction for two pier bent at 50 ms after impact

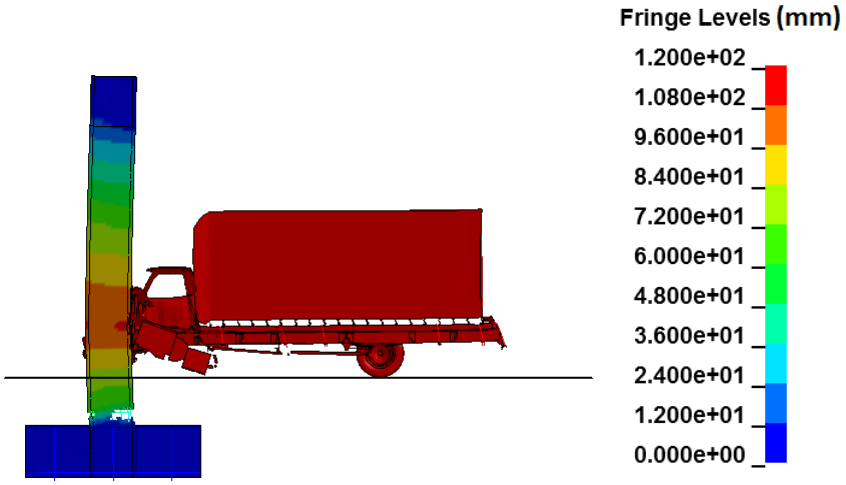

Figure 6.32. Nodal displacements in X-direction for single pier bent at 50 ms after impact

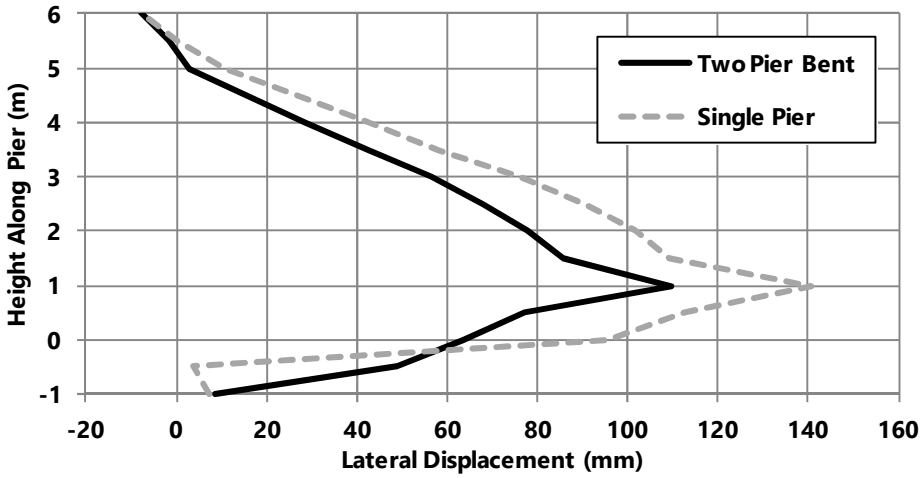

Figure 6.33. Lateral displacement along the length of the impact simulations at 50 ms

The plastic strain of the elements illustrates the possible locations of cracking that occur within the concrete matrix of the pier. The plastic strain of the two pier bent, shown in Figure 6.34, has some noticeable differences from plastic strains in the single pier, shown in Figure 6.35. A noticeable amount of plastic strain occurs within the bent cap at the top of the impacted pier.

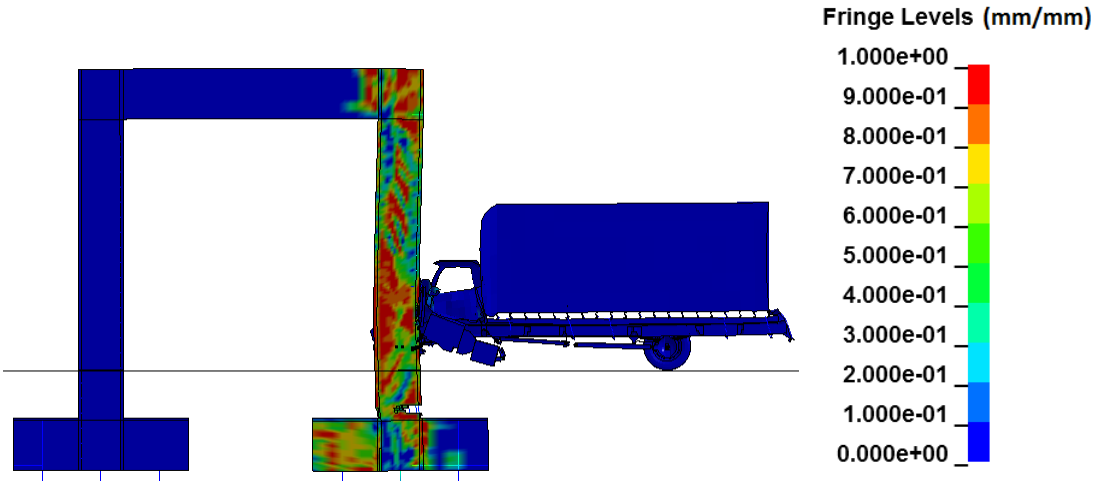

Figure 6.34. Plastic strain contours of two pier bent at 50 ms post impact

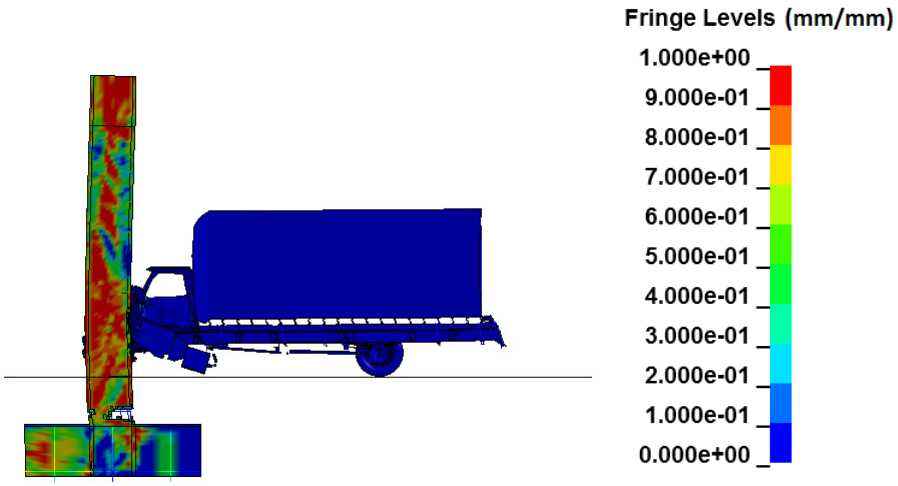

Figure 6.35. Plastic strain contours of single pier bent at 50 ms post impact

The von Mises stress distribution throughout the two pier bent and single pier simulations are shown in Figure 6.36 and Figure 6.37, respectively. The most significant difference between the two simulations is the stress concentration that occurs near the top

of the impacted column in the two pier bent simulation. The bent cap also allows for the redistribution of stresses throughout the structure. The stresses in the neighboring pier are relatively low and resulted in no noticeable damage.

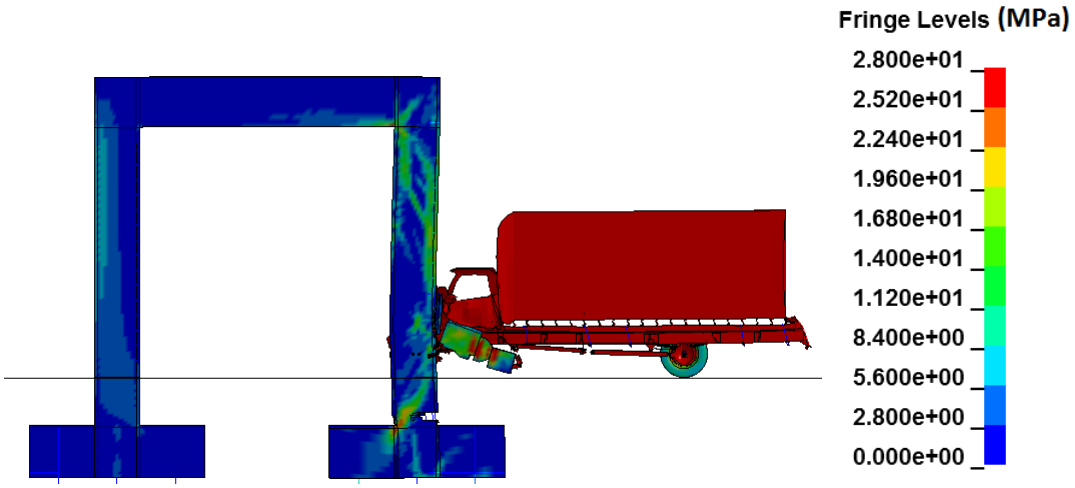

Figure 6.36. Von Mises stress contours of two pier bent at 50 ms post impact

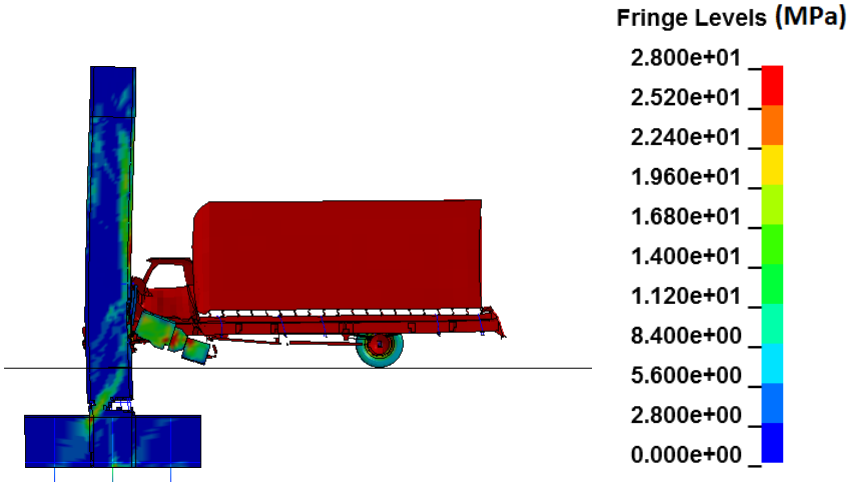

Figure 6.37. Von Mises stress contours of single pier bent at 50 ms post impact

The shear and moment along the length of the piers, shown in Figure 6.38 and Figure 6.39, respectively, were investigated to observe differences between the two pier bent and single pier simulations. The shear and moment forces were considered at the time of peak impact force, 22 ms, and at 50 and 100 ms. The shear and moment forces at the time of peak impact were very similar for both pier configurations. The post peak

impact response in the shear and moment forces was observed to vary at a times of 50 and 100 ms after impact.

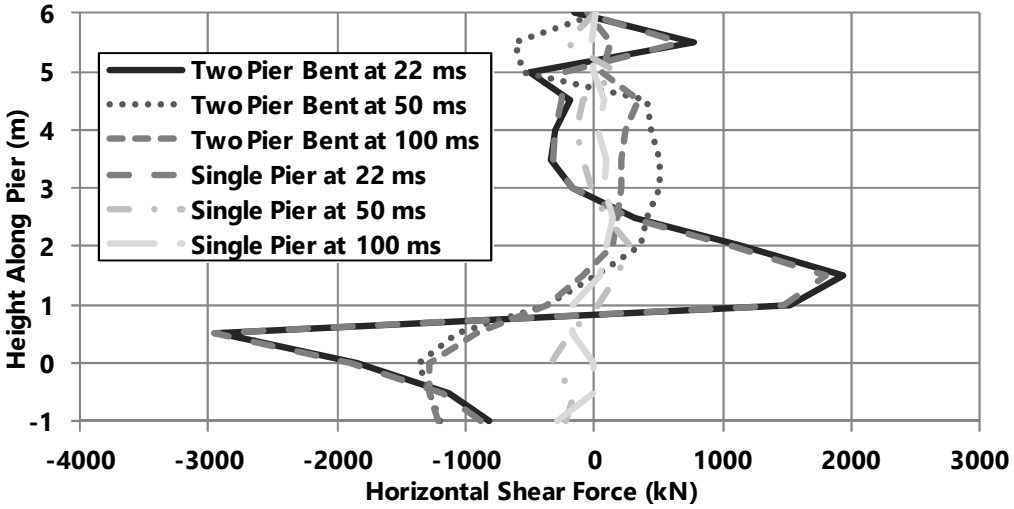

Figure 6.38. Shear force along the length of the piers at 50 ms post impact

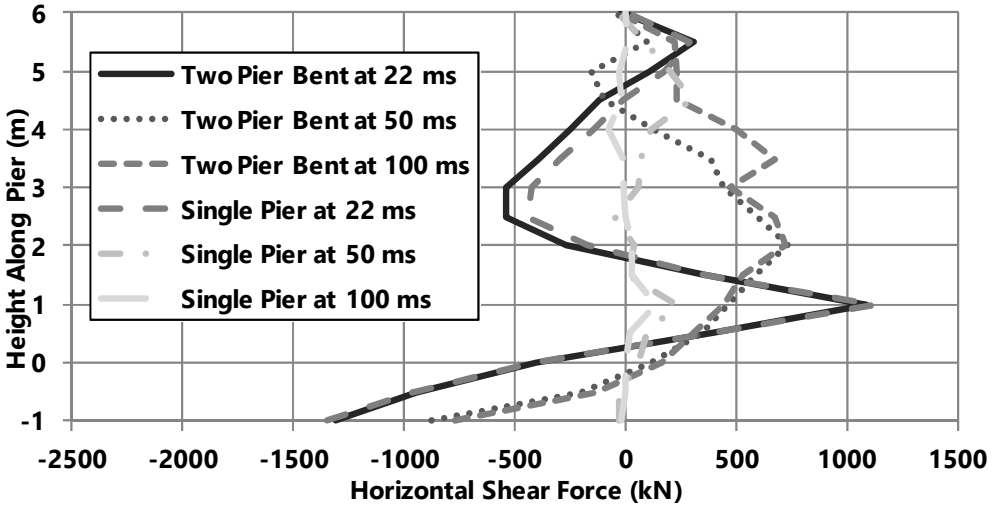

Figure 6.39. Moment along the length of the piers at 50 ms post impact

The difference between these forces is most likely attributable to the pier configurations. The single pier acts as a cantilevered beam, relying on the inertia of the superstructure mass to resist lateral displacement of the free end. In the two pier bent, the stiffness of the structure is greater than that of the single pier because the two piers, connected through the bent cap, work together to resist lateral displacement and distribute stresses. The two pier bent, with more stiffness, has a lower natural period than the single

pier, and therefore the single pier stops vibrating earlier than two pier bent when subjected to the same impact force. It is for this reason that the shear and moments of the single pier are significantly less than those obtained for the two pier bent at the same time steps.

Based on the results of this study, it was observed that modeling a multi-pier bent subjected to vehicular impacts had noticeable effects on the structural response, as compared to a single pier modeled with a large mass placed on top of it. Further research is recommended to observe when a full bridge pier bent is necessary to be modeled for vehicle impact simulations.

6.3.8. Performance-Based Analysis

In order to quantify the results from the impact simulations, a performance-based analysis was conducted using damage ratios. This method was similar to the performance-based design methods for structures exposed to seismic loading and has been investigated by other researchers for use with vehicle impact design (Agrawal 2013; see also Gomez and Alipour 2014). The damage ratio was defined as the ratio of applied peak dynamic force over the shear resistance of the pier. The idea behind this method is that the damage ratio can be associated with various qualitative performance measures of the pier corresponding to different damage states that would result from a vehicular collision. The different damage states consist of minor, major, and extensive. Figure 6.40 depicts examples of each damage state. The description of each damage state is outlined in Table 0-8. Minor damage consists of spalling of the concrete cover and yielding of the longitudinal bars. Major damage consists of longitudinal and transverse reinforcement

bar exposure and shear cracking through the concrete core. Extensive damage consists of bucking of the steel reinforcement bars and loss of axial load capacity in the pier.

(a) (Buth et al. 2010) (b) (Buth et al. 2010) (c) (Smoke et al. 2012)

Figure 6.40. Examples for (a) minor, (b) major, and (c) extensive damage states

Table 0-8. Description of the different damage states

Damage State	Failure Mechanism Description
Minor	Concrete Cover Spalling Yielding of Longitudinal Bars
Major	Exposure of Longitudinal and Transverse Bars Shear Cracking Through Concrete Core
Extensive	Buckling of Reinforcement Bars Loss of Axial Load Capacity

To determine the damage ratio for each simulation that was conducted, the peak dynamic impact forces were extracted from the resultant impact force time histories. The peak impact forces were then divided by the shear resistance of the piers. The shear resistance of the piers were determined using the equations outlined in Section 6.3.4. Tables 6-9 through 6-11 show the peak dynamic forces, shear resistances, and damage ratios for the 600, 900, and 1,200 mm diameter piers given different hoop spacing and impact velocities, respectively.

Table 0-9. Damage ratio for 600 mm diameter pier

Hoop Spacing (mm)	Impact Velocity (km/h)	Peak Dynamic Force (kN)	Shear Capacity (kN)	Damage Ratio
300	55	2065	324	6.4
300	80	2905	324	9.0
300	120	7383	324	22.8
150	55	2150	465	4.6
150	80	3234	465	7.0
150	120	6756	465	14.5
50	55	2122	1025	2.1
50	80	3311	1025	3.2
50	120	7336	1025	7.2

Table 0-10. Damage ratio for 900 mm diameter pier

Hoop Spacing (mm)	Impact Velocity (km/h)	Peak Dynamic Force (kN)	Shear Capacity (kN)	Damage Ratio
300	55	1978	621	3.2
300	80	4792	621	7.7
300	120	8949	621	14.4
150	55	2081	840	2.5
150	80	4427	840	5.3
150	120	9691	840	11.5
50	55	1997	1712	1.2
50	80	4896	1712	2.9
50	120	9299	1712	5.4

Table 0-11. Damage ratio for 1,200 mm diameter pier

Hoop Spacing (mm)	Impact Velocity (km/h)	Peak Dynamic Force (kN)	Shear Capacity (kN)	Damage Ratio
300	55	2030	1009	2.0
300	80	5563	1009	5.5
300	120	11203	1009	11.1
150	55	2256	1306	1.7
150	80	5621	1306	4.3
150	120	11650	1306	8.9
50	55	2054	2491	0.8
50	80	6284	2491	2.5
50	120	11966	2491	4.8

The damage ratios versus vehicle impact velocity was graphed for each one of the piers and their hoop spacing, shown in Figure 6.41. It was observed that the damage ratio increased with an increase in the vehicle impact velocity, as well as with an increase in the hoop spacing. Each simulation was reviewed and assigned an appropriate damage state based on visual damage to the piers. The different damage states are indicated in Figure 6.41 for the 600, 900, and 1,200 mm diameter piers using green for minor, orange for major, and red for extensive damage.

It was observed that the 600 mm diameter pier was susceptible to major and extensive damage at medium to high vehicle impact velocities and at a low damage ratio. The 900 mm diameter pier did not sustain any significant damage at low to medium vehicle impact velocities, but some major and extensive damage was observed at the high impact velocity simulations. The 1,200 mm diameter pier showed no apparent major or extensive damage, regardless of vehicle impact velocity or transverse hoop spacing. Based on these observations, it is apparent that the damage ratios resulting in different damage states vary based on pier diameter and vehicle impact velocity. This suggests that a spectrum of damage ratios, derived from finite element simulations or experimental tests for a range of pier dimensions and vehicle impact velocities, would be required for performance-based design.

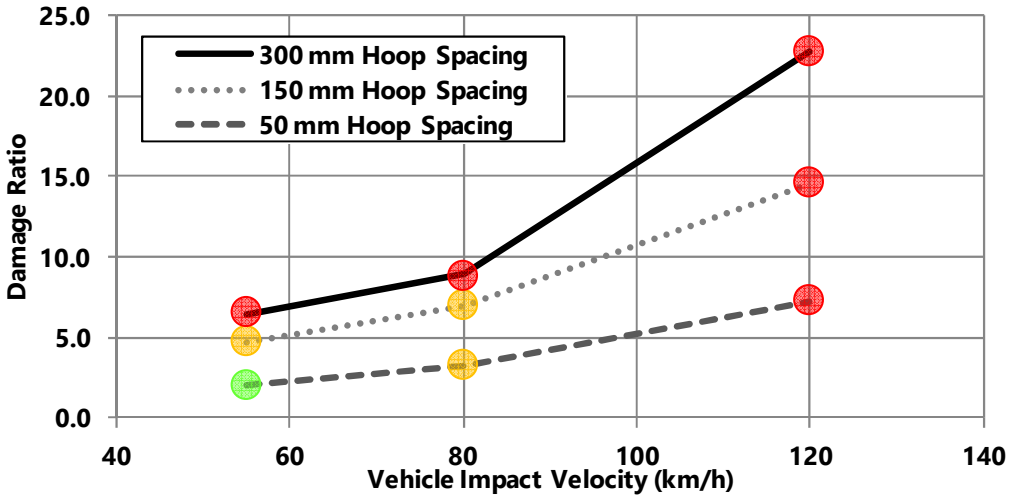

a) 600 mm diameter pier

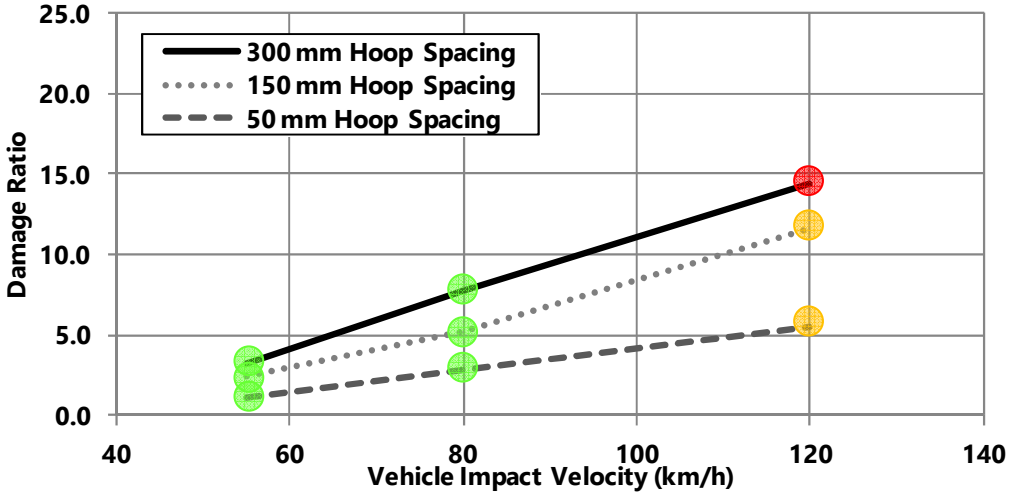

b) 900 mm diameter pier

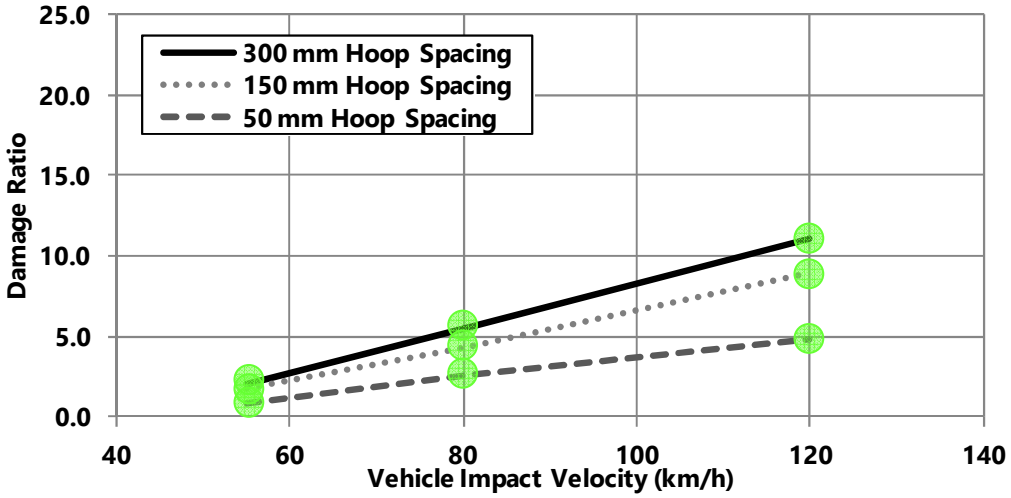

c) 1,200 mm diameter pier

Figure 6.41. Damage ratio vs. vehicle impact velocity for different pier diameters

The methodology used to determine the damage ratios for this analysis could be used to design bridge piers based on a desired performance level for different damage states resulting from vehicular collisions. Bridges can be assigned various performance levels based on their classification of importance to society and national security/defense. Bridges are generally classified based on their need and use by emergency personnel after they are subjected to various earthquakes, but the same classifications could be used for bridge subjected to vehicular collisions (AASHTO 2012). Bridge owners can classify a bridge as one of the following: essential, critical, or other. Essential bridges must be open to emergency vehicles and accessible for security and defense purposes immediately following an extreme loading event. Critical bridges must remain open to all traffic following an extreme loading event and be usable to emergency vehicles and accessible for security and defense purposes immediately following an extreme loading event that exceeds the design impact forces.

The bridge classification could be used in conjunction with the desired performance levels to determine the damage state a bridge pier should be designed for. For example, an essential bridge passes over a low speed highway and is designed to resist major damage when subjected to a vehicular impact. A large diameter pier could easily be used to assure that a vehicle impact would not impede traffic on the bridge. With the bridge owners approval, a slender pier with a high transverse reinforcement ratio could be a more economical choice to sustain the vehicle impact, while still leaving the bridge accessible and usable to emergency vehicles. Alternatively a bridge owner specifies that a 600 mm diameter pier is desired and to be used due to dimension constraints, and the bridge of interest is given a classification of critical importance. A

damage ratio could be specified for the 600 mm diameter pier for various hoop spacing and impact velocities. A damage ratio below 2.0 would result in minor damage to the pier up to an impact velocity of 55 km/h. A damage ratio from 2.0 to 7.0 would result in major damage to the pier up to an impact velocity of 80 km/h. For this case, a pier could be designed to have a damage ratio of 5. This damage ratio would be associated with a major damage resulting from a vehicle impact, but not enough to cause failure of the entire bridge. For higher impact velocities, a larger pier would be recommended. If a larger pier was selected, a new range of damage ratios would be specified for the different damage states depending on pier dimensions and characteristics.

A sensitivity analysis was conducted to evaluate the impact of different parameters, such as pier diameter, hoop spacing, vehicle impact velocity, pile cap height, and multi-pier configuration, on the failure of bridge piers subjected to vehicle collisions. It was observed that parameters that increased the stiffness of the piers led to increases in peak dynamic impact forces, decreased lateral displacements, and higher resistances to shear and moment stresses. A performance-based analysis was conducted to observe what damage states result from various impact forces and pier parameters. The damage states are associated with different damage ratios that result from vehicle impact forces and the shear resistance of the piers. This method of analysis could be used to design safer and more economical piers.

CHAPTER 7.

CONCLUSIONS

Vehicle collisions with bridge piers can cause serious damage to bridge components and lead to catastrophic failure of the entire bridge. Damage, resulting from vehicle collisions, can have profound effects on local communities by shutting down major traffic routes, paying for repairs, and loss of life during the event. The design specifications use an equivalent static load to design for vehicle collision loading events. Research has revealed that the design specifications underestimate the forces that are generated during an impact event and suggest developing an alternative method of design. The preceding study outlines different methods of validating and developing finite element models that simulate vehicle collisions with bridge piers.

It was shown in Chapter 2 that vehicle collisions with bridge piers can pose a serious threat to the nation's infrastructure. The interaction and design forces generated from vehicles impacting bridge piers is not fully understood by researchers. Due to the expensive nature of conducting full-scale experiments, many researchers study vehicle collisions with bridge piers using finite element codes, such as LS-DYNA. One recent experiment that has been conducted led to changes in the design specifications, suggesting that many bridge piers built prior to the changes no longer meet design standards.

It was shown in Chapter 3 that conservation of energy can be used to determine impact forces. The equation for work can be used to determine the amount of force required to displace a pier over a given distance. The mass of the vehicle and impact velocity have a profound influence on the force applied to a bridge pier resulting from a

vehicle collision. An equivalent static force can be determined if the stiffness and displacement are known. The equations presented in this chapter are only useable in instances where the deformation of the bridge piers is elastic.

It was shown in Chapter 4 that impact loading events could be modeled using certain material properties and finite element controls in LS-DYNA. Material models 24 and 159 were found to accurately model the behavior of steel reinforcing bars and concrete, respectively. Strain rate effects for the steel reinforcement were effectively modeled using the methods outlined by Malvar and Crawford (1998). An automatic surface-to-surface contact algorithm was able to model the contact between different objects in the simulation. It was observed that hourglass control had a significant effect on energy conservation, nodal displacements, and impact forces.

It was shown in Chapter 5 that the vehicle models available through the NCAC and NTRCI can accurately and efficiently simulate vehicle collisions with bridge piers. The C2500 pickup truck and F800 SUT vehicle models were validated by comparing vehicle damage and peak dynamic impact forces with published results. It was observed that type 5 hourglass control, with a coefficient of 0.05, effectively controlled hourglassing of the under-integrated solid elements. It was observed that a model must be preloaded under the acceleration due to gravity and have a detailed foundation in order to obtain accurate displacements of the pier resulting from impact loading.

Chapter 6 consisted of developing a set of bridge pier models to be used for a sensitivity analysis. It was shown that implicit dynamic relaxation was an efficient way of preloading a model under the acceleration due to gravity. The interaction between the deep pile foundation and the surrounding sandy soil was efficiently modeled using the

API method for determining load-displacement (p-y) curves. The sensitivity analysis was conducted to evaluate failures in bridge piers with varying parameters. It was shown that as the stiffness of the piers increased, there was an increase in peak dynamic impact forces, a decrease in lateral displacements, and an increased resistance to shear and moment stress. Increasing pier diameter, using a multi-pier bent, or decreasing hoop spacing all lead to increased stiffness of the bridge piers. Vehicle impact velocity has a significant effect on the amount of kinetic energy that must be absorbed by the pier and colliding vehicle. A performance-based analysis showed that the impact force and pier resistance can be used to determine a damage ratio. The damage ratios can be used to design bridge piers for specific damage states resulting from vehicle collisions.

Overall, the preceding study lays the foundation for future research to be conducted on bridge piers subjected to vehicle collisions. The finite element code LS-DYNA was used to conduct this research. The finite element controls, material properties, and vehicle models have been validated and used with confidence to draw conclusions from the simulations results. The sensitivity analysis showed how increasing structural stiffness causes an increase in peak dynamic impact force, decrease in the lateral displacement of the pier, and an increase in the amount of shear and moment that can be absorbed in the pier. The impact velocity of the vehicle was observed to increase the amount of kinetic energy that had to be absorbed in the pier and vehicle. The higher the impact velocity, the larger the amount of damage caused throughout the pier. A performance-based design approach to constructing bridge piers would allow engineers to design piers to resist a particular amount of damage based on specific impact forces and

shear resistance. This design approach had the potential to be more conservative than the design specifications, and can allow for safer and more economical bridge piers.

APPENDIX A.

ENERGY DISTRIBUTION RESULTS

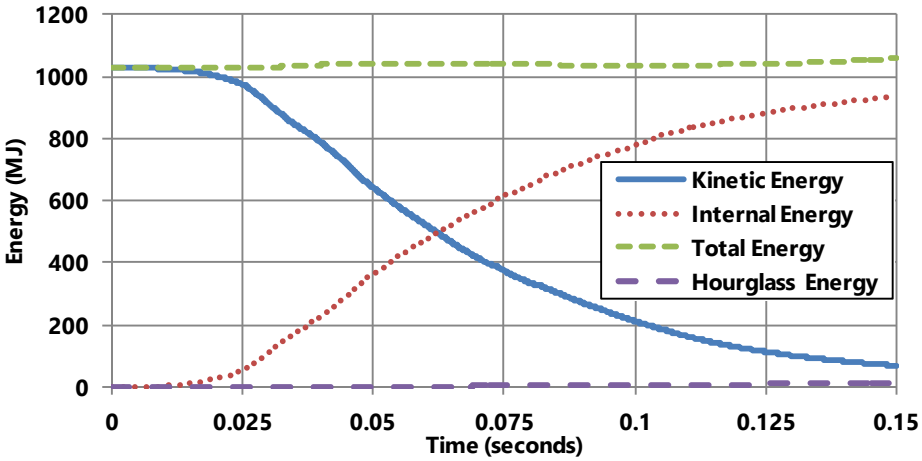

a) 55 km/h impact velocity

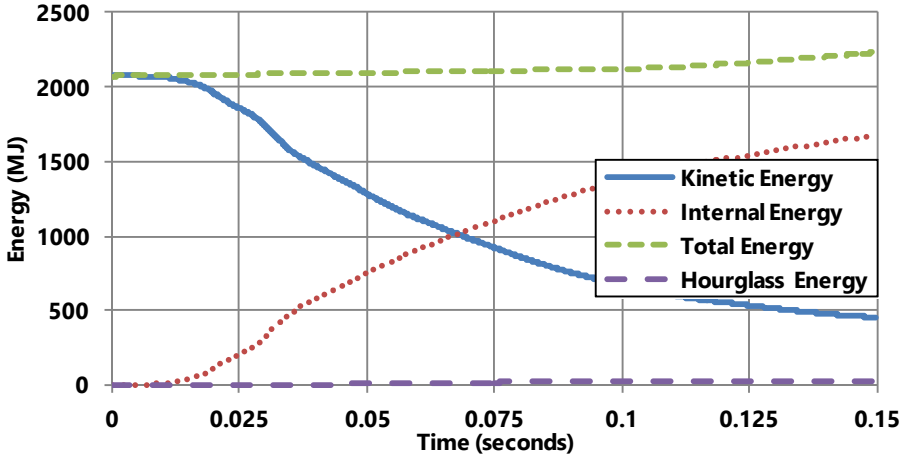

b) 80 km/h impact velocity

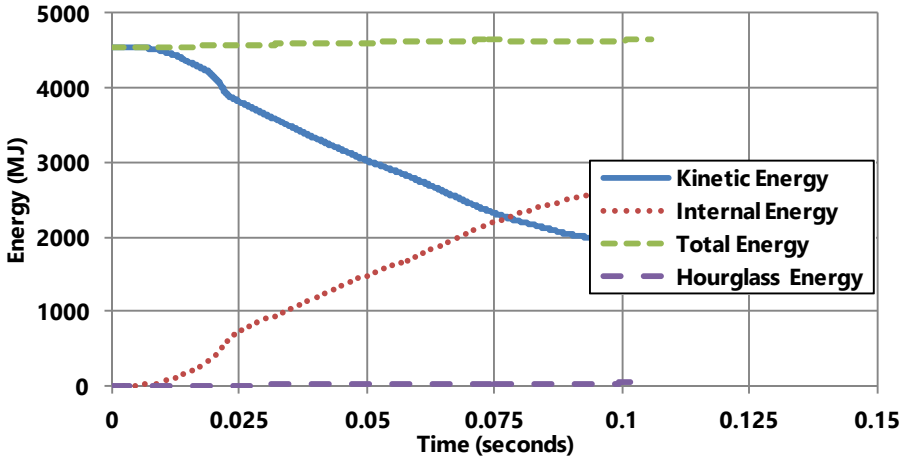

c) 120 km/h impact velocity

Figure A.1. Energy distribution for the 600 mm diameter pier with 50 mm hoop spacing at different impact velocities

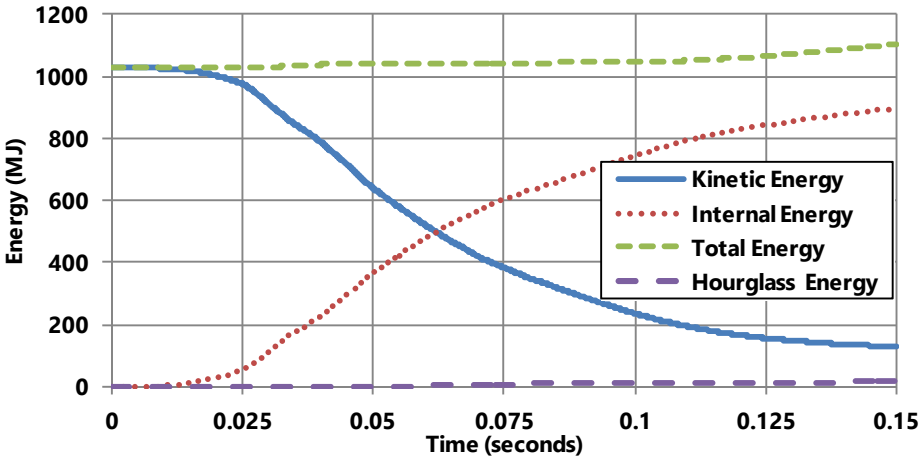

a) 55 km/h impact velocity

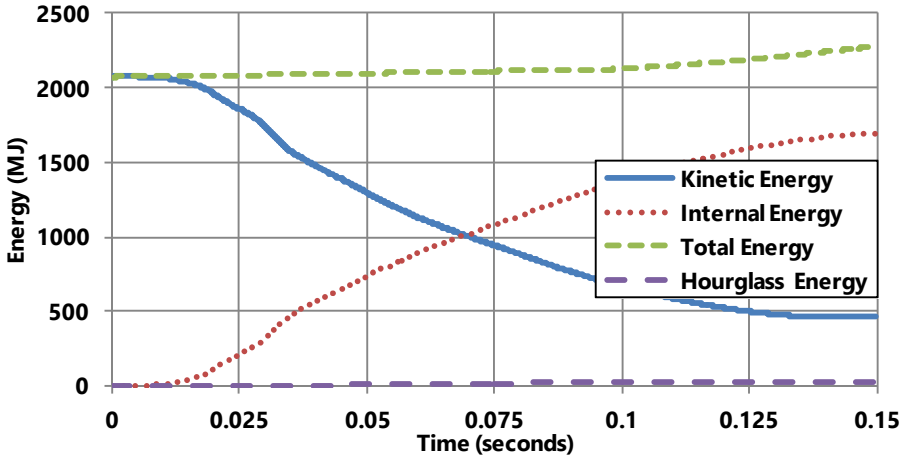

b) 80 km/h impact velocity

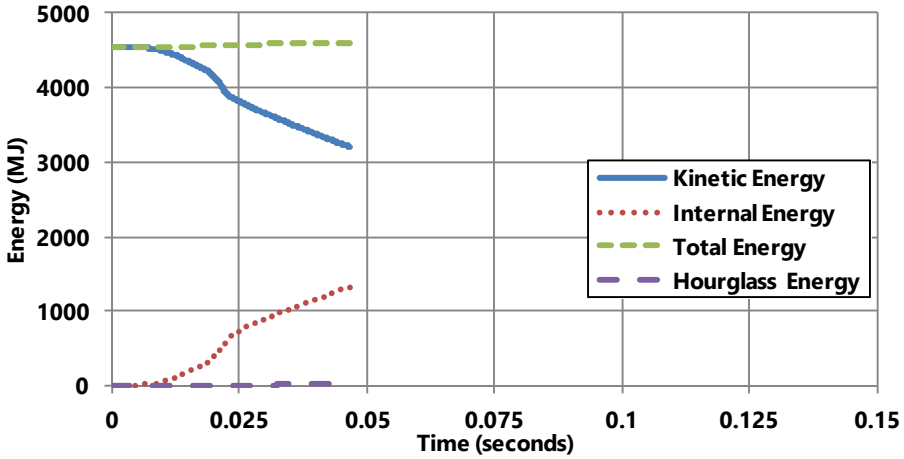

c) 120 km/h impact velocity

Figure A.2. Energy distribution for the 600 mm diameter pier with 150 mm hoop spacing at different impact velocities

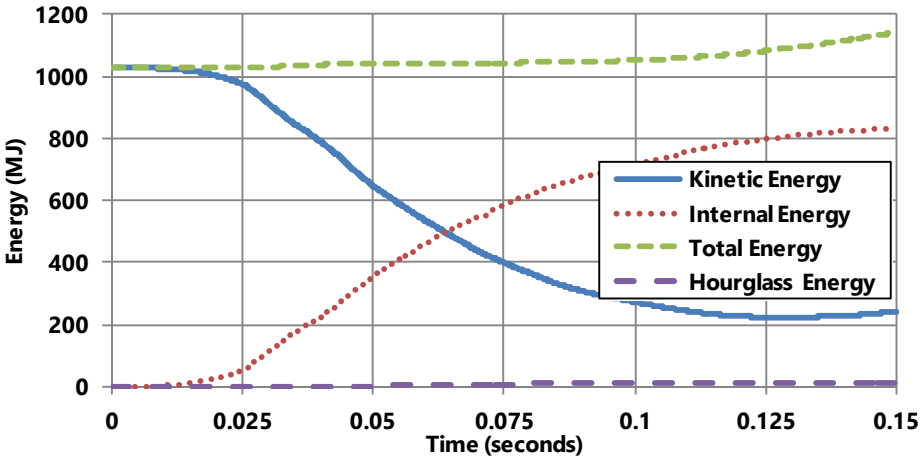

a) 55 km/h impact velocity

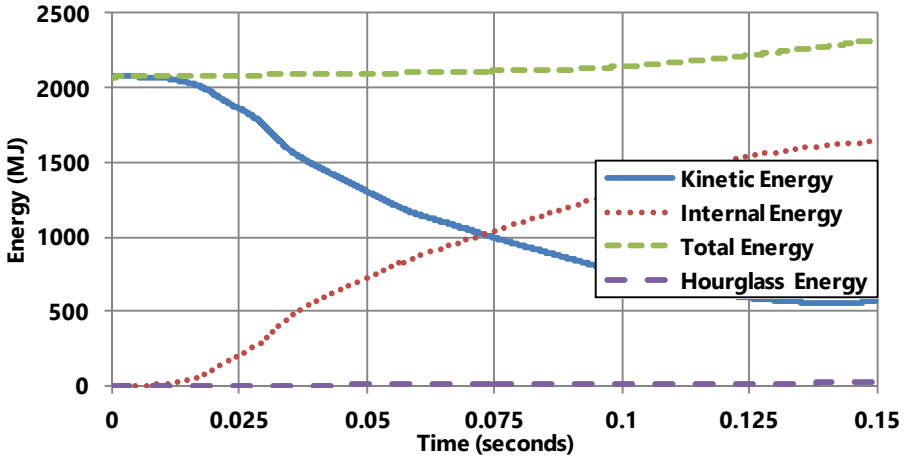

b) 80 km/h impact velocity

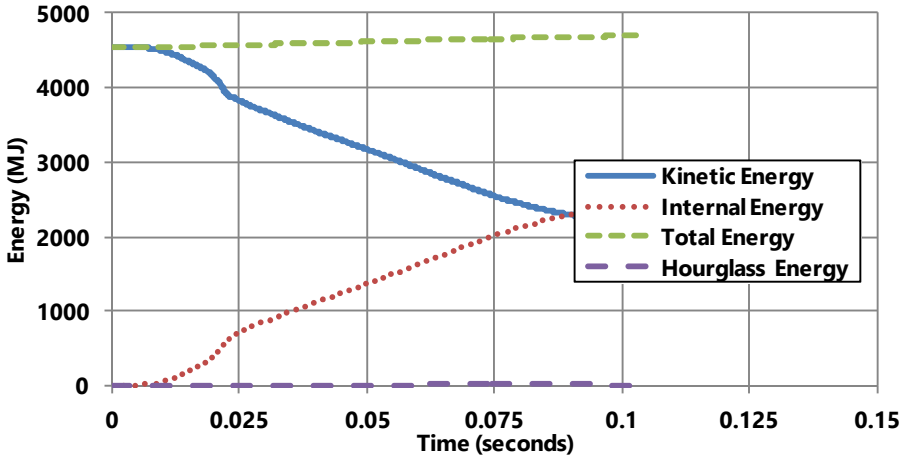

c) 120 km/h impact velocity

Figure A.3. Energy distribution for the 600 mm diameter pier with 300 mm hoop spacing at different impact velocities

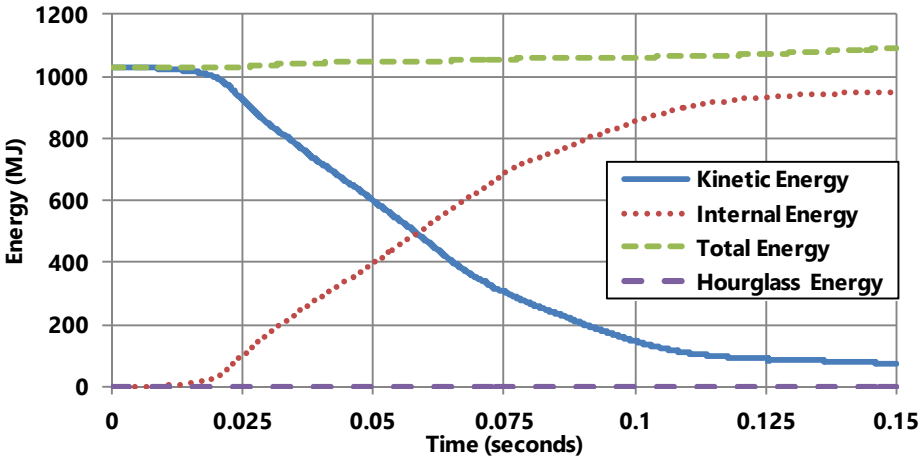

a) 55 km/h impact velocity

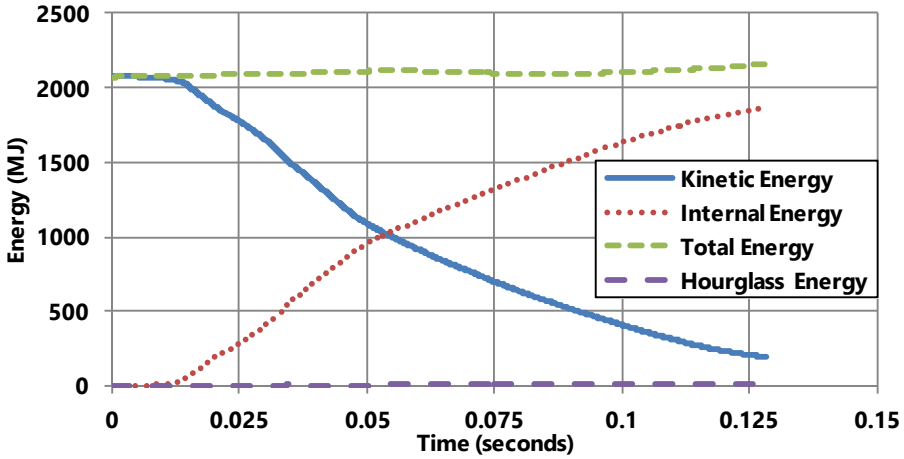

b) 80 km/h impact velocity

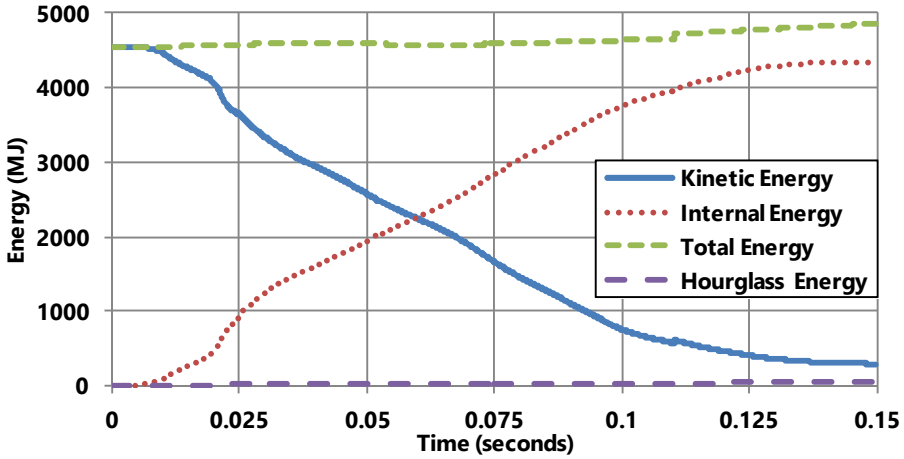

c) 120 km/h impact velocity

Figure A.4. Energy distribution for the 900 mm diameter pier with 50 mm hoop spacing at different impact velocities

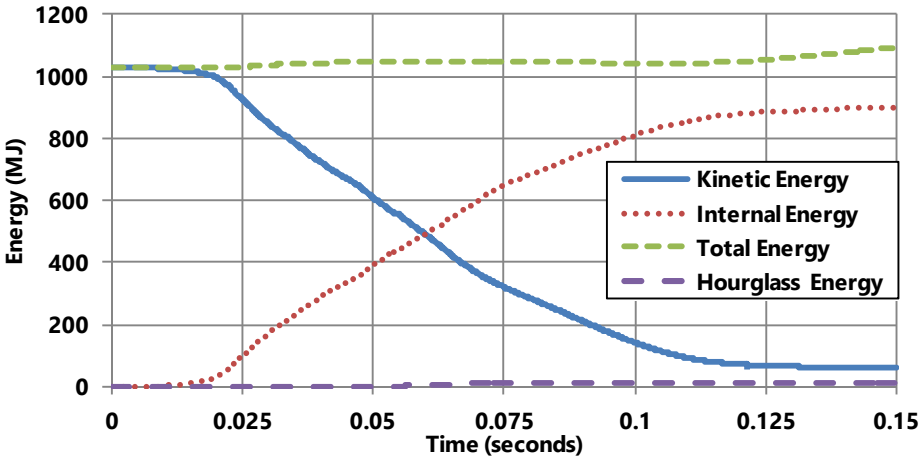

a) 55 km/h impact velocity

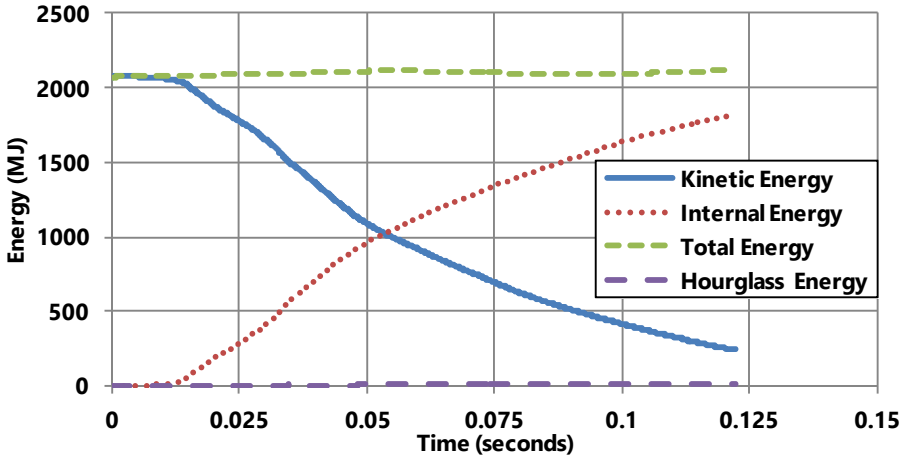

b) 80 km/h impact velocity

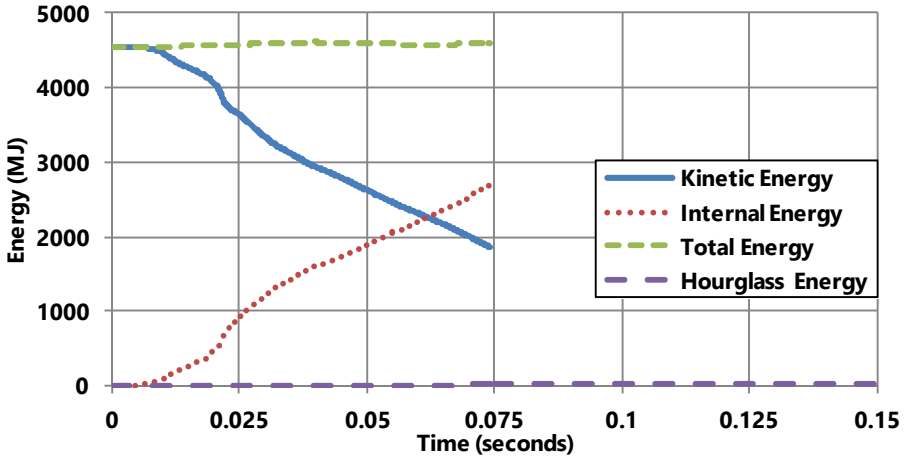

c) 120 km/h impact velocity

Figure A.5. Energy distribution for the 900 mm diameter pier with 150 mm hoop spacing at different impact velocities

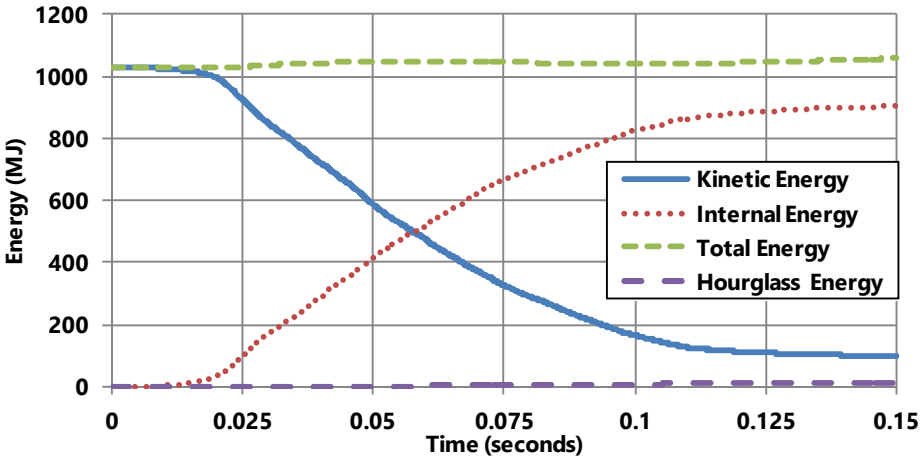

a) 55 km/h impact velocity

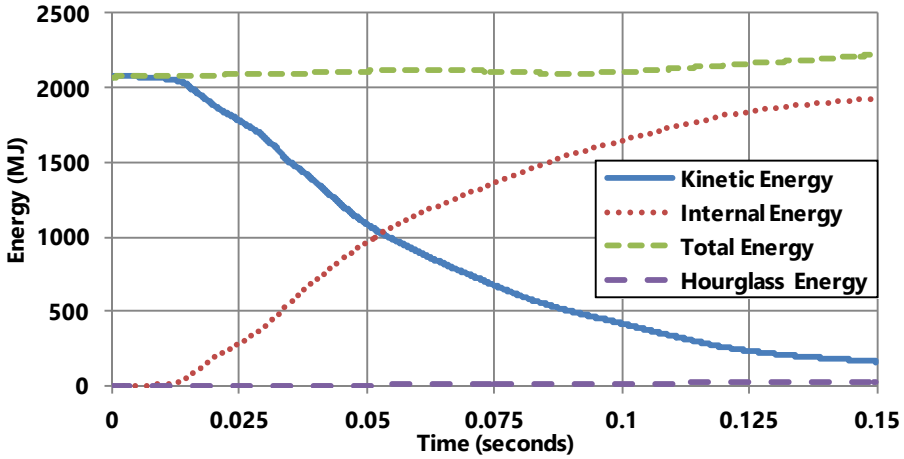

b) 80 km/h impact velocity

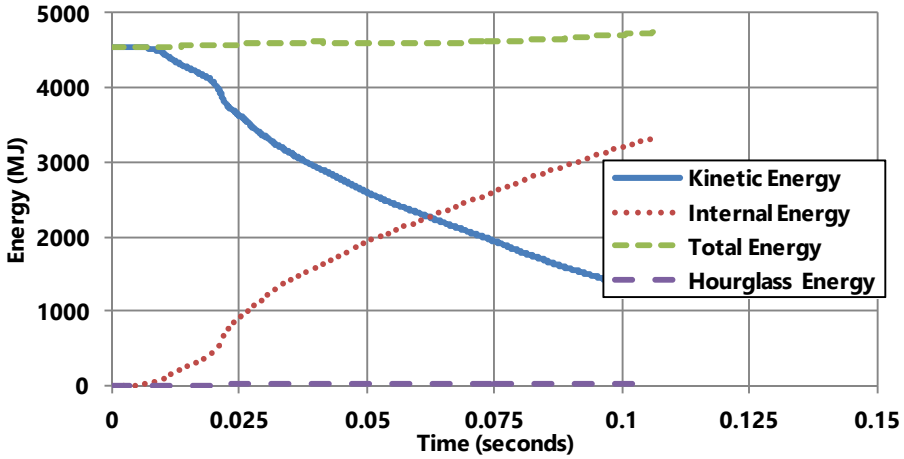

c) 120 km/h impact velocity

Figure A.6. Energy distribution for the 900 mm diameter pier with 300 mm hoop spacing at different impact velocities

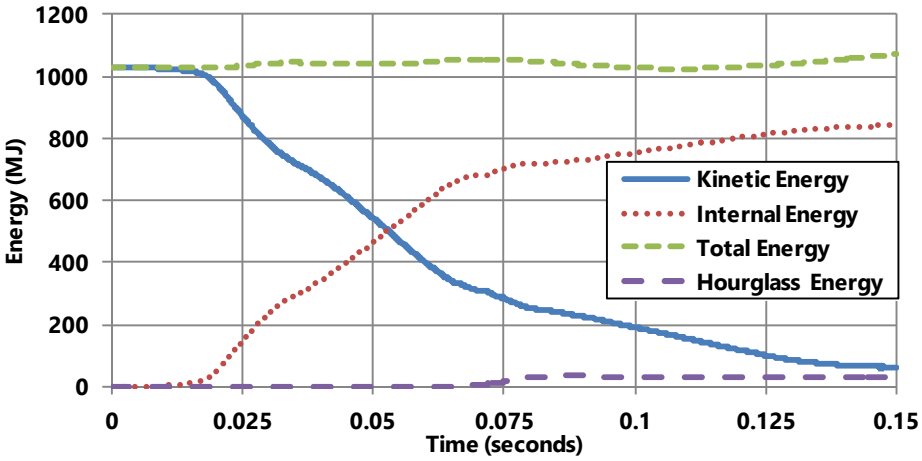

a) 55 km/h impact velocity

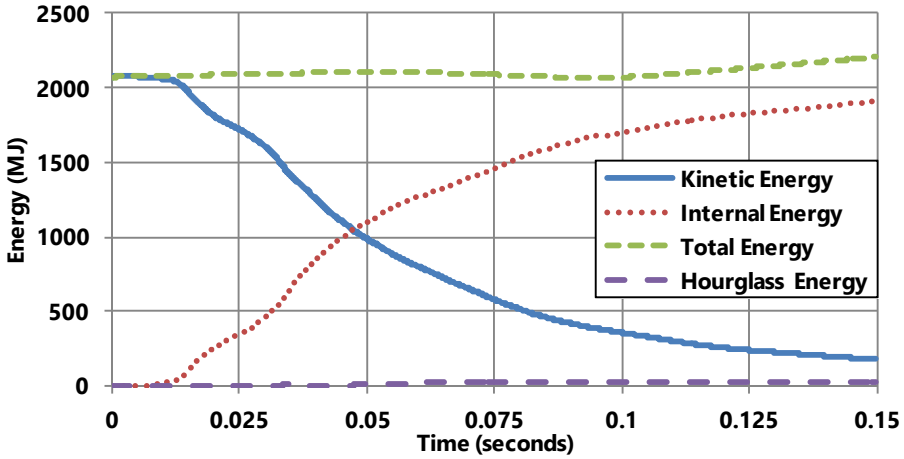

b) 80 km/h impact velocity

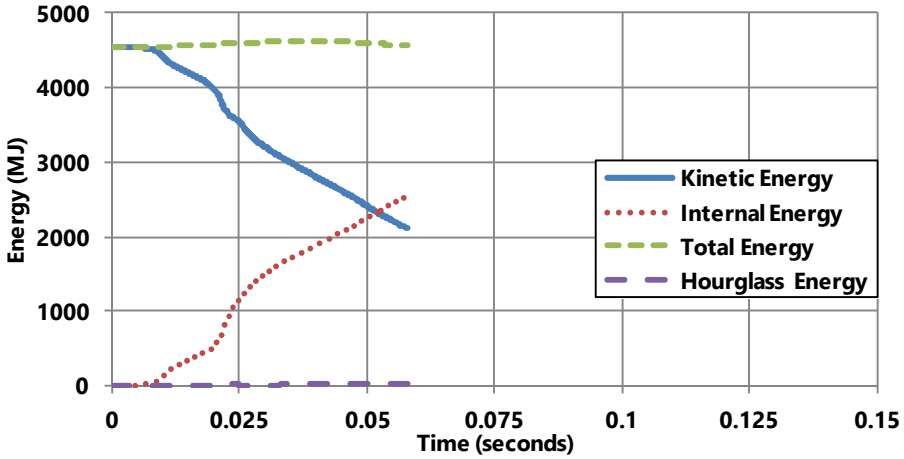

c) 120 km/h impact velocity

Figure A.7. Energy distribution for the 1,200 mm diameter pier with 50 mm hoop spacing at different impact velocities

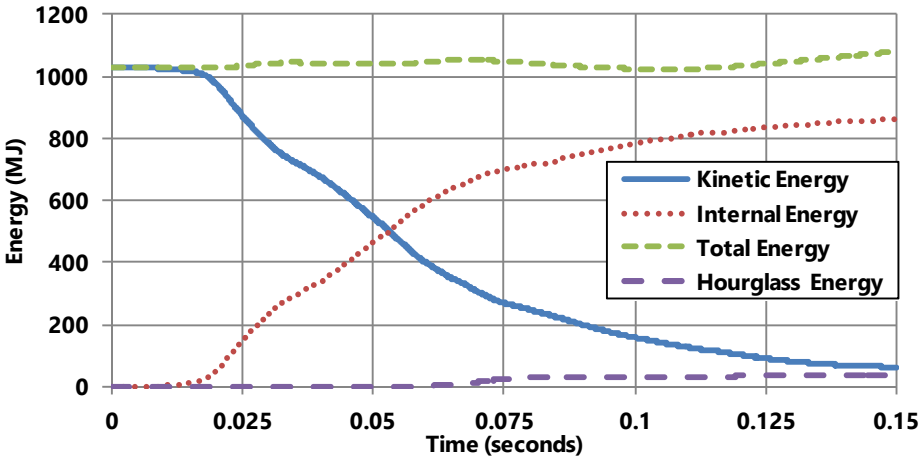

a) 55 km/h impact velocity

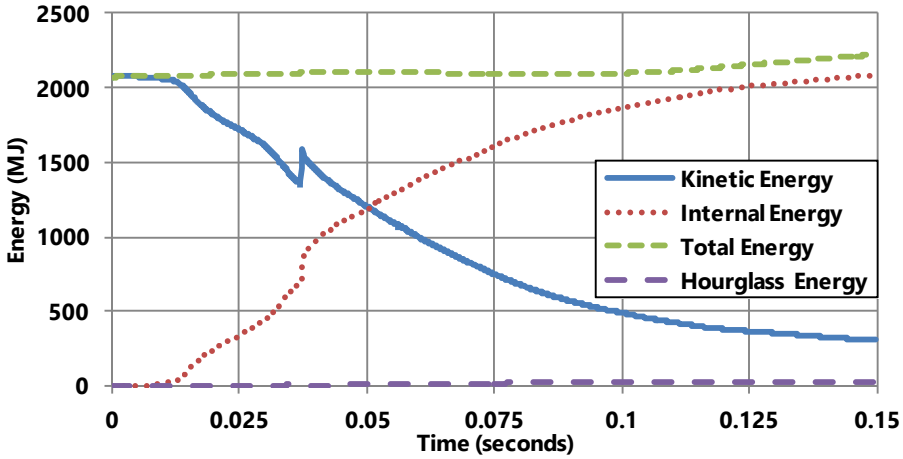

b) 80 km/h impact velocity

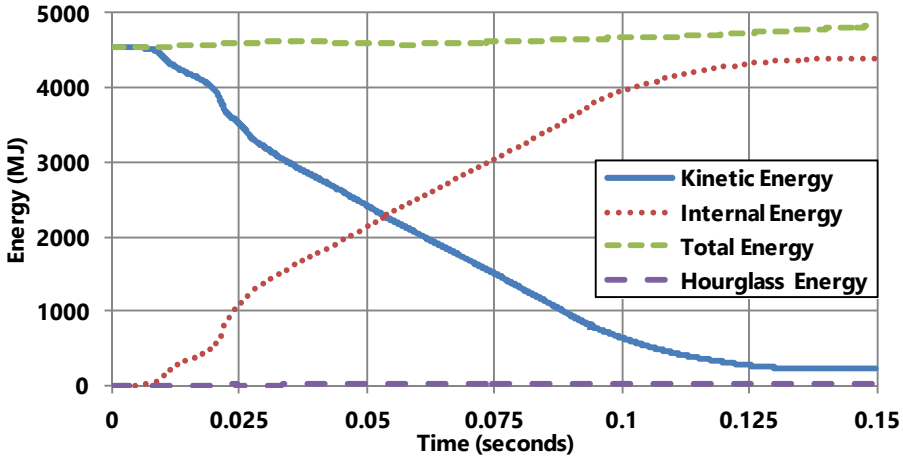

c) 120 km/h impact velocity

Figure A.8. Energy distribution for the 1,200 mm diameter pier with 150 mm hoop spacing at different impact velocities

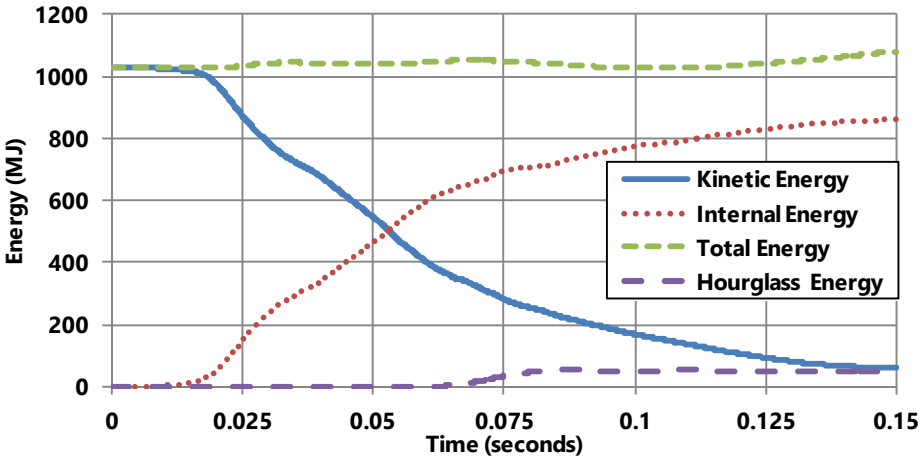

a) 55 km/h impact velocity

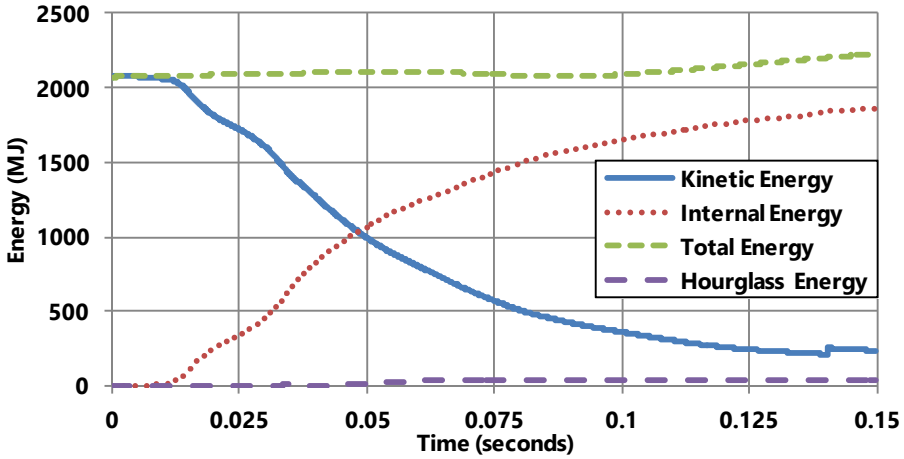

b) 80 km/h impact velocity

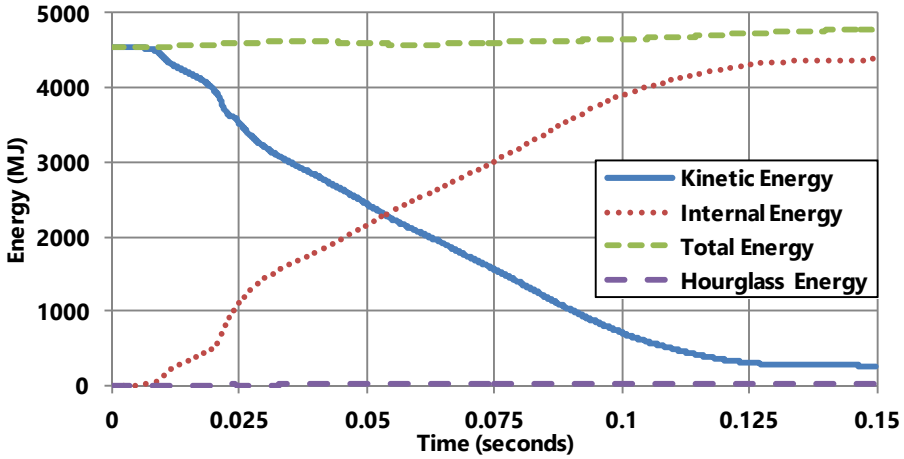

c) 120 km/h impact velocity

Figure A.9. Energy distribution for the 1,200 mm diameter pier with 300 mm hoop spacing at different impact velocities

APPENDIX B.

RESULTANT IMPACT FORCE TIME HISTORIES

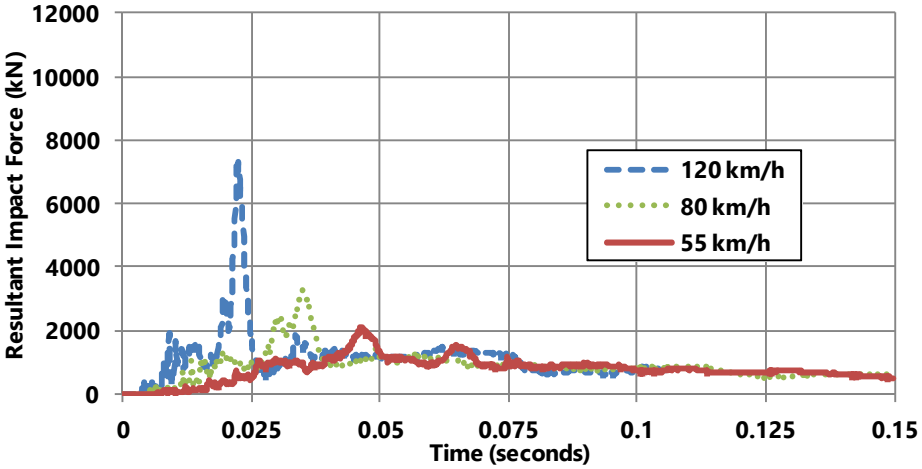

a) 50 mm hoop spacing

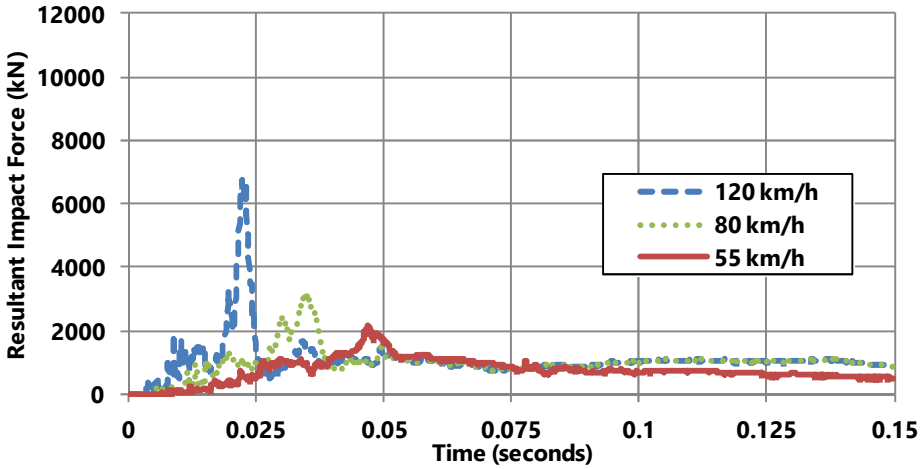

b) 150 mm hoop spacing

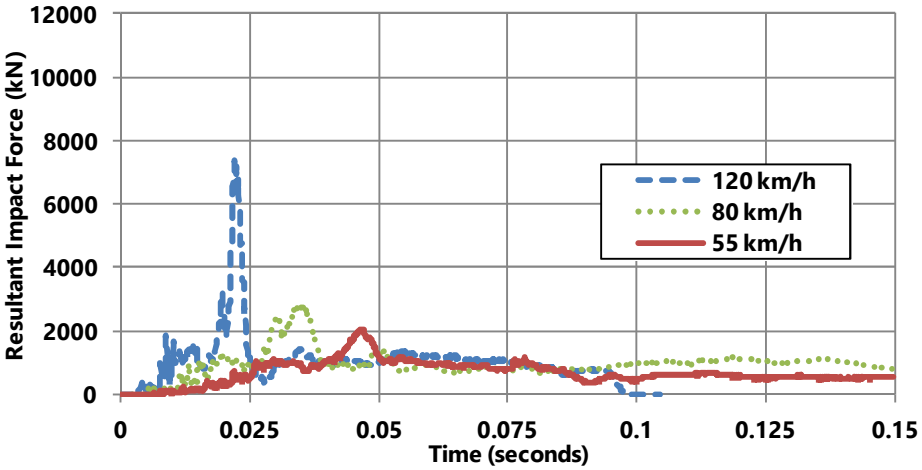

c) 300 mm hoop spacing

Figure B.10. Resultant impact force time histories for the 600 mm diameter piers with different hoop spacing

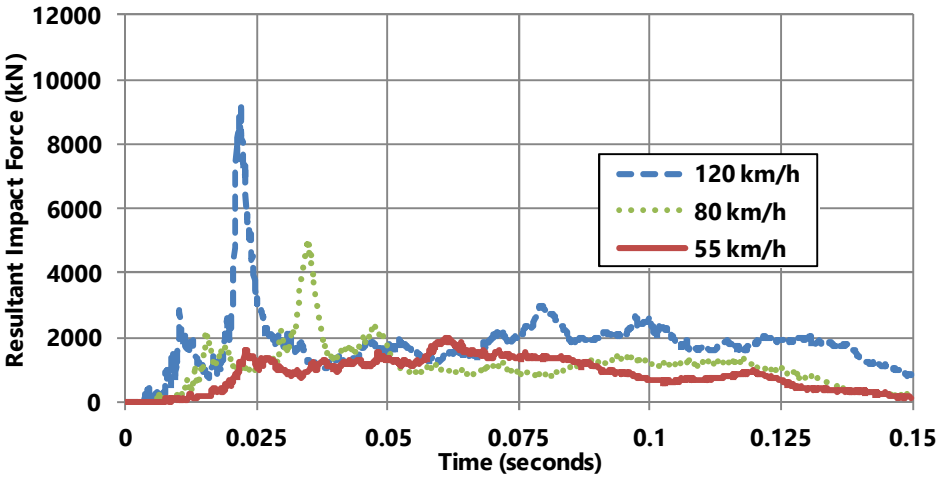

a) 50 mm hoop spacing

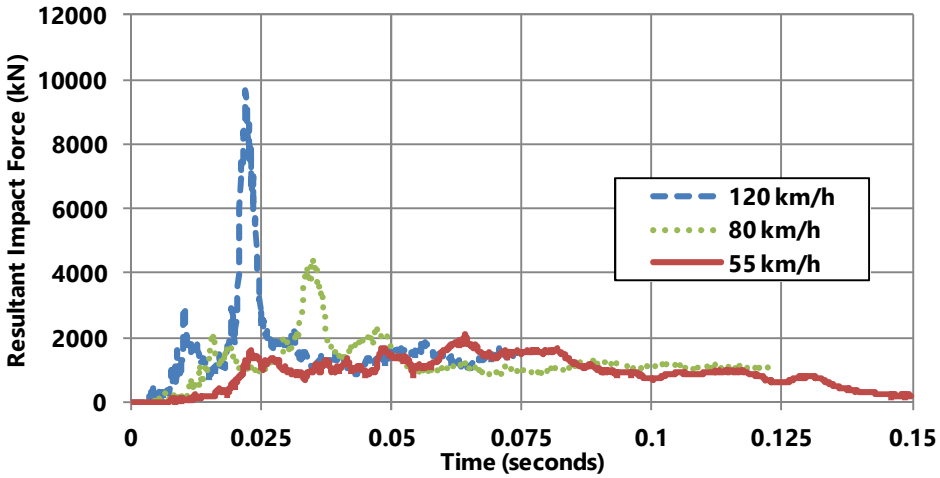

b) 150 mm hoop spacing

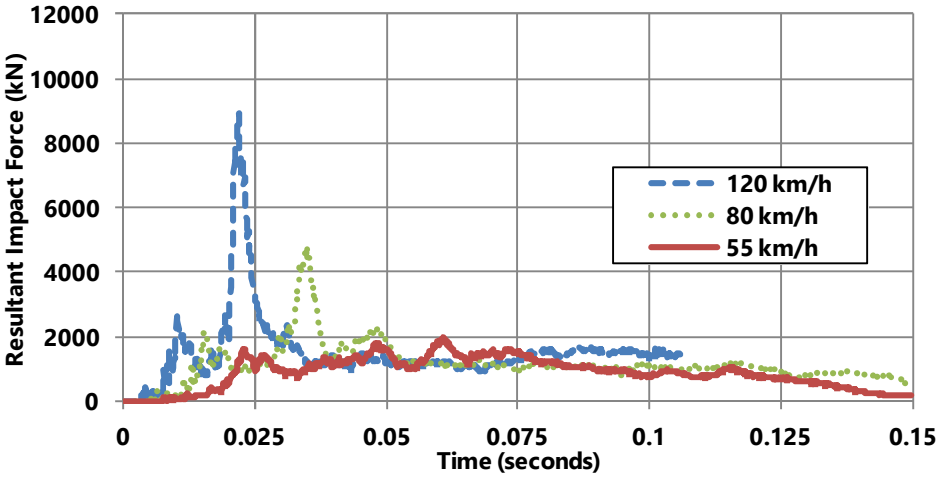

c) 300 mm hoop spacing

Figure B.2. Resultant impact force time histories for the 900 mm diameter piers with different hoop spacing

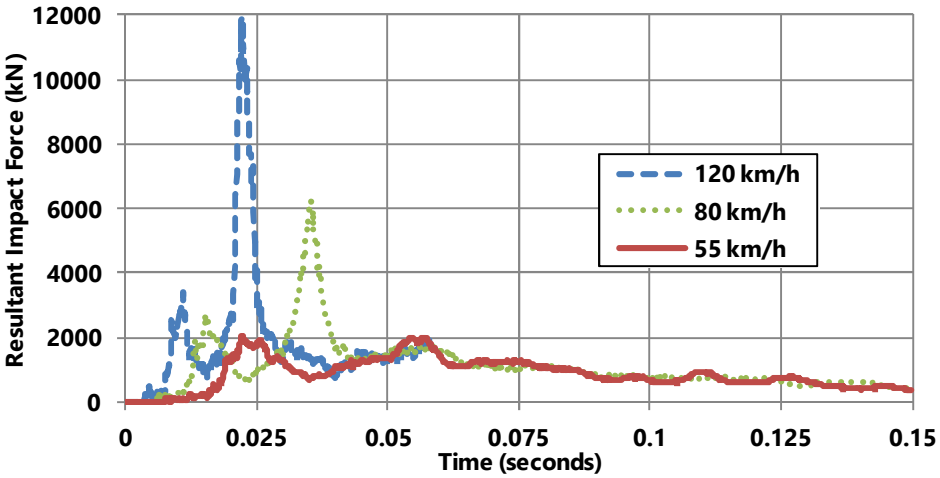

a) 50 mm hoop spacing

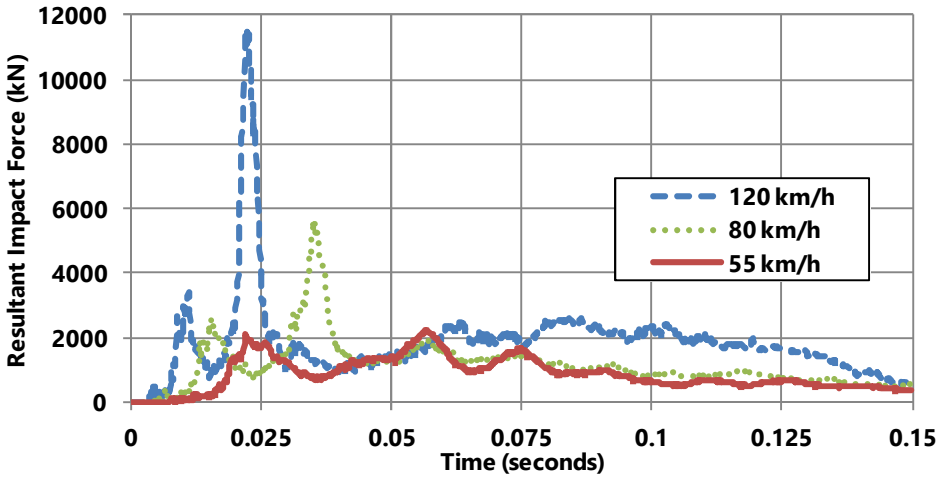

b) 150 mm hoop spacing

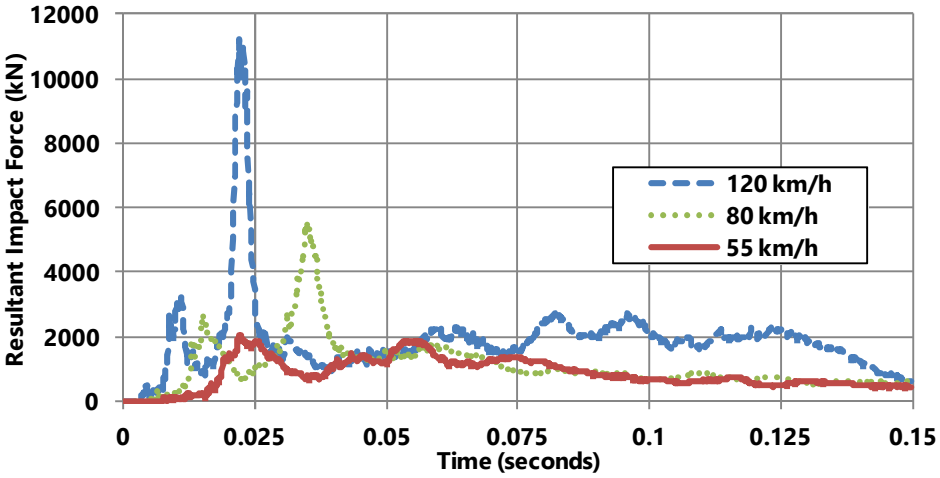

c) 300 mm hoop spacing

Figure B.3. Resultant impact force time histories for the 1,200 mm diameter piers with different hoop spacing

APPENDIX C.

LATERAL DISPLACEMENT AT TIME OF PEAK IMPACT FORCE

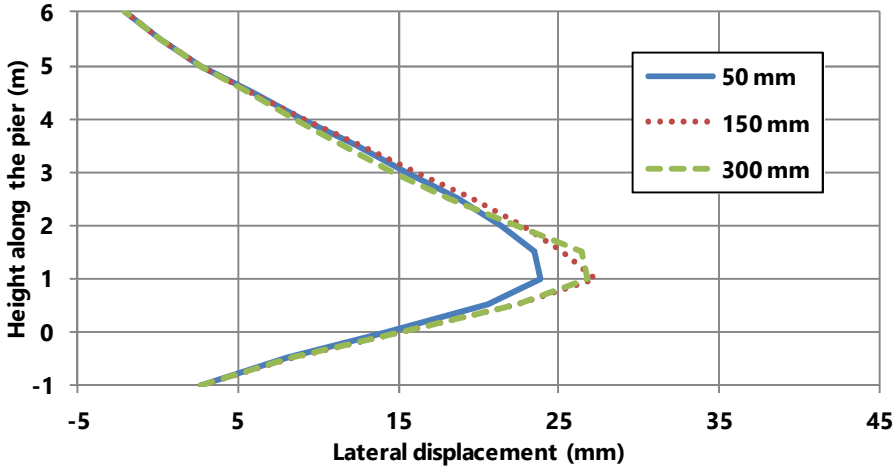

a) 55 km/h impact velocity

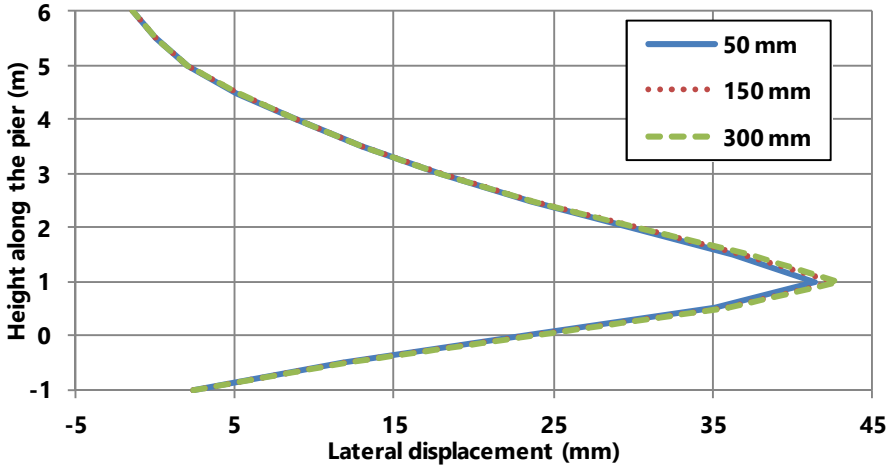

b) 80 km/h impact velocity

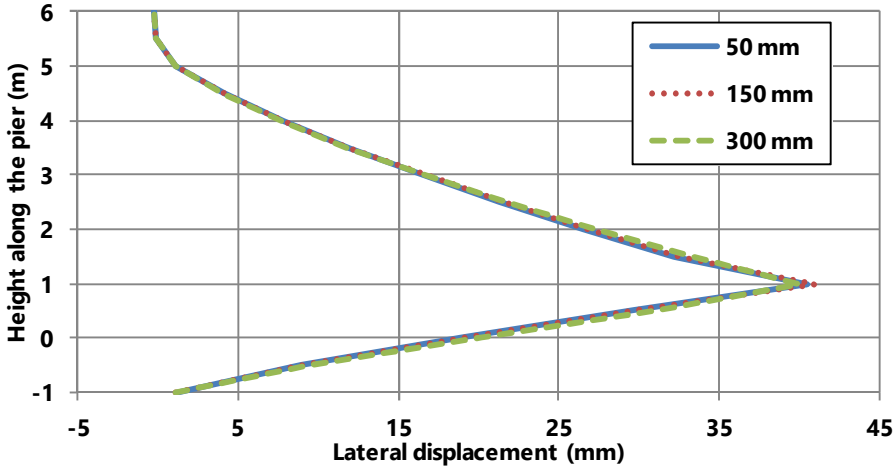

c) 120 km/h impact velocity

Figure C.11. Lateral displacement along the length of the 600 mm diameter piers at different impact velocities

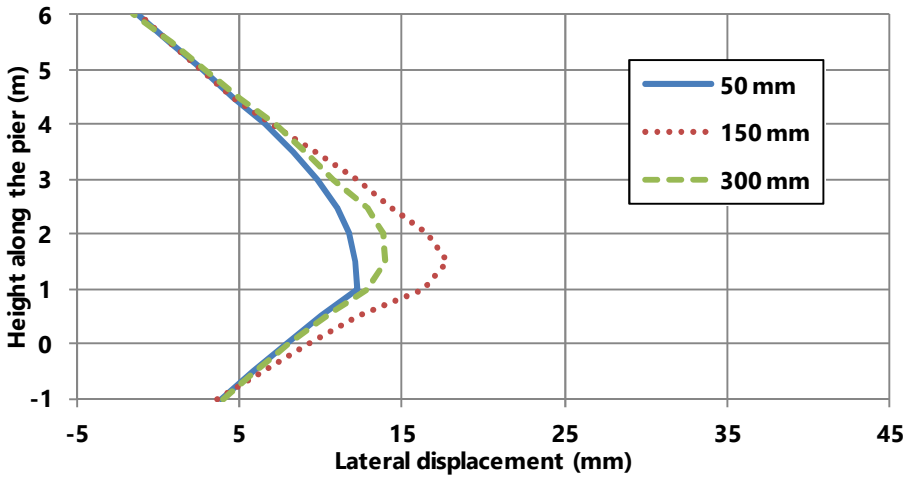

a) 55 km/h impact velocity

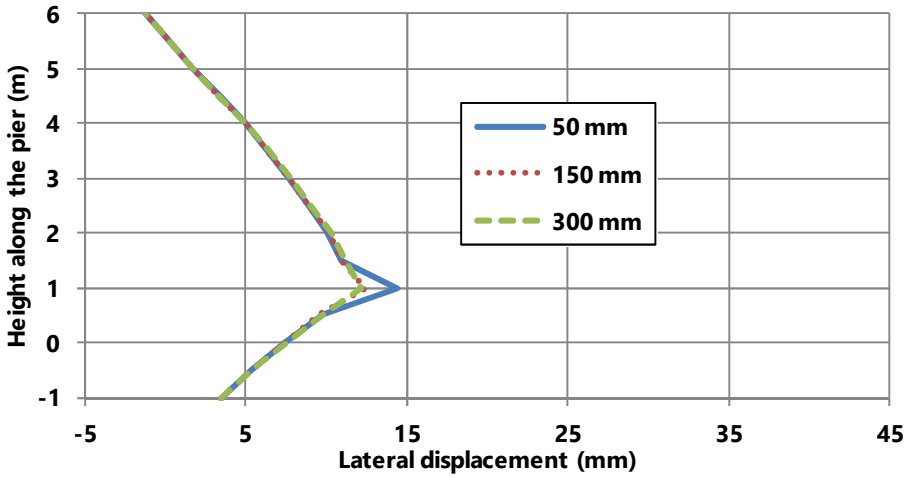

b) 80 km/h impact velocity

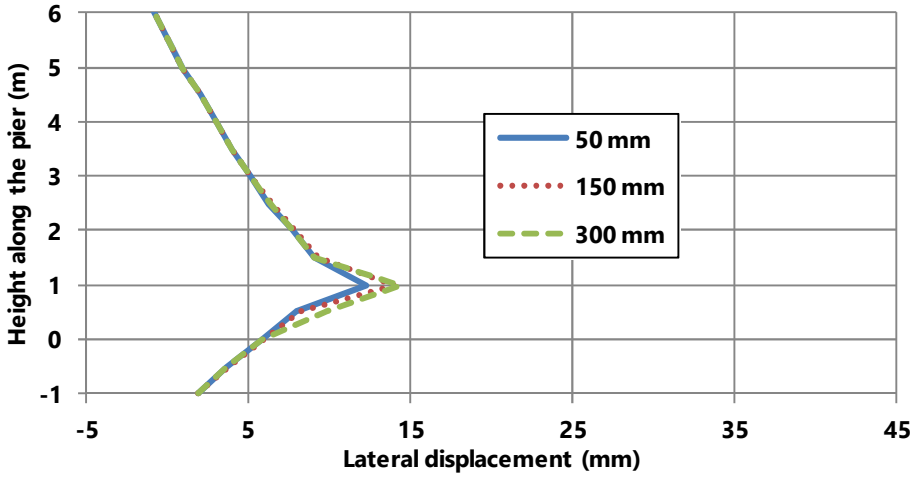

c) 120 km/h impact velocity

Figure C.2. Lateral displacement along the length of the 900 mm diameter piers at different impact velocities

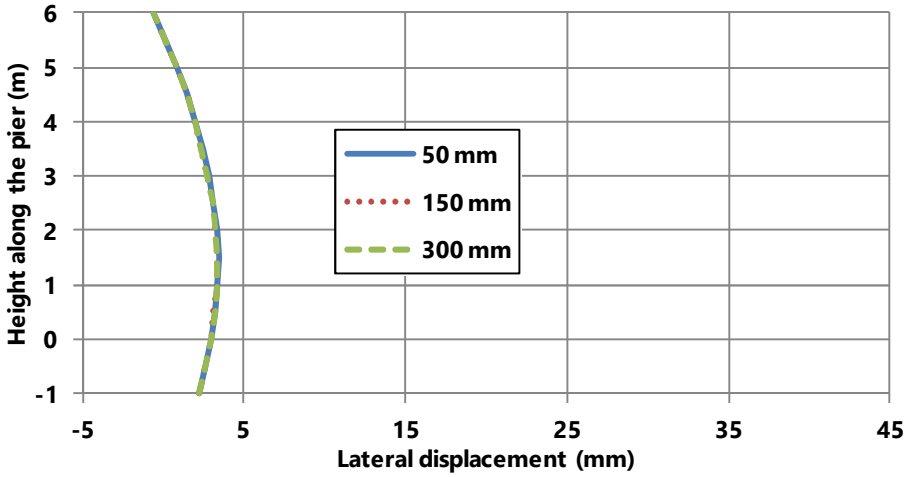

a) 55 km/h impact velocity

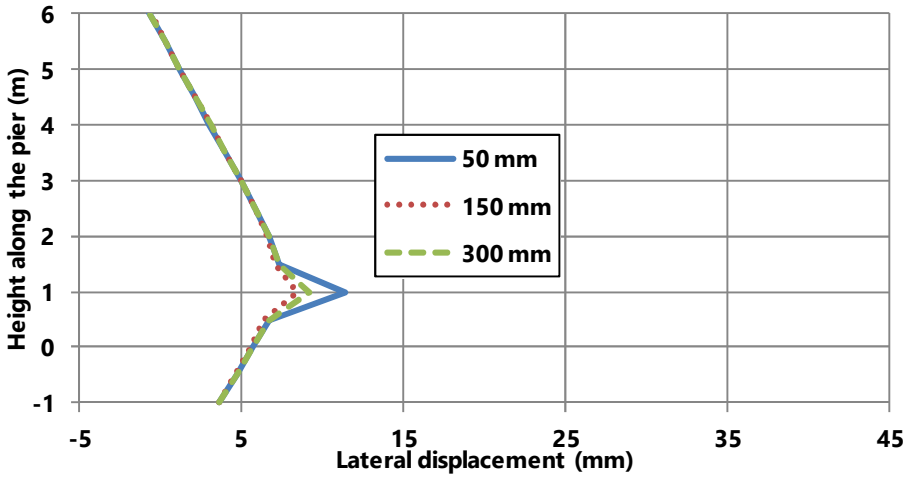

b) 80 km/h impact velocity

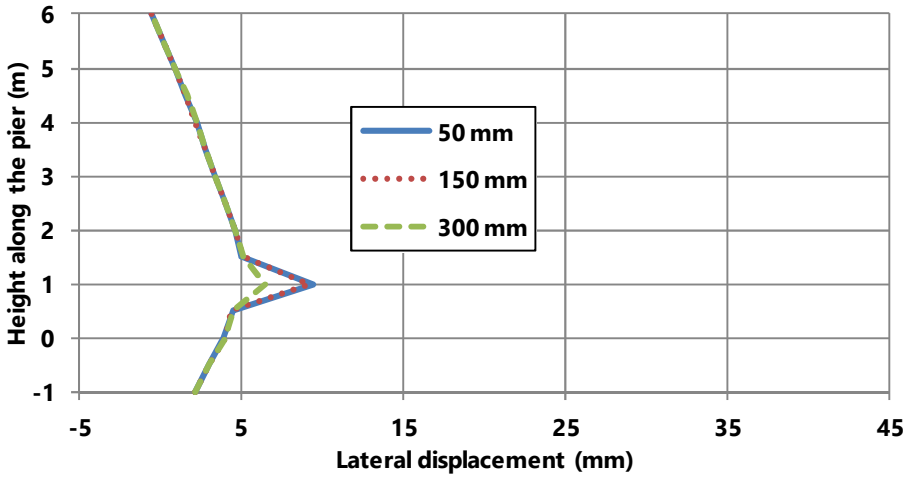

c) 120 km/h impact velocity

Figure C.3. Lateral displacement along the length of the 1,200 mm diameter piers at different impact velocities

APPENDIX D.

SHEAR AT TIME OF PEAK IMPACT FORCE

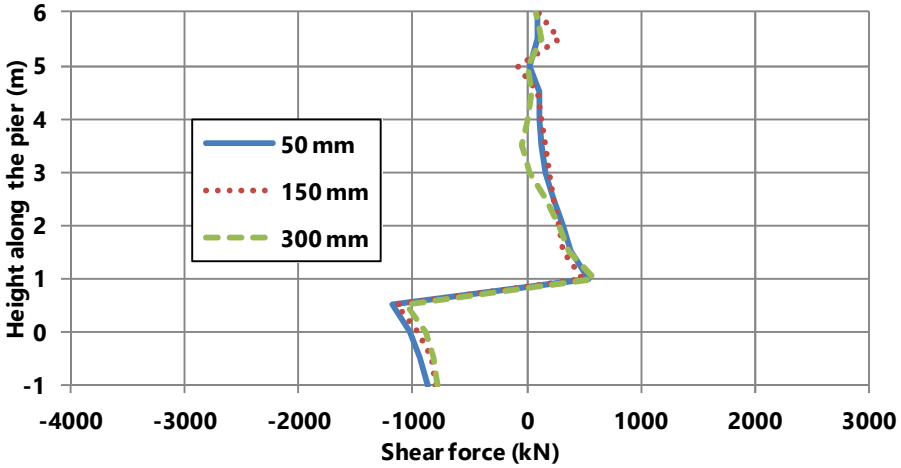

a) 55 km/h impact velocity

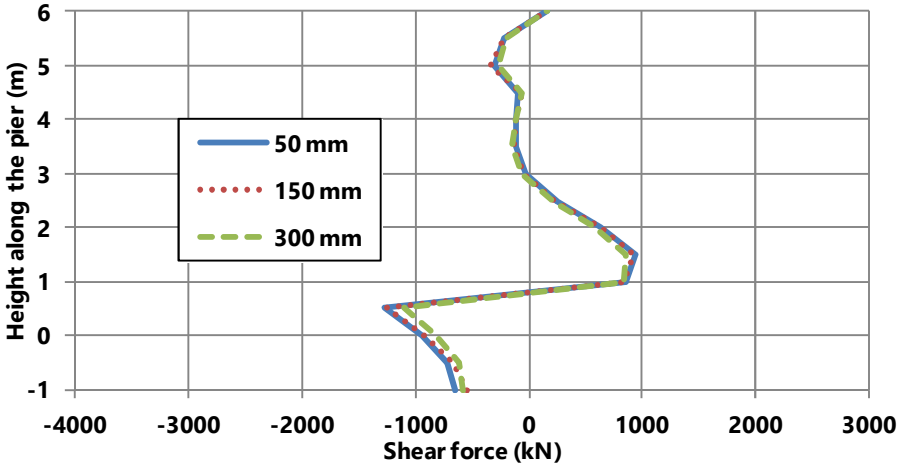

b) 80 km/h impact velocity

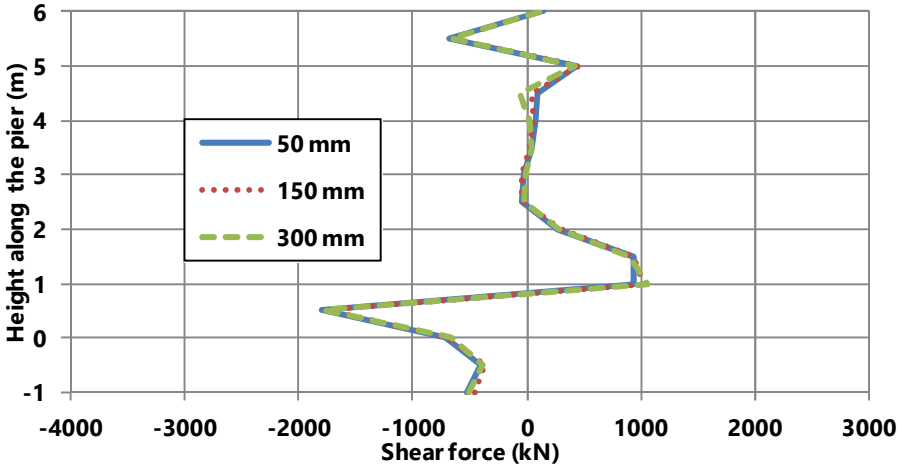

c) 120 km/h impact velocity

Figure D.1. Shear along the length of the 600 mm diameter piers at different impact velocities

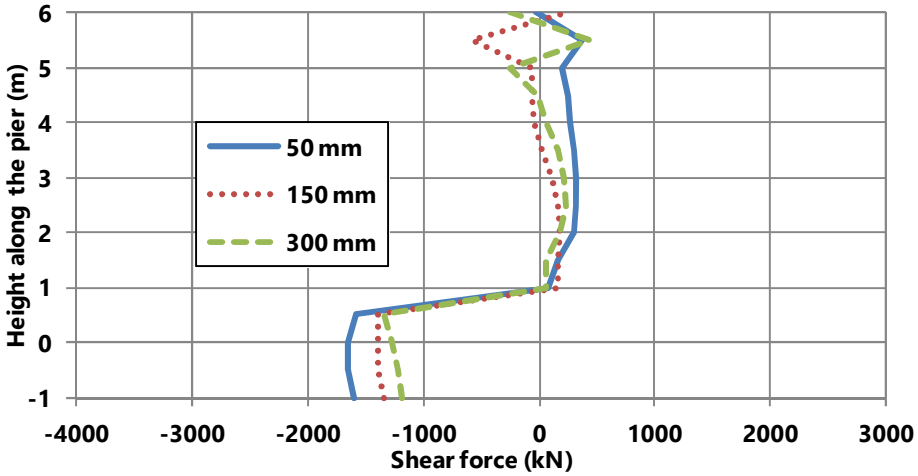

a) 55 km/h impact velocity

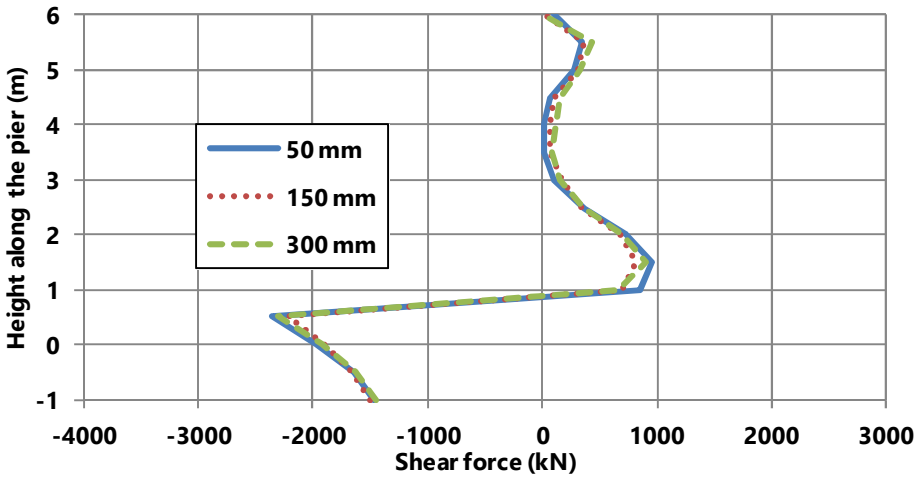

b) 80 km/h impact velocity

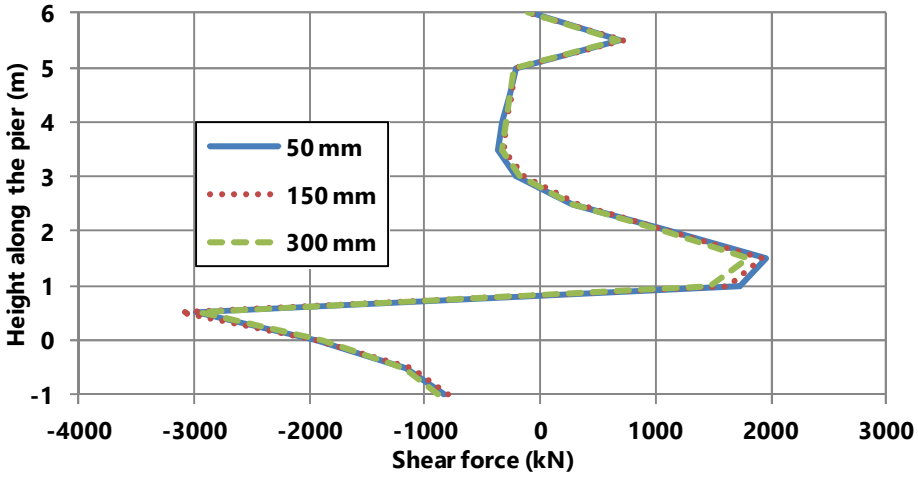

c) 120 km/h impact velocity

Figure D.2. Shear along the length of the 900 mm diameter piers at different impact velocities

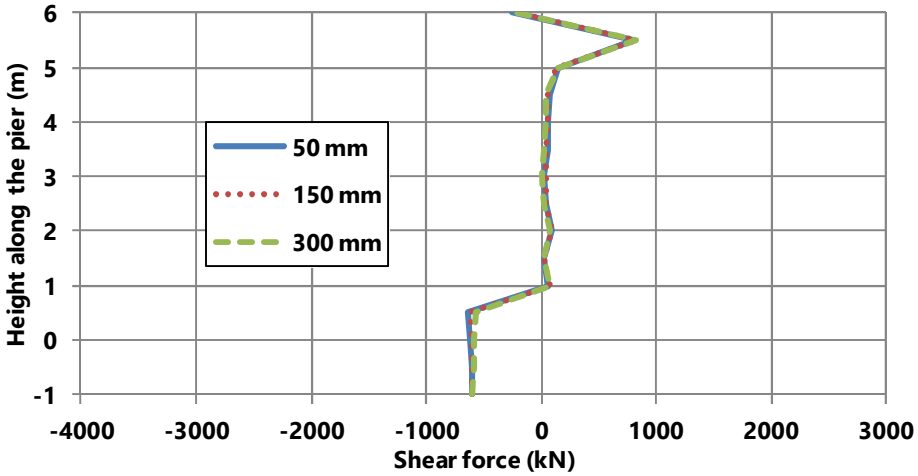

a) 55 km/h impact velocity

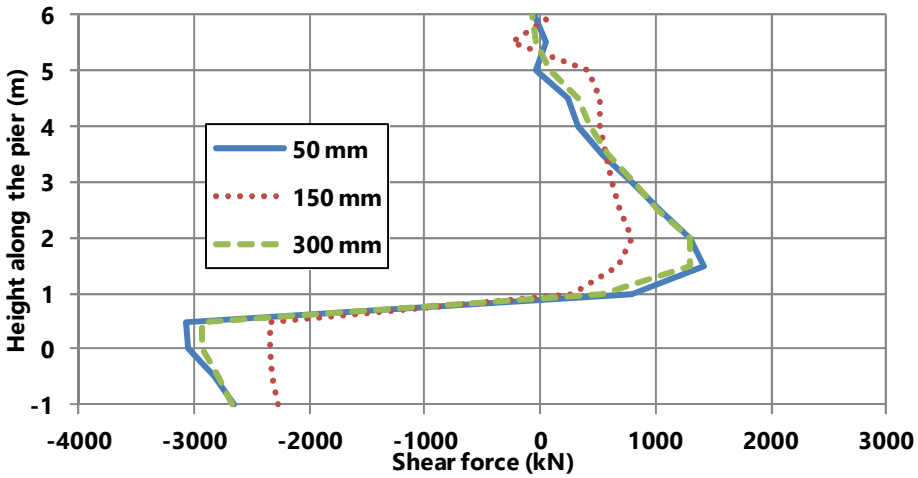

b) 80 km/h impact velocity

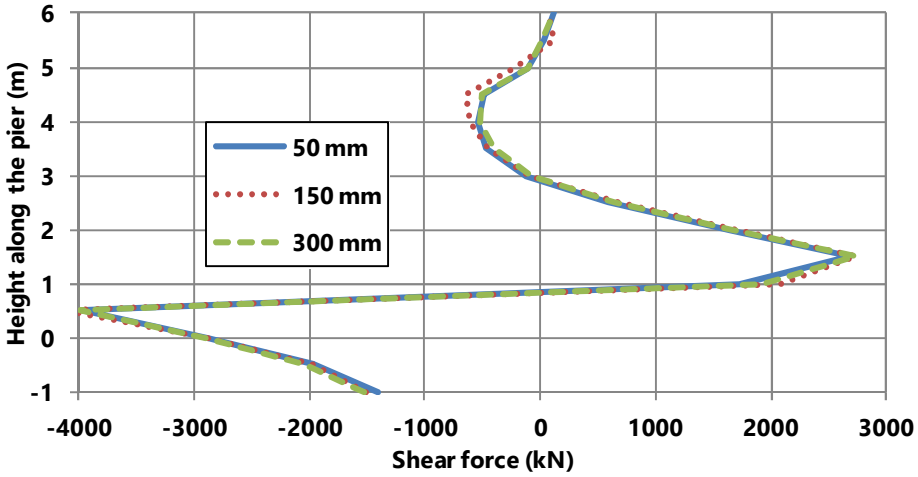

c) 120 km/h impact velocity

Figure D.3. Shear along the length of the 1,200 mm diameter piers at different impact velocities

APPENDIX E.

MOMENT AT TIME OF PEAK IMPACT FORCE

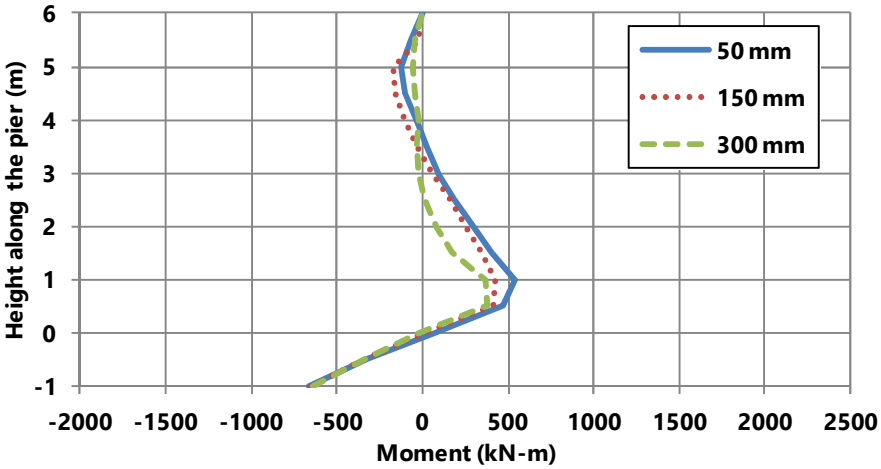

a) 55 km/h impact velocity

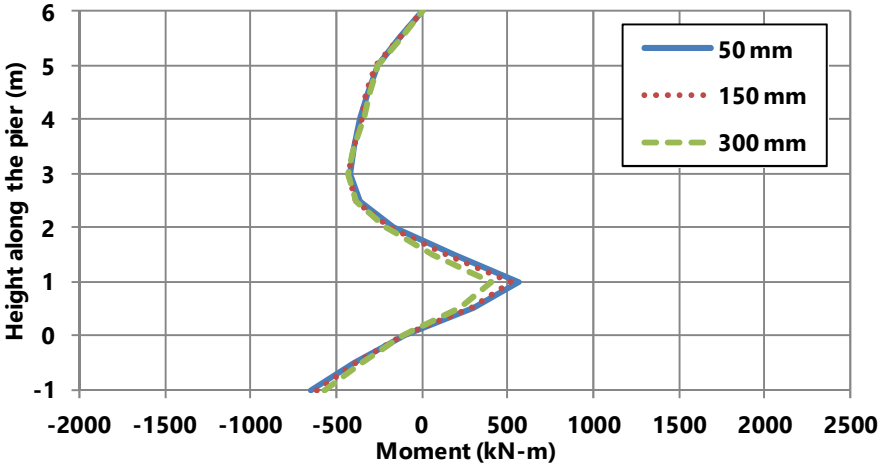

b) 80 km/h impact velocity

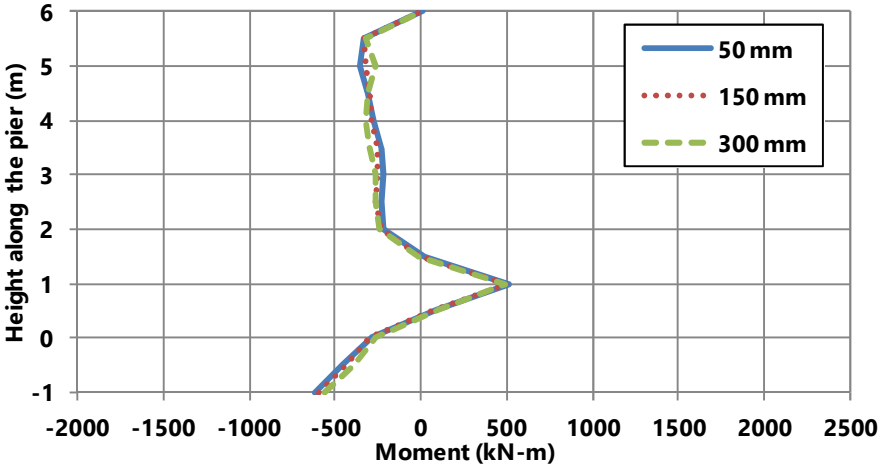

c) 120 km/h impact velocity

Figure E.1. Moments along the length of the 600 mm diameter piers at different impact velocities

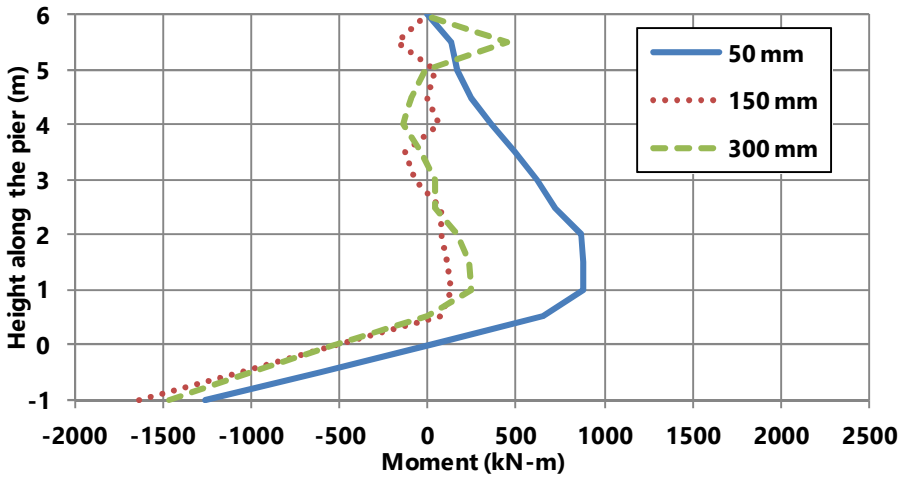

a) 55 km/h impact velocity

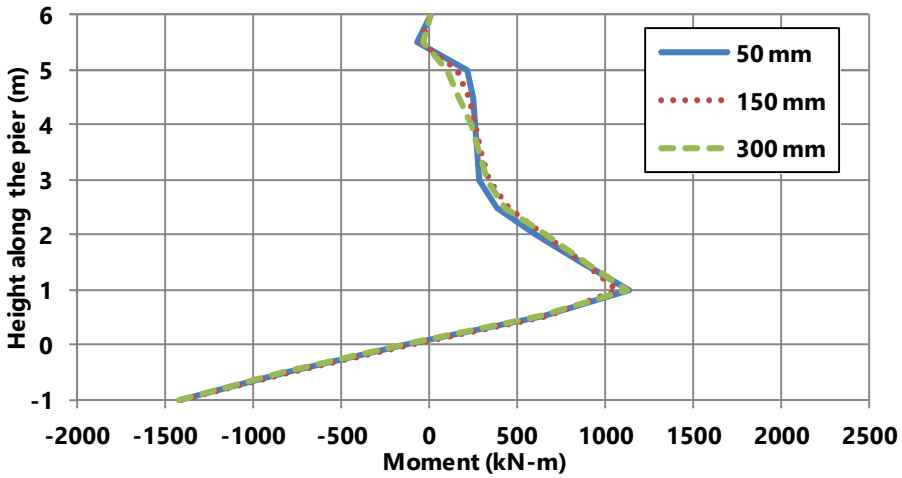

b) 80 km/h impact velocity

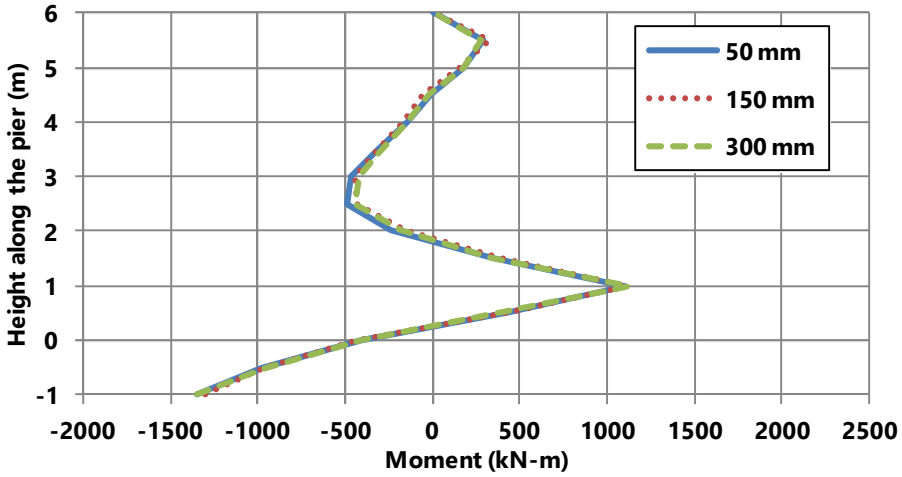

c) 120 km/h impact velocity

Figure E.2. Moments along the length of the 900 mm diameter piers at different impact velocities

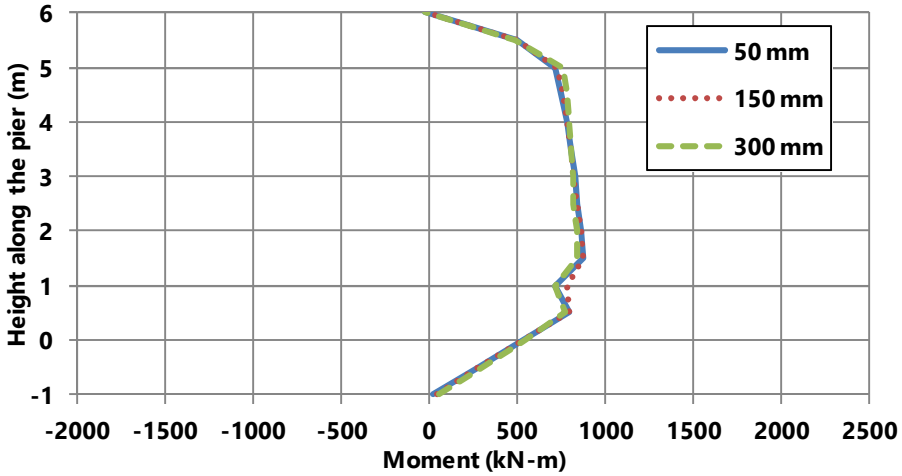

a) 55 km/h impact velocity

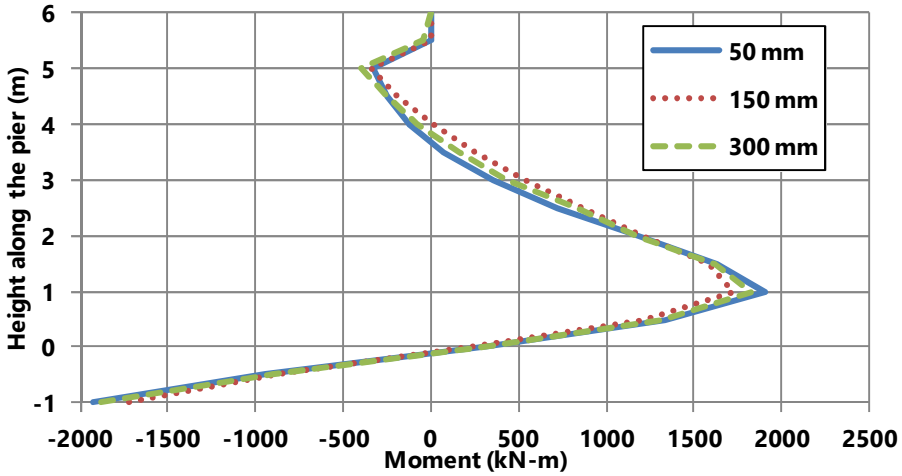

b) 80 km/h impact velocity

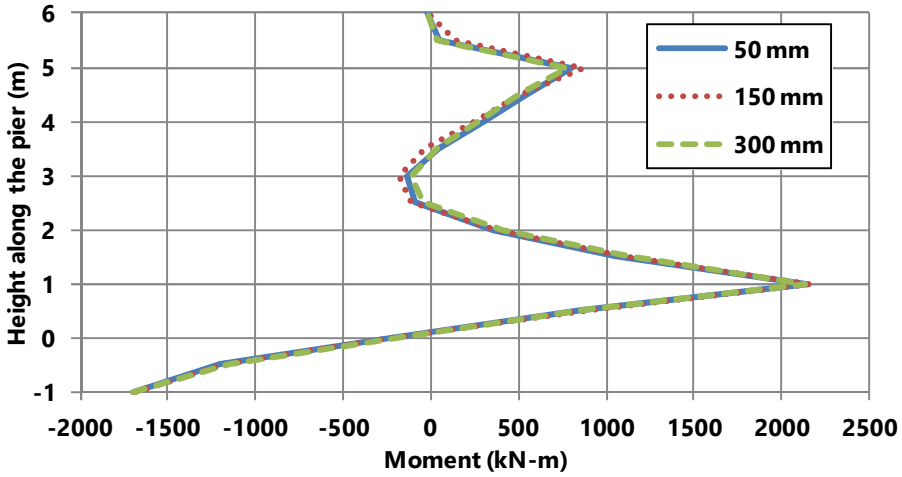

c) 120 km/h impact velocity

Figure E.3. Moments along the length of the 1,200 mm diameter piers at different impact velocities

APPENDIX F.

DISPLACEMENT, SHEAR, AND MOMENT TIME HISTORIES

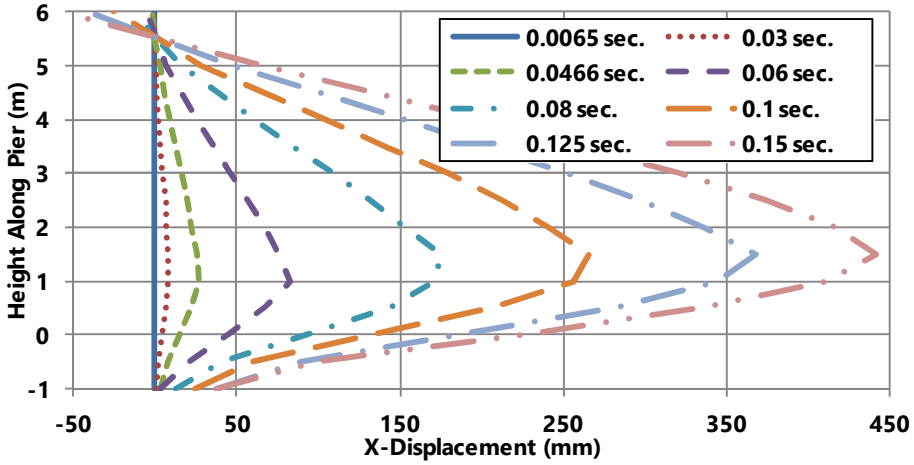

a) Lateral displacement along pier

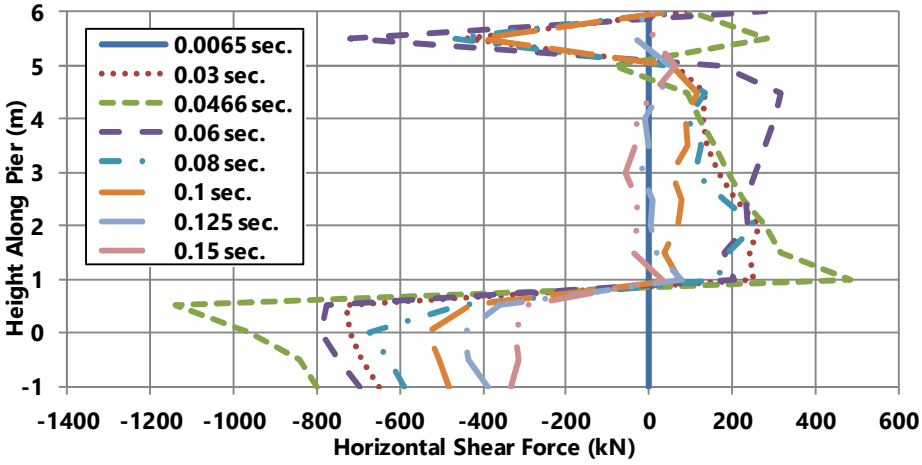

b) Shear along the pier

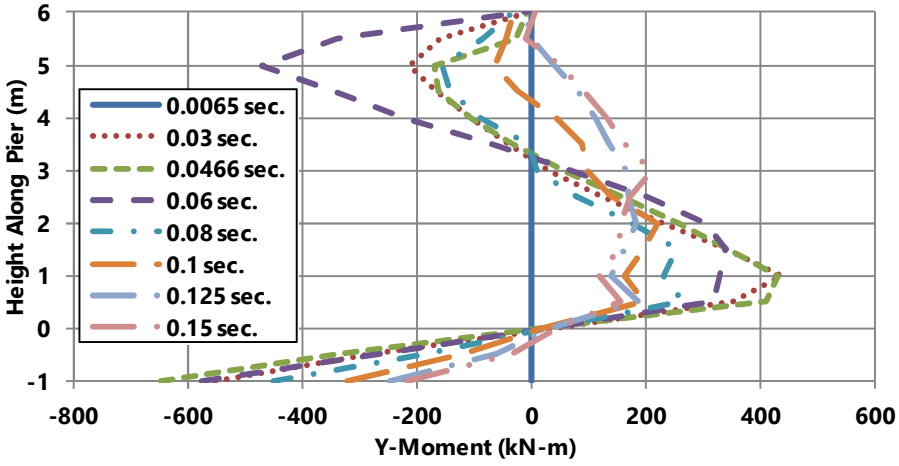

c) Moment along the pier

Figure F.1. Displacement, shear, and moment along the length of the 600 mm dia. pier with 150 mm hoop spacing at an impact velocity of 55 km/h at different time steps

APPENDIX G.

AXIAL FORCE IN LONGITUDINAL REINFORCEMENT

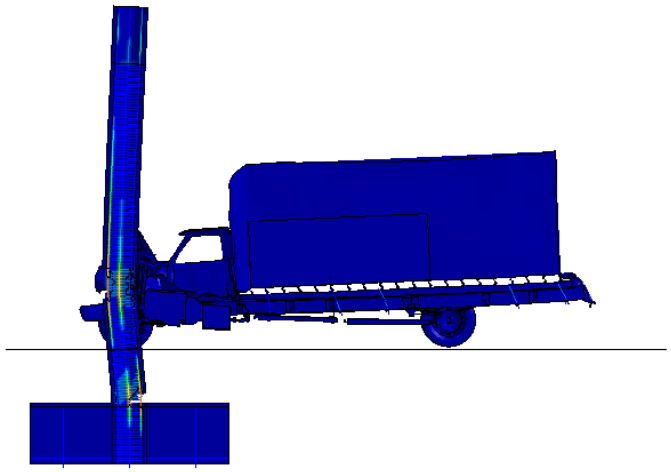

a) 55 km/h impact velocity

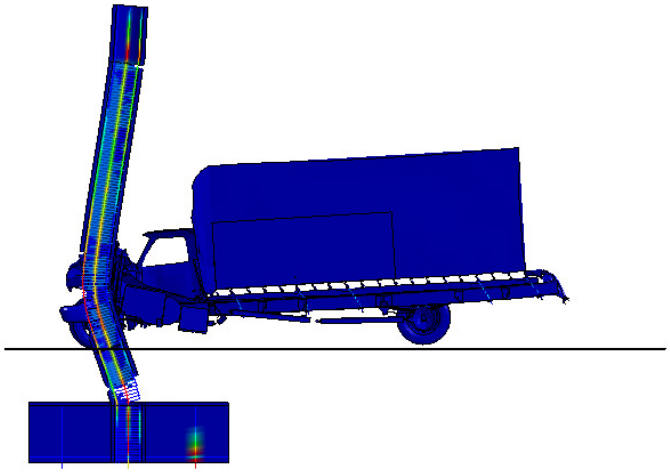

b) 80 km/h impact velocity

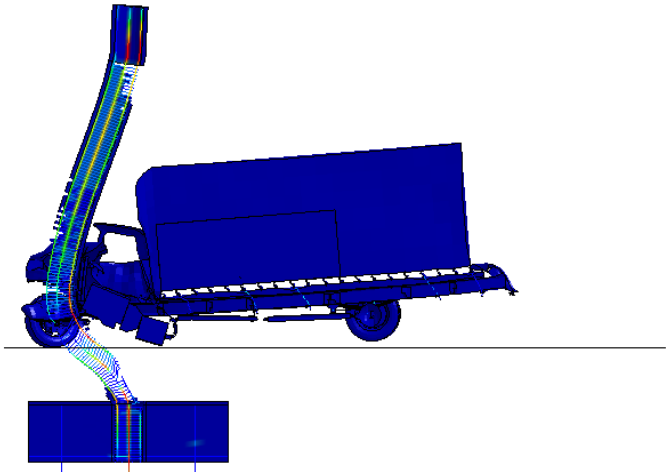

a) 120 km/h impact velocity

Figure G.1. Axial force in the longitudinal bars for the 600 mm diameter pier with 50 mm hoop spacing at 100 ms

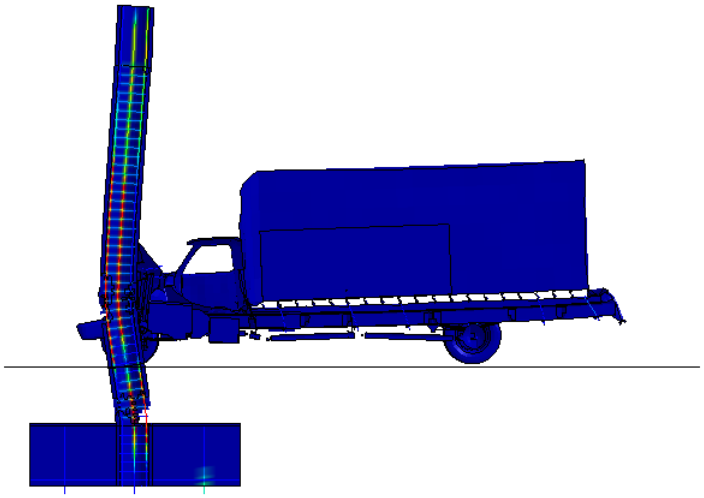

a) 55 km/h impact velocity

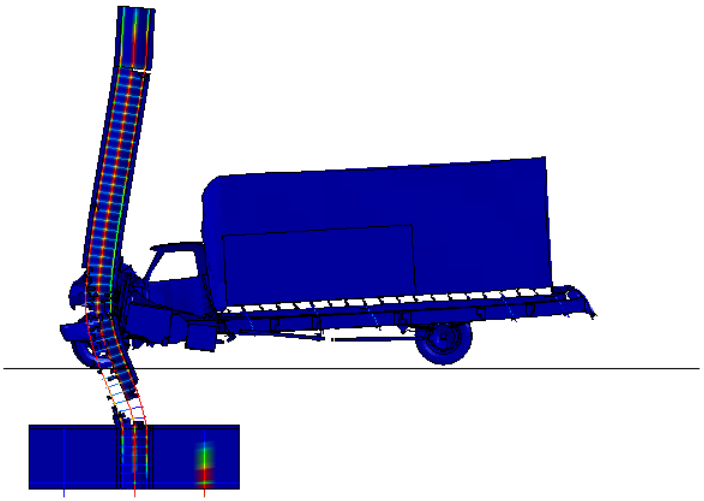

b) 80 km/h impact velocity

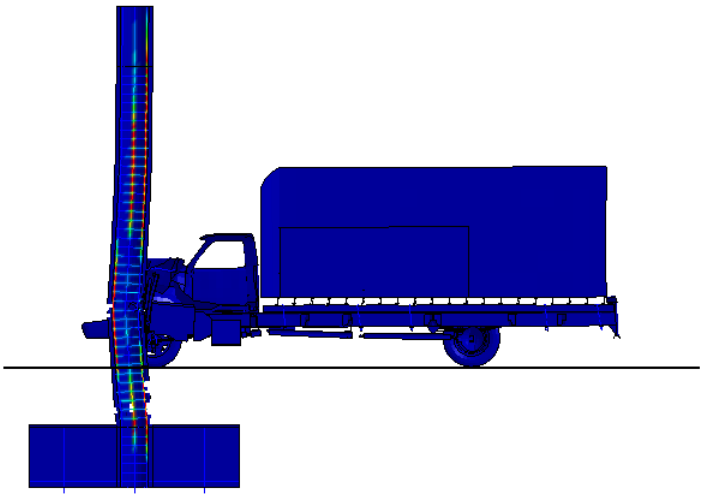

c) 120 km/h impact velocity

Figure G.2. Axial force in the longitudinal bars for the 600 mm diameter pier with 150 mm hoop spacing at 100 ms

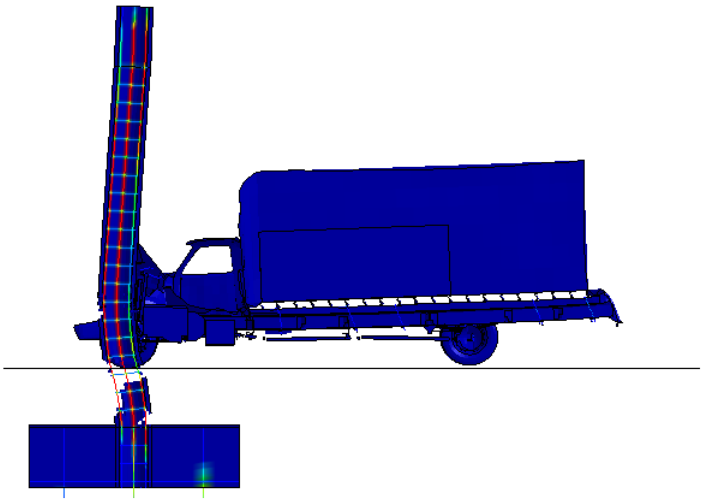

a) 55 km/h impact velocity

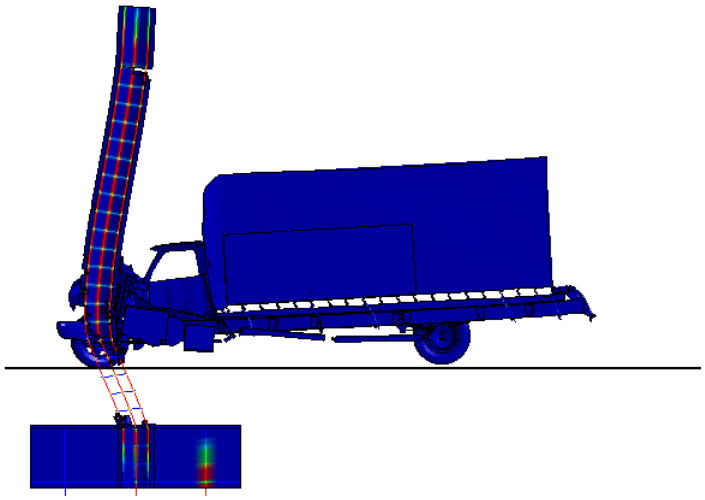

b) 80 km/h impact velocity

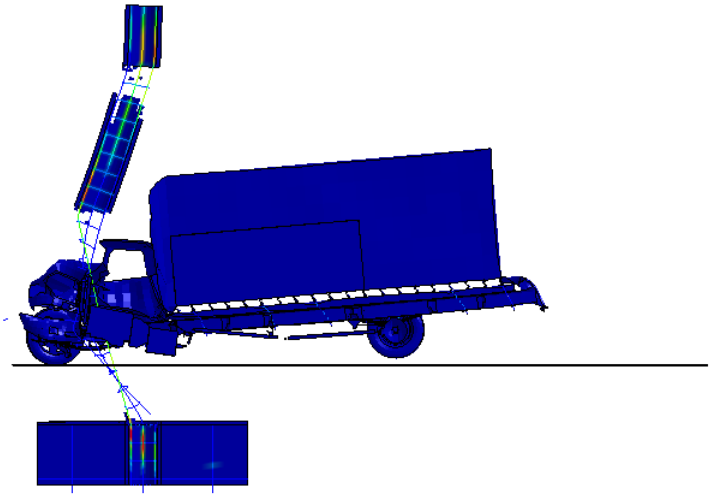

c) 120 km/h impact velocity

Figure G.3 Axial force in the longitudinal bars for the 600 mm diameter pier with 300 mm hoop spacing at 100 ms

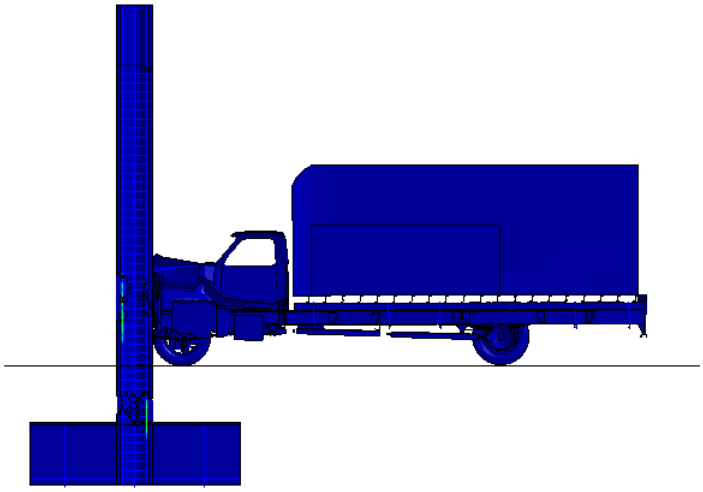

a) 30 ms after impact

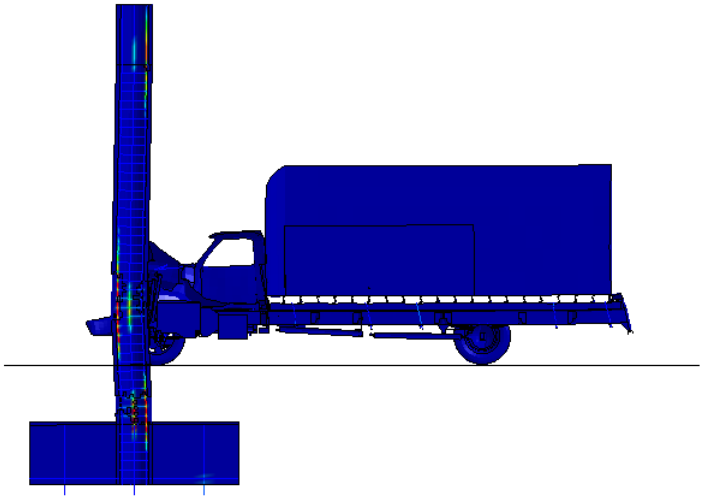

b) 60 ms after impact

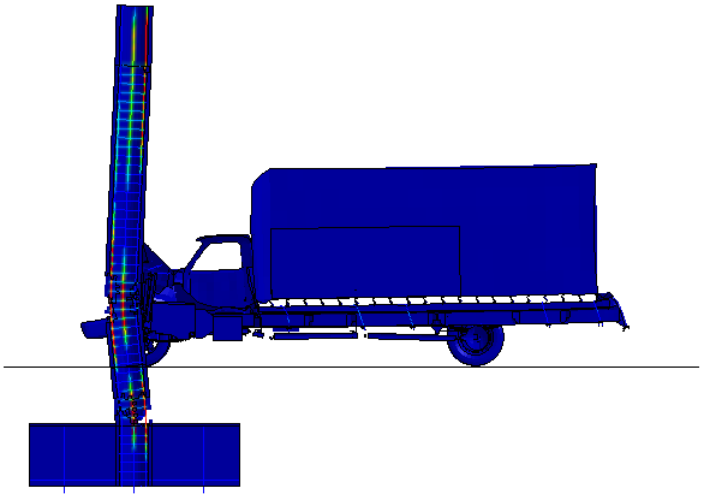

c) 80 ms after impact

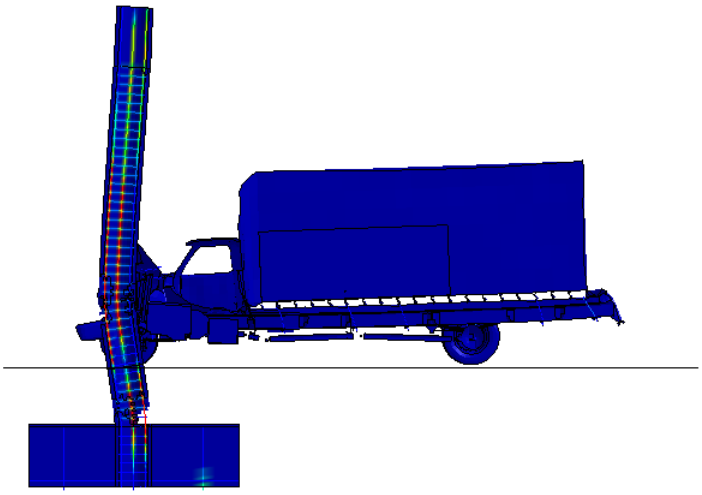

d) 100 ms after impact

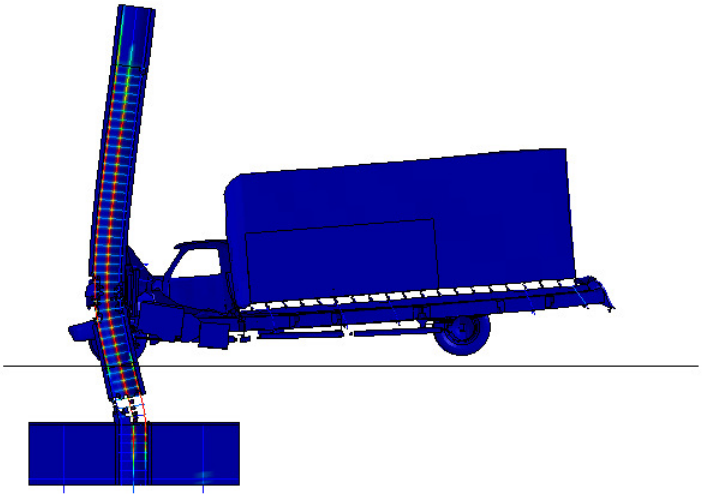

e) 150 ms after impact

Figure G.4. Axial force in long. bars for the 600 mm diameter pier with 150 mm hoop spacing subjected to a 55 km/h impact velocity at different time steps

REFERENCES

AASHTO, *AASHTO LRFD Bridge Design Specifications,* Sixth Edition, American Association of State Highway and Transportation Officials, Washington, D.C., 2012.

Adhikary, S. D., Bing, L., and Fujikake, K. (2012). "Dynamic Behavior of Reinforced Concrete Beams Under Varying Rates of Concentrated Loading." *International Journal of Impact Engineering*, 47, 24-38.

Agrawal, A. K., and Chen, C. (2008). "Bridge Vehicle Impact Assessment." Project #C-07-10, University Transportation Research Consortium, New York Department of Transportation.

Agrawal, A. K., Liu, G., and Alampalli, S. (2013) "Effects of Truck Impacts on Bridge Piers." *Advanced Materials Research*, 639-640, 13-25.

API (2005). "Recommended Practice for Planning, Designing and Constructing Fixed Offshore Platforms – Working Stress Design." American Petroleum Institute, 70-71.

ASCE. (2013). "Report Card for America's Infrastructure." American Society of Civil Engineers. <http://www.infrastructurereportcard.org/a/#p/home> (June 10, 2013).

Bala, S., and Day, J. (2004). "General Guidelines for Crash Analysis in LS-DYNA." Livermore Software Technology Corporation, Livermore, CA. <http://awg.lstc.com/tiki/tiki-download_file.php?fileId=18> (11 November 2013).

Buth, E., Brackin, M. S., Williams, W. F., and Fry, G. T. (2010). "Analysis of Large Truck Collisions with Bridge Piers: Phase 1, Report of Guidelines for Designing Bridge Piers and Abutments for Vehicle Collisions." Texas Transportation Institute, Texas A & M University System, College Station, Texas.

Buth, E., Brackin, M. S., Williams, W. F., and Fry, G. T. (2011). "Collision Loads on Bridge Piers: Phase 2. Report of Guidelines for Designing Bridge Piers and Abutments for Vehicle Collisions." Texas Transportation Institute, Texas A & M University System, College Station, Texas.

Chopra, A. (2012). "Dynamics of Structures: Theory and Application to Earthquake Engineering." 4th ed. Prentice Hall, Boston, MA, 3-33.

Coduto, Donald P. (2001). *Foundation Design: Principles and Practices,* 2nd Ed., Prentice Hall, New Jersey.

Colorado DOT (2007). "Estimate Summary" Pay estimates, Contract ID: C16540. Web. 8 November 2013. < www.coloradodot.info/content/payestimates/16540_02.pdf>

El-Tawil, S. (2004). "Vehicle Collision with Bridge Piers." *Project BC-335-6,* FDOT/FHWA.

El-Tawil, S., Severino, E., and Fonseca, P. (2005). "Vehicle Collision with Bridge Piers." *Journal of Bridge Engineering,* 10(3), 345-353.

Fujikake, K., Li, B., and Soeun, S. (2009). "Impact Response of Reinforced Concrete Beam and Its Analytical Evaluation." *Journal of Structural Engineering*, 135(8), 938–950.

Gallegos, D., and McPhee, M. *Two Truckers Die in Fiery I-70 Crash*. The Denver Post, 15 August 2007. Web. 8 November 2013. < www.denverpost.com/ci_6628365>

Gomez, N. L., and Alipour, A. (2014). "Study of Circular Reinforced Concrete Bridge Piers Subjected to Vehicular Collisions." *Structures Congress 2014*, 577-587.

Harik, I. E., Shaaban, A. M., Gesund, H., Valli, G. Y. S., and Wang, S. T. (1990). "United States Bridge Failures, 1951–1988." *Journal of Performance of Constructed Facilities,* 4(4), 272-277.

Kamaitis, Z. (1997). "Vehicle Accidental Impacts on Bridges." *Statyba*, 3(12), 20-27.

Kudelka, B. (2011). "SCDOT Crews Respond After Fiery Crash Shuts Down I-85." *The Connector*, 2(14).

LSTC (2006). "LS-DYNA Theory Manual." Livermore Software Technology Center, Livermore, CA.

LSTC (2013). "LS-DYNA Keyword User's Manual." Livermore Software Technology Center, Livermore, CA.

Malvar, L. J., and Crawford, J. E. (1998). "Dynamic Increase Factors for Steel Reinforcing Bars." Ft. Belvoir: Defense Technical Information Center.

Mander, J., Priestley, M., and Park, R. (1988). "Theoretical Stress-Strain Model for Confined Concrete." *Journal of Structural Engineering*, 114(8), 1804-1826.

Mohammed, T. (2011). "Reinforced Concrete Structural Members Under Impact Loading." Doctoral dissertation. University of Toledo, Toledo, OH.

Murray, Y. D. (2007). "Users manual for LS-DYNA Concrete Material Model 159." *Report No. FHWA-HRT-05-062*. USA: Federal Highway Administration, US Department of Transportation; 2007.

Murray, Y. D., Abu-Odeh, A., and Bligh, R. (2007). "Evaluation of LS-DYNA Concrete Material Model 159." *Report No. FHWA-HRT-05-063*. USA: Federal Highway Administration, US Department of Transportation; 2007.

NCAC (2012). "National Crash Analysis Center." http://www.ncac.gwu.edu/ (October 1, 2012).

Sha, Y., and Hao, H. (2013). "Laboratory Tests and Numerical Simulations of Barge Impact on Circular Reinforced Concrete Piers." *Journal of Engineering Structures*, 46(0), 593-605.

Sharma, H., Hurlebaus, S., and Gardoni, P. (2012). "Performance-Based Response Evaluation of Reinforced Concrete Columns Subject to Vehicle Impact." *International Journal of Impact Engineering*, 43(5), 52-62.

Smoke, G. (2012). "SC-150 Bridge Replacement After Damage." *2012 South Carolina Highway Engineers Conference*. Columbia Metropolitan Convention Center, Columbia, SC.

Tsang, H., and Lam, N. (2008) "Collapse of Reinforced Concrete Column by Vehicle Impact." *Computer-Aided Civil and Infrastructure Engineering*, 23, 427-436.

U.S. Department of Transportation Federal Highway Administration (FHWA) (2007). "Vertical Clearance." Mitigation Strategies for Design Exceptions, <http://safety.fhwa.dot.gov/geometric/pubs/mitigationstrategies/chapter3/3_verticalclearance.htm> (July 2, 2013)

Vega, C. *Race to Repair Damaged I-30 Overpass*. WFAA, 11 June 2012. WFAA. Web. 23 October 2013. <http://www.wfaa.com/news/local/Truck-hits-overpass-on-I-30-in-Dallas-158372365.html>

Wardhana, K., and Hadipriono, F. C. (2003). "Analysis of Recent Bridge Failures in the United States." *Journal of Performance of Constructed Facilities*, 17(3), 144-150.